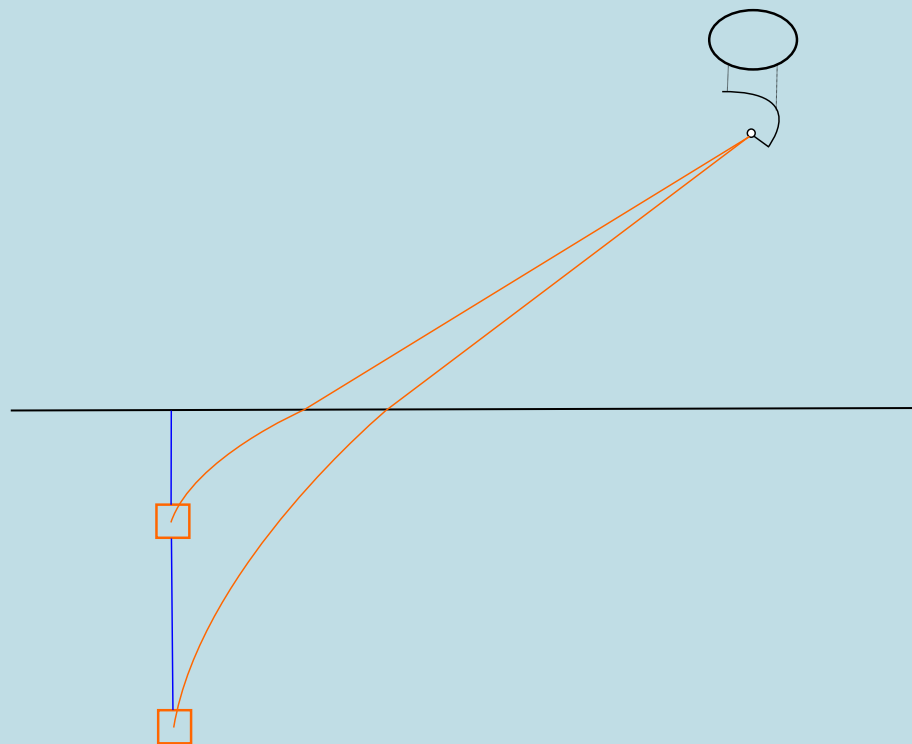


A new ray tracing algorithm for complex ice models and the analysis of ice properties using weather balloons

Arthur Adriaens



Department of Physics and Astronomy

Promotor: Prof. dr. Dirk Ryckbosch Dirk.Ryckbosch@ugent.be

Supervisor: Bob Oeyen Bob.Oeyen@ugent.be

Master's dissertation submitted in partial fulfilment of the requirements for the degree of master in Physics and Astronomy

SUMMARY

Outside our earth various kinds of events take place which we wish to observe: Black hole outbursts, supernovae, cosmic jets, ... These events produce various kinds of messengers which are useful in detecting them: Gravitational waves, gamma rays, protons,... But one particle within this set of particles is quite unique and the subject of our study: The neutrino.

The neutrino is unique in that it points back to the event itself. Due to the neutrino not having any charge, nearly no mass and interacting weakly it doesn't get bend or absorbed and re-emitted on it's way to us unlike say the proton. This means that if we observe a neutrino back here on earth it's very likely that the direction we observe it in, is the direction it came from.

We wish to detect a particular type of neutrinos: The ultra high energy (UHE) neutrino. There have been lots of neutrino detectors around but none of them have been able to observe *cosmogenic neutrinos* which would live past the 3 PeV energy range, this is probably caused by the exponentially falling flux with increasing energy, implying that a really big detector volume is required to detect neutrinos with such high energies.

Due to cost requirements, it was necessary to work in the radio regime. As much as we'd like a really big detector working in the visible spectrum, it would cost way to much. As neutrinos can produce radio waves upon interacting in ice through the Askaryan effect and as radio waves can travel for way longer distances in there before interacting than visible light, it was previously descided in experiments like ARA and ARIANNA to detect on the principle of radio waves. The Radio Neutrino Observatory in Greenland or RNO-G wich is currently under construction and the subject of this thesis builds on the knowledge of these two experiments to make a quite complex detector which should be capable of detecting UHE neutrinos.

The ice properties have an impact on how radiowaves propagate. As mentioned before, RNO-G is a detector built in the Greenland icecap. As the radiowaves get produced in the ice we need to figure out how they propagate towards our detector. An important part in figuring out how they propagate is the local index of refraction which seems to be linearly related to the density of the ice. The density of the ice seems to vary continuously with depth, a function describing this overall relation of the index of refraction with the depth is called an *ice model* and it is

crucial for future studies to understand this ice model.

Due to the ice model seeming to deviate from the theoretically expected single exponential, it was necessary to develop a new algorithm to find the paths the radio waves could take with more complex ice models. The software used within this thesis to figure out the path radiowaves take is called *radioprop*a. Even though this software can be used to work with most kinds of ice models, it still needs to be used within some kind of algorithm to be useful. Such an algorithm has already been developed called the *Iterative ray tracer* as will be explained in section 3.3 but it had its shortcomings, that's why in this thesis a new algorithm was developed called the *hybrid ray tracer* which is explained in chapter 4. This algorithm makes it possible to both find a more accurate and faster solution.

It is, however, crucial to make sure we actually need a new kind of ice model. The measuring of the index of refraction can be accomplished indirectly through weather balloon fly-bys as is explained in chapter 5. Every day in the summer, two times per day a weather balloon is launched from the base camp. This weather balloon is equipped with an antenna which sends out a 403MHz AM signal, upon close fly-bys with detectors this signal can be observed in the detectors. By looking at the difference in arrival time of the signal the difference in timing can be made out from which a plane wave reconstruction can be done. As the accuracy of this plane wave reconstruction is heavily dependent on the local index of refraction in the ice, it can be indirectly measured through this reconstruction. After this analysis the following data was found: (???) These all show a discrepancy with the exponential model as is shown in figure (???).

SAMENVATTING

Er gebeuren verscheidene gebeurtenissen in het heelal dewelke we wensen te detecteren, zoals Black hole outbursts, supernovae, cosmic jets, ... Al deze gebeurtenissen produceren vormen van informatie dewelke we kunnen infereren door hun op een manier te detecteren zoals de protonen en fotonen maar ook verscheidene andere zoals zwaartekracht golven. Maar één bepaald deeltje vinden wij bijzonder interessant: de neutrino.

De neutrino heeft als erg unieke eigenschap dat het terugwijst naar het event waar ze gecreëerd werd. In tegenstelling tot andere deeltjes zoals protonen heeft de neutrino geen lading, bijna geen massa en interageert ze zeer zwakjes. Door deze eigenschappen zal ze op de weg naar de aarde niet afgebogen worden door magneetvelden en hoogstwaardschijnlijk niet interageren met tussenmedia zoals gaswolken, wat impliceert dat als we erin slagen een neutrino te detecteren, de richting waarin ze gedetecteerd wordt hoogstwaarschijnlijk eenzelfde richting is als waar ze vandaan komt.

Neutrinos komen in verschillende energieën maar wij zijn geïnteresseert in één bepaald gebied, boven de 3 PeV oftewel de ultra hoge energie (UHE) neutrino. In de verscheidene experimenten die neutrinos hebben gedetecteerd is er nog geen een geslaagd neutrinos te observeren met energieën boven de 3 PeV, dit is het regime waar zogenaamde *cosmogenic neutrinos* zouden leven en dus uiterst interessant om te bestuderen. Maar, om zo'n hoge neutrino energie waar te nemen blijkt een zeer grote detector nodig te zijn.

Aangezien het zeer rap zeer duur zou zijn om een groot genoeg detector te bouwen om deze neutrinos te detecteren in het visuele spectrum, wat bijvoorbeeld gebruikt wordt in detectoren zoals IceCUBE. Werd besloten om te leunen op het Askaryan effect, dit is het effect die zorgt voor de productie van radiogolven bij interactie van een neutrino in ijs. Aangezien radio golven verder vrij kunnen propageren in ijs dan zichtbaar licht maakt dit het mogelijk om de verscheidene antennes verder van elkaar te plaatsen. Enkele experimenten zijn op dit principe gebouwd zoals ARA en ARIANNA, uit de expertise van deze experimenten werd dan de Radio Neutrino Observatory in Greenland of RNO-G gemaakt. RNO-G moet het mogelijk maken om UHE neutrinos te observeren en deze thesis wenst bij te dragen aan deze detector.

Het blijkt dat de eigenschappen van het ijs een effect hebben op hoe radiogolven zich propageren

door het ijs. Aangezien RNO-G gebouwd is in groenland op een groot volume ijs en ze werkt op het principe van radiogolven is het nodig dit te onderzoeken. Het blijkt dat de propagatie sterk afhankelijk is aan de locale refractieve index van het ijs, dewelke lineair lijkt gerelateerd te zijn aan de dichtheid van het ijs, hoe de lokale refractieve index afhangt van de ruimtelijke positie wordt het *ijsmodel* genoemd. Theoretisch verwacht men een exponentiële afhankelijkheid van de dichtheid met de diepte, maar uit metingen blijkt deze af te wijken van het theoretische model.

De ray tracing simulaties die gebruikt worden om na te gaan waar de neutrino vandaan komt zijn sterk afhankelijk van het ijsmodel. Er werd vroeger een algoritme gemaakt dewelke enkel met het exponentieel model kan omgaan, maar door de recent gevonden tekortkomingen aan dit ijsmodel bleek het nodig een nieuw algoritme te bedenken. Zo'n algoritme, genaamd de *iterative ray tracer* werd daarom uitgevonden (zie sectie 3.3) maar bleek enkele tekortkomingen te hebben. Daarom bleek het nodig om een nieuw soort algoritme uit te vinden dewelke steunt op dat algoritme genaamd de *hybrid ray tracer*, dit algoritme kan gevonden worden in hoofdstuk 4. Dit algoritme maakt het mogelijk om beide een meer accurate oplossing te vinden maar deze ook sneller te vinden.

Maar om over te schakelen op een nieuw ijsmodel met een anders algoritme is het nodig aan te tonen dat er effectief een groot verschil is tussen het theoretische exponentiële model en de echte refractieindex, om dit aan te tonen kunnen we gebruik maken van weerballonnen. Elke dag in de zomer, 2 keer per dag, wordt een weerballoon gelanceerd. Deze weerballoon beschikt over een antenne dewelke een AM signaal uitstuurt aan 403MHz, als zo'n ballon toevallig dicht bij een detector komt zal dit signaal kunnen gedetecteerd worden. Door een plane wave reconstructie te doen van dit signaal en gebruik te maken van de positie van de ballon kunnen we infereren wat de lokale refractieve index is in het ijs. Deze procedure wordt volledig uitgelegd in hoofdstuk 5. Na deze procedure op enkele evenementen toe te passen werd de volgende data gevonden: (???) Hier is een duidelijke tekortkoming van het exponentieel model te zien.

DANKWOORD

CONTENTS

Summary	I
Samenvatting	III
Dankwoord	V
Introduction	1
1 Neutrino as Astroparticle	3
1.1 Discovery	3
1.2 Neutrino sources	4
1.2.1 Cosmological/Primordial neutrinos	4
1.2.2 Solar neutrinos	5
1.2.3 Supernovae	6
1.2.4 Background from old supernovae	7
1.2.5 Atmospheric neutrinos	7
1.2.6 neutrinos from AGNs	8
1.2.7 Cosmogenic neutrinos	8
1.2.8 How do they fit into the full detector spectrum?	8
1.3 Current research	9
2 Radio neutrino detection	10
2.1 Neutrino interactions in ice	10
2.2 Askaryan effect	11
2.3 RNO-G	12
2.3.1 Hardware	13
2.3.2 Reconstruction: Lookup tables	15
2.3.3 Reconstruction: Butterworth filters	15
3 Ray tracing	18
3.1 Wave propagation	18

3.2	Ice model	19
3.3	Iterative ray tracer	22
4	Hybrid Ray tracer	23
4.1	Shortcomings of the exponential ice model	23
4.2	How it works	23
4.3	Performance Optimalisation	26
4.3.1	Length of the normal vector	26
4.3.2	ztol	27
4.3.3	Sphere Size & Step Size	27
4.3.4	Conclusion of optimization	29
4.4	Expansion	31
5	Weather Balloon	32
5.1	Plane Wave Reconstruction	32
5.2	Is the goal feasible?	35
5.2.1	Refraction at the surface	37
5.2.2	Influence of height on Epsilon	42
5.3	Error on prediction	43
5.4	Fitting the index: Channels 0 and 3	45
5.4.1	Spatial data	45
5.4.2	Signal analysis and initial guesses	46
5.5	Channels 6 and 7	50
6	To be deleted	52
6.1	Fitting the index: deep components	53
6.1.1	Station 23 run 800 event 1867 Channels 0 and 3	53
6.2	Special test: Channels 7 and 13	53
A	List of abbreviations	55
B	Balloon passbys under 5° in the summer of 2022	56
C	Balloon passbys under 10° in the summer of 2022	59

INTRODUCTION

Outside our earth various kinds of events take place which we wish to observe: Black hole outbursts, supernovae, cosmic jets, ... These events produce various kinds of messengers which are useful in detecting them: Gravitational waves, gamma rays, protons,... But one particle within this set of particles is quite unique and the subject of our study: The neutrino.

The neutrino is unique in that it points back to the event itself. Due to the neutrino not having any charge, nearly no mass and interacting weakly it doesn't get bend or absorbed and re-emitted on it's way to us unlike say the proton. This means that if we observe a neutrino back here on earth it's very likely that the direction we observe it in, is the direction it came from.

We wish to detect a particular type of neutrinos: The ultra high energy (UHE) neutrino. There have been lots of neutrino detectors around but none of them have been able to observe *cosmogenic neutrinos* which would live past the 3 PeV energy range, this is probably caused by the exponentially falling flux with increasing energy, implying that a really big detector volume is required to detect neutrinos with such high energies.

Due to cost requirements, it was necessary to work in the radio regime. As much as we'd like a really big detector working in the visible spectrum, it would cost way to much. As neutrinos can produce radio waves upon interacting in ice through the Askaryan effect and as radio waves can travel for way longer distances in there before interacting than visible light, it was previously descided in experiments like ARA and ARIANNA to detect on the principle of radio waves. The Radio Neutrino Observatory in Greenland or RNO-G wich is currently under construction and the subject of this thesis builds on the knowledge of these two experiments to make a quite complex detector which should be capable of detecting UHE neutrinos.

The ice properties have an impact on how radiowaves propagate. As mentioned before, RNO-G is a detector built in the Greenland icecap. As the radiowaves get produced in the ice we need to figure out how they propagate towards our detector. An important part in figuring out how they propagate is the local index of refraction which seems to be linearly related to the density of the ice. The density of the ice seems to vary continuously with depth, a function describing this overall relation of the index of refraction with the depth is called an *ice model* and it is

crucial for future studies to understand this ice model.

It has become apparent that the ice model seems to deviate from the theoretically expected single exponential density expectation. In this thesis a new algorithm will be developed which makes it possible to work with more complex ice models and the verification of the shortcomings of the exponential model, which is now the only model that gets used, will be layed out.

CHAPTER

1

NEUTRINO AS ASTROPARTICLE

When looking at phenomena outside our earth the astronomer will turn to electromagnetic radiation, but he's missing out on a big part of the full picture. Not only do interesting events emit photons but also muons, nuclei, gravitational waves,... All kinds of particles which might also be of interest, that's where the astroparticle physicist comes in.

Of all these particles there is one particle which has properties we're quite interested in: the neutrino. Neutrinos don't have any charge, meaning that they are not deflected by magnetic fields. Also neutrinos interact very weakly, because of this they are often called "ghost" particles; on average 100 trillion neutrinos pass through your body per second, none of them having any effect. You'd even need a light year of lead to give you just a 50% chance of stopping a neutrino. These properties makes them ideal messenger particles as, when we detect a neutrino and it's arrival direction, we can be quite sure it came to our detector unhindered from a far away event in the exact same direction. Neutrinos can serve as unique clues about what's happening elsewhere in the universe including the cosmic collisions, galaxies, supernovae, Gamma-ray bursts (GRBs),... where they are created.

1.1 Discovery

When researching β^- decay, the decay of a neutron, researcher detected a proton and an electron coming from the neutron. However on closer inspection it became apparent that energy was lost somewhere in violation with the conservation law of energy, and angular momentum wasn't conserved. The solution postulated by Wolfgang Pauli was to introduce a new, really hard to detect particle with no charge and a very small mass: the neutrino. The neutrino comes in three flavours: electron, muon and tau neutrinos, each corresponding to their respective lepton denoted as

$$\nu_e \quad \nu_\mu \quad \nu_\tau \tag{1.1}$$

and each also having an anti-particle.

$$\bar{\nu}_e \quad \bar{\nu}_\mu \quad \bar{\nu}_\tau \tag{1.2}$$

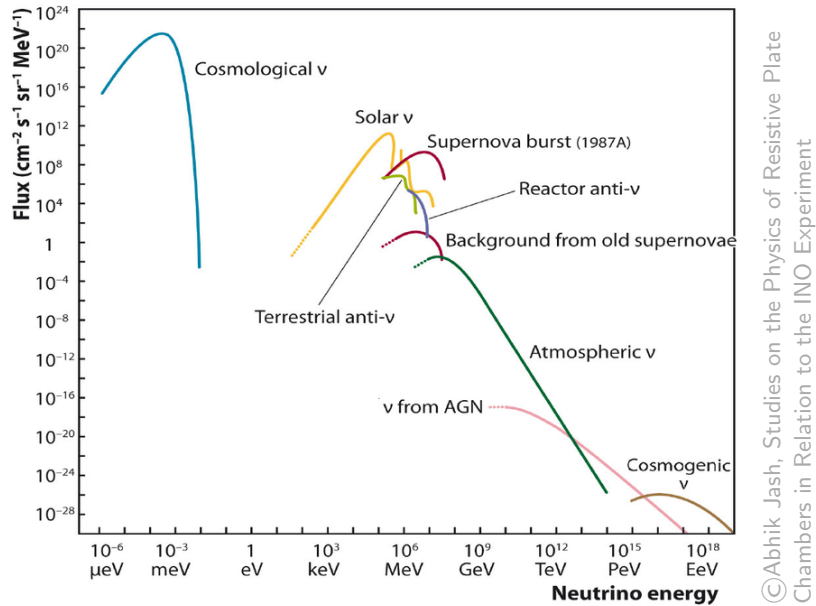


Figure 1.1: Predicted neutrino flux for various sources both natural and man-made

Now with the introduction of the neutrino the full β^- decay becomes

$$n \rightarrow p^+ + e^- + \nu_e \quad (1.3)$$

The inverse can then also be used to detect neutrinos:

$$n \rightarrow p^+ + e^- + \nu_e \quad (1.4)$$

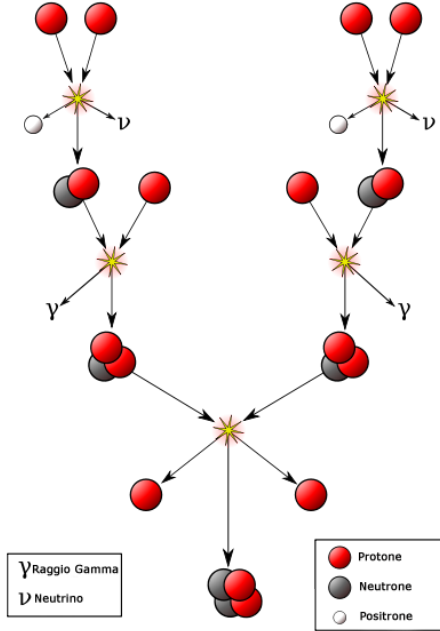
Which is called beta capture and was first experimentally detected in 1956 [10] also making it the first experimental detection of a neutrino.

1.2 Neutrino sources

As shown in figure 1.1 there are various kinds of neutrino sources, we'll discuss these one by one in order leaving out the reactor anti-neutrinos and the terrestrial anti-neutrinos as we're only interested in neutrinos of astrophysical nature.

1.2.1 Cosmological/Primordial neutrinos

The first source of neutrinos we'll talk about is the one in blue to the left of the figure termed the *Cosmological neutrinos*: the neutrino version of the CMB. To understand this source we'll have to go back all the way to just after the big bang: The very early universe was hot and dense. As a result, interactions among particles occurred much more frequently than they do today. As an example, a photon today can travel across the observable universe without deflection or capture, so it has a mean free path greater than 10^{26} m. When the universe was 1 second old, though, the mean free path of a photon was about the size of an atom. Thus in the time it took the universe to expand by a factor of 2, a given photon interacted many, many times. These multiple interactions kept the constituents in the universe in thermal equilibrium. But as the universe expanded there were times when reactions could not proceed rapidly enough to maintain equilibrium conditions, these particles then fall out of thermal equilibrium. This falling out of equilibrium is termed *decoupling*. And we're interested in when neutrinos decoupled. Neutrinos



were kept in equilibrium through the interaction

$$\nu e \leftrightarrow \nu e \quad (1.5)$$

up until the universe cooled down to about 1MeV when they decoupled. To estimate the temperature of the neutrinos who decoupled at the start of the universe, we can take a look at conservation of entropy [11] from which we'll find that:

$$T_\nu = \left(\frac{4}{11} \right)^{1/3} T_\gamma \quad (1.6)$$

Note that they decoupled before the photons making them lower in temperature. As T_γ is the CMB temperature which, nowadays, is measured to be around 2.7K or 2.3×10^{-4} . This would imply $T_\nu = 1.66 \times 10^{-4}$ which is roughly where the peak flux is located. these primordial neutrinos are thus very low in energy.

1.2.2 Solar neutrinos

The sun fuses elements to release energy and thus keeping itself from collapsing in on itself, with most of the various ways particles get fused, neutrinos get released as is shown in figure 1.2.2. Now with this and some information about the sun like the pressure and mass, the so-called "standard solar model" was made. This model predicted a certain amount of neutrinos to be hitting the earth from the previously mentioned thermonuclear fusion, it was however 3 times higher than the observed amount of neutrinos back at our planet. This led to a little bit of hysteria as this could've meant that the sun was dying and we'd see the aftermath only in a couple of years. Through various experiments however, it became apparent that this was due to the different kinds of neutrinos oscillating into each other on their way to earth, i.e 2/3 of the original electron neutrinos had oscillated into mu and tau neutrinos. But for them to oscillate into each other, they not only require mass but each flavor also should have a different mass as can be seen from an example 2D approximation to the transition probability:

$$P(\nu_e \rightarrow \nu_\mu) = |\langle \nu_\mu | \psi(L, T) \rangle|^2 = c_\mu c_\mu^* = \sin^2(2\theta) \sin^2\left(\frac{\Delta\phi_{12}}{2}\right) \quad (1.7)$$

with

$$\Delta\phi_{12} \approx \frac{m_1^2 - m_2^2}{2p} L \quad (1.8)$$

In full generality (3D):

$$|\nu_\alpha\rangle = \sum_i U_{\alpha i} |\nu_i\rangle \quad (1.9)$$

With $U_{\alpha i}$ the Pontecorvo-Maki-Nakagawa-Sakata (PMNS) matrix. This phenomenon has been observed e.g through the discrepancy from the observed and expected neutrino events coming from a nuclear reactor [12].

1.2.3 Supernovae

A star starts its life as a ball of pure hydrogen. At the core, due to the gravitational pressure of the outside plasma, fusion of hydrogen into deuterium and helium happens. Thus converting mass into energy. The pressure of this energy counteracts the pressure of gravity and the star is stable.

When the hydrogen at the core runs out no more hydrogen can be fused. For stars with masses between $8M_\odot$ and $30M_\odot$ the fusion of heavier elements starts, this can't keep going on however as at some point the star starts to form the most stable element: iron. It costs energy to both

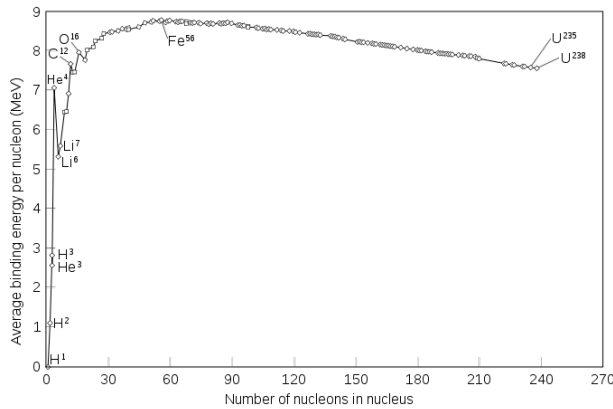


Figure 1.2: Energy per nucleon i.f.o number of nucleons in the nucleus

make lighter elements than iron and heavier ones. As the iron core builds up the outside pressure from the core starts to decrease as no new energy is released. This goes on until the threshold of an iron core with a mass of $1.4M_\odot$ known as the Chandrasekhar limit is reached and the the inwards pressure becomes too large, making the electrons surrounding the iron core fuse with the protons (uud), creating neutrons (udd) and neutrinos, diagrammatically shown in figure 1.3. This last part happens in a split second as the collapse goes at 25% the speed of light, creating a very dense neutron star (3000km in diameter iron core to 30km in diameter neutron star) and

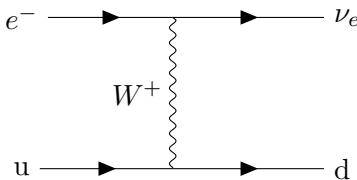


Figure 1.3: fusion of protons with surrounding electrons into neutrons via the weak force

up to 10^{52} ultra-relativistic neutrinos, carrying up to 99%¹ of the released energy [26]. As the density has suddenly increased so much there's a huge distance of pure vaccuum between the plasma outer layer and the (now) neutron star, this plasma starts free-falling inwards, also at 25% the speed of light whilst the neutrinos carrying tremendous amounts of energy start going outwards from the neutron stars core.

The neutrinos then collide with the plasma resulting in what we observe as a "supernova", wrongly thought of by Kepler as being a "new (nova) star" rather being a violent death of an old star.

This is quite unexpected as neutrinos rarely interact, it's only as the incoming plasma is so dense and due to the tremendous amount of neutrinos that collisions happen at all. Some, however, escape and will be visible on earth in our neutrino detectors $\approx 18h$ before the light escapes the exploding star.

Neutrino observatories are thus also useful to know where to point our various telescopes before the supernova is actually visible in the night sky.

1.2.4 Background from old supernovae

Also termed the *diffuse supernova neutrino background* (DSNB), as the universe is quite old various supernovae have happened over it's lifetime, each generating a lot of neutrinos as was discussed in section 1.2.3. This is postulated to have generated a continuous neutrino background.

1.2.5 Atmospheric neutrinos

Before we can talk about atmospheric neutrinos it's necessary to discuss *cosmic rays*. Cosmic rays are ionized nuclei of which 90% are protons, 9% are alpha particles and the rest are heavier nuclei. Almost all of them originate from outside the solar system but from within our galaxy, the few particles that do come from our solar system can be temporally linked to violent events on the sun. In contrast to this the particles coming from outside our solar system show an anti-correlation with the sun as they can more easily reach the earth if solar activity is low. It has been observed that they roughly follow a power-law spectrum $N \propto E^{-\gamma}$ [13].

Cosmic rays hit the Earth's atmosphere at a rate of about 1000 per square meter per second and interact with atomic nuclei in the Earth's atmosphere, creating showers of particles, many of which are unstable and produce neutrinos when they decay, these neutrinos are what's called *Atmospheric neutrinos*. Most notably neutrinos can be produced together with muons in the two-body decays of charged pions and kaons wherever these hadronic interactions occur. The most important production channels and their branching ratios for neutrinos are:

$$\pi^\pm \rightarrow \mu^\pm + \nu_\mu(\bar{\nu}_\mu)(\sim 100\%) \quad (1.10)$$

$$K^\pm \rightarrow \mu^\pm + \nu_\mu(\bar{\nu}_\mu)(\sim 63.5\%) \quad (1.11)$$

Neutrinos are subsequently also produced when these muons decay:

$$\mu^\pm \rightarrow e^\pm + \nu_e(\bar{\nu}_e) + \bar{\nu}_\mu(\nu_\mu) \quad (1.12)$$

which is a process mainly happening at low energies in the atmosphere. The atmospheric neutrino spectrum shown in figure 1.1 roughly follows a power spectrum as the cosmic ray flux follows a power spectrum but the correspondence isn't one-to-one as, due to the difference in

¹ $\approx 1\%$ is released as kinetic energy, only 0.001% as electromagnetic radiation

kinematics, the contribution from kaons to neutrinos is significantly more important than to muons, especially at high energies.

1.2.6 neutrinos from AGNs

An AGN (active galactic nucleus) is deemed to be the reason why several abnormal galaxies exist with an extra bright (and mostly variable) light source in their core which even the biggest of telescopes can't spatially discern. The general consensus is that this phenomenon is caused by one particular kind of object: a supermassive black hole (a black hole with a mass of at least $105M_{\odot}$) surrounded with a close torus of dust and gas. This torus of gas is called an *accretion disc* and is an enormous source of energy. The conversion of potential energy of the incoming gas to highly energetic radiation is a very complex physical process with which we have to account for various factors like gravitational instabilities, magnetic fields, hydrodynamical turbulence,... And thus produces a spectrum that's quite complex. It would appear that the luminosity of an AGN would increase indefinitely with incoming mass, but this process is limited: if too much matter accretes on the black hole the radiative pressure becomes too massive and the matter on the disc gets blown away, this phenomenon is termed a *black hole outburst*.

The emission of high energy neutrinos from AGNs rests solely on the premise that relativistic protons of sufficiently high energy and energy density in the AGN's accretion disc will be present [24] as they may interact to create e.g pions whom decay. A direct consequence of the occurrence of these relativistic protons is the production of γ -rays of similar energies to those of the neutrinos, thus high energy neutrino- and γ -ray astronomy are closely related. However, even though γ -ray photons can be produced even in the absence of relativistic protons (e.g via high energy electrons), neutrinos can not. Thus the detection of these high-energy neutrinos (which might have already been detected [8]) will provide unique information about the workings of AGNs. As these ultra high energy neutrinos get produced near the source (the AGN) they are what's called *astrophysical neutrinos*

1.2.7 Cosmogenic neutrinos

In contrast to the previous source of UHE neutrinos which was generated at the source, called *astrophysical neutrinos* we'll now talk about UHE neutrinos whom are generated through the interaction of ultra-high energy cosmic rays during propagation with the cosmic microwave or other photon backgrounds termed *cosmogenic neutrinos*. The mechanism by which these get created is quite simple, if a proton has sufficiently high energy the cross section to interact with CMB (Cosmic Microwave Background) photons becomes non-negligible. These protons can scatter off the photons to resonantly produce a Δ^+ baryon. This resonance has enough mass to dominantly decay to a pion and a nucleon:

$$\Delta^+ \rightarrow \pi^0 + p \quad (2/3) \tag{1.13}$$

$$\Delta^+ \rightarrow \pi^+ + n \quad (1/3) \tag{1.14}$$

Of which the charged pion decays to neutrinos as previously mentioned in 1.2.5.

1.2.8 How do they fit into the full detector spectrum?

The origin of the most energetic cosmic rays is still not conclusively identified. One approach to solving this problem is *multi-messenger astrophysics*, where several types of cosmic particles are used to identify the sources of these ultra-high energy cosmic rays (UHECRs). E.g we simultaneously measure gravitational waves with the Einstein telescope, neutrinos with RNO-G, photons with various telescopes and muons with a muon detector.

1.3 Current research

Talk about first IceCUBE something?

RADIO NEUTRINO DETECTION

2.1 Neutrino interactions in ice

As neutrinos propagate through ice they can interact weakly. The main mechanisms of interaction is by charged (W boson) and neutral current (Z boson) exchange with nuclei [14] as is also depicted in figure 2.1.



Figure 2.1: Most prominent ways of neutrino-nucleus interaction

With the produced leptons in the W boson mediated interaction being either electrons, resulting in an electromagnetic shower, muons which typically go undetected as they live too long or tauons which will decay via

$$\tau^- \rightarrow e^- + \bar{\nu}_e + \nu_\tau \quad (2.1)$$

or, less ideally

$$\tau^- \rightarrow \mu^- + \bar{\nu}_\mu + \nu_\tau \quad (2.2)$$

In both of the possible interactions (W or Z exchange) the resulting nucleus will result in an hadronic shower, for the neutral current interaction (mediated by the Z boson) the fraction of the neutrino energy that gets transferred to the nucleon is described by the inelasticity y and is heavily shifted towards small values of y [1]. This causes a big, irreducible uncertainty when trying to estimate the original neutrino energy from these kinds of events. With the

charged current interaction (mediated by the W^\pm bosons) this isn't a problem however as the full neutrino energy ends up in the resulting cascades.

2.2 Askaryan effect

For a particle shower to emit strong radio signals, two conditions have to be met:

- There needs to be a separation of positive and negative charges in the shower front
- The signals produced over the length of the shower profile need to overlap coherently.

The *Askaryan* [6] effect, which is responsible for the production of Askaryan radiation describes the effect at radio frequencies which abides by both of these conditions. In general it's a quite difficult effect but we'll give a crude overview. The previously described interactions create a shower of secondary charged particles containing a charge anisotropy. This charge imbalance is a result of medium electrons either Compton scattering into the advancing shower or annihilating with shower positrons. In the end you have a moving charge anisotropy, propagating faster than the speed of light in the medium, creating Cherenkov radiation.

Cherenkov radiation is like the electromagnetic equivalent of a sonic boom, a sonic boom happens when something goes faster than the speed of sound in the medium; A particle emits Cherenkov radiation if it goes faster than the speed of light in the medium¹. Choosing the particle trajectory to lie along the z axis an approximate equation can be found [23] for $\frac{d^2\mathcal{J}}{d\omega d\Omega}$: the energy radiated per elementary unit solid angle and per elementary unit frequency interval

$$\frac{d^2\mathcal{J}(\omega)}{d\omega d\Omega} = \frac{q^2}{4\pi} \sqrt{\frac{\mu}{\epsilon}} \beta^2 \omega^2 \delta^2 [\omega(1 - \beta \mathbf{e}_r \cdot \mathbf{e}_z)] |\mathbf{e}_r \times \mathbf{e}_z|^2 \quad (2.3)$$

Now we can re-write this equation in spherical coordinates, which gives $1 - \beta \mathbf{e}_r \cdot \mathbf{e}_z = 1 - \beta \cos(\theta_c)$ in the delta function. We thus only expect radiation if

$$\cos(\theta_c) = \frac{1}{\beta} = \frac{c'}{u} = \frac{c}{n} \cdot \frac{1}{u} \quad (2.4)$$

With u the local speed of light in the medium and n the index of refraction. I.e if $u > \frac{c}{n}$, Cherenkov radiation will be emitted along a cone surface with half angle $\frac{\pi}{2} - \theta_c$ as illustrated in figure 2.3. Integrating equation 2.3 over the solid angle and formally dividing by the time interval we get:

$$\frac{d^2\mathcal{J}}{d\omega dt} = \frac{q^2}{4\pi} \sqrt{\frac{\mu}{\epsilon}} \beta \omega \left(1 - \frac{1}{\beta^2}\right) \quad (2.5)$$

We see that the energy is proportional to ω , so we expect that most radiation will be emitted "in blue" with a cut-off frequency above which the equation $\cos \theta = 1/(n\beta)$ can no longer be satisfied, this "in blue" characteristic is responsible for the blue glow seen in nuclear reactors as seen in figure 2.2. For ice the index of refraction is roughly 1.78 in deep ice, so we expect an ultra-relativistic particle to produce the most radiation at around 56° opening as

$$\cos(\theta_c) \approx \frac{1}{n} \implies \cos^{-1} \left(\frac{1}{1.78} \right) \approx 56^\circ \quad (2.6)$$

Of course this is just an estimate, as the actual index of refraction is depth-dependent which we'll get to in section 3.2. Now this explains how the signals get generated but logically, from

¹The reader who wants a thorough explanation and derivation is advised to check out *Chapter 14: Radiation by Moving Charges* from the book *Classical Electrodynamics* by Jackson.

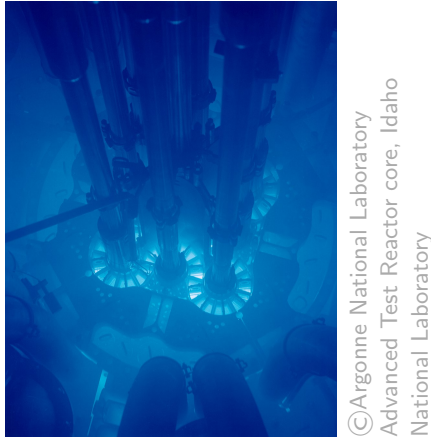


Figure 2.2: Cherenkov radiation in a nuclear reactor

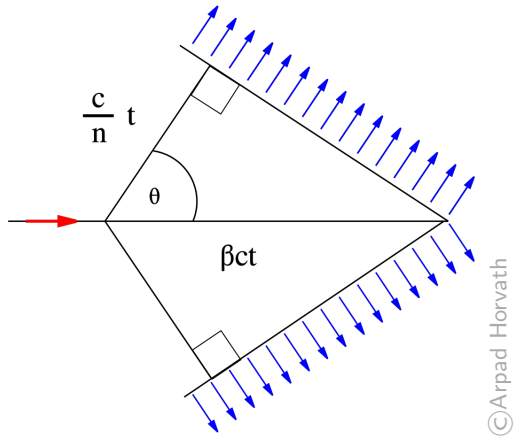
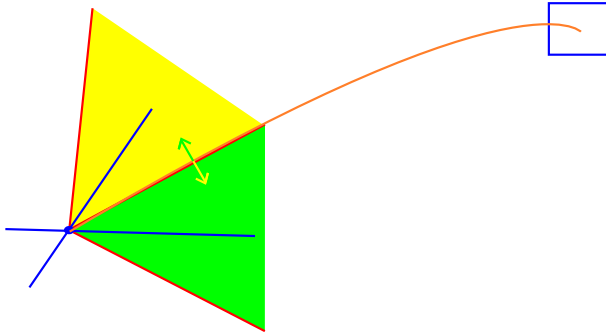


Figure 2.3: Diagrammatic representation of Cherenkov radiation

only knowing this we'd expect radio waves to almost be non-existent due to the "in blue" nature of Cherenkov radiation. This isn't the full story however as we'll need to talk about coherent overlap to fully understand the Askaryan effect. This can be intuitively explained as follows: generally the shower is of length $\mathcal{O}(10\text{cm})$ [22], over this length the radiation gets emitted, most frequencies decoherently interfering, but radio waves with wavelengths of $\approx 10\text{cm}$ coherently interfere, and it's these waves we then wish to detect.

The generated electromagnetic radiation is polarized perpendicular to the cherenkov cone, this can be useful to discern between different cherenkov cones whom, timely, would generate the same response. This concept is illustrated below in 2D where two neutrinos from different directions would generate the same signal in the detector. If the detector has a way to differentiate between polarization however, there would be no doubt where the neutrino originated from as the one producing the yellow cherenkov cone would have a downwards polarization and the one producing a green cherenkov cone would have an upwards polarization, note that in 3D infinite different cherenkov cones could generate the same timely signal (think of rotating the cone around a line on the cone) so both vertical and horizontal polarization information is needed.



2.3 RNO-G

Both cosmic ray and neutrino detectors face the same main problem at the highest energies: the steeply falling flux (as was previously discussed in chapter 2) requires large effective areas, which leads to the construction of neutrino detectors with volumes on the cubic kilometer scale like IceCube [3] which works on the principle of detection neutrinos with visible light. But



Figure 2.4: orthographic projection of Greenland

even IceCube has its limitations, it's still too small to observe neutrino events above the 10 PeV scale [2], that's why a new detector was needed which was even bigger and able to observe Cosmogenic neutrinos. We could just make IceCube bigger but this would cost a lot of money as the individual detectors need to be spaced closely as the attenuation length is quite short for light in the visible spectrum propagating through ice. The proposed solution was to work with radiowave detectors, leveraging the previously discussed Askaryan effect (see section 2.2). Besides the advantage radiowaves have due to their abundance, they can also propagate way further in ice than visible light making it possible to space the individual detectors further apart. The proposed location was Greenland, an island country in North America and part of the Kingdom of Denmark which has large ice sheets. The proposal for RNO-G, which was later funded and now in the construction phase, is for it to be an array of autonomous radio stations each of which having both surface channels and various deep channels resulting in a total of 24 channels per station. The whole project builds heavily on the knowledge obtained through previous radio based neutrino detectors like the NuMoon [9] project, ANITA [28], ARA [5], RICE [25],...

2.3.1 Hardware

One such detector is illustrated in figure 2.5, the plan is to build 35 of these as is shown in figure 2.6². Looking closely at one such detector we see just below the surface 9 Log Periodic Dipole Antennas (LPDAs), these are used to detect air shower muon signals as muons will also generate cherenkov radiation in the ice whose signals can then be filtered out. Aside from these surface detectors there are also deep components of the detector which can be split up in three parts: Two *helper strings* and the *power string*.

The helper strings are the 2 vertical cables shown on the right of figure 2.5 each housing 2 vertically polarized antennas (Vpols), one quadslot antenna for the horizontal polarization component (Hpol) and one radio pulser on each helper string which can be used to generate calibration signals. As was mentioned in the previous chapter the polarization can be used to

²note that all the individual detectors are named after various species living in greenland (in the native tongue)

distinguish between possible cherenkov cones generating the same resulting pulse, that's why both the helper and power string are equiped with both kinds of polarized antennas.

The power string (the leftmost vertical cable) is more densely instrumented than the helper strings: At the bottom it houses a set of four Vpol and two Hpol antennas with a spacing of 1m called the *phased array* and further up the string, with a spacing of 20m, are three more Vpol antennas.

The signal from each of the deep antennae are fed into a low-noise amplifier directly above it, from there the signal is send to the data acquisition (DAQ) system at the surface via a Radio Frequency over Fiber (RFoF) cable. The signals coming from the surface antennae are first passed through a Bandpass filter of 80-750MHz³ prior to both them and the deep component signal ending up in the RAdio DIgitizer and Auxiliary Neutrino Trigger (RADIANT), there it's again amplified, digitized and saved onto an SD card. This data is then transmitted via a Long Term Evolution (LTE) telecommunications network to a local server⁴, from where it is sent via a sattelite link.

As a power source, battery banks are used whom are charged via solar panels. But as there is't enough light during the Greenland winters, there're plans to build wind turbines (with one of the problems being the possibly detectable RF noise the 'engine' would produce).

It can,however, pose a challenge to reconstruct the radio signals produced by the Cherenkov radiation as they are often obscured by background noise. A solution used in RadioReco is Information Field Theory (IFT) implemented in RadioReco by Welling et al. [29] which uses Bayesian inference to calculate the most likely radio signal, given recorded data.

As was previously explained the radio signal from a neutrino often travels along both direct and refracted paths (designated DnR) to the deep array. This double pulse characteristic would be a smoking-gun signature of an in-ice source. The two helper strings are needed for a full direction reconstruction. Three independent measurements are needed for azimuthal information, which is provided by the Vpol (Vertical polarization) antennas and placing the Hpol (Horizontal polarization) antennas at different depths on every string, both zentih and azimuth information will be provided for those signals. The helper strings' calibration pulsers, as well as one on the surface, will ensure regular monitoring of the performance of the station and provide information useful for precise calibration of the antenna geometry.

Christoph Welling did an investigation into energy reconstruction from the received signals [30] for air showers in one single station (as the RNO-G stations are so far apart this is the case here aswell) and he noticed that it is nescessary to know if the detector who observes an event falls inside or outside the Cherenkov cone to accurately reconstruct the primary particle energy as most over-estimated energies in his simulations are caused by events viewed from within the Cherenkov ring being mistaken for events outside of it. He went on to show that, if we somehow know if the shower was seen from inside or outside the ring from some extra source, that most outliers in the energy disappeared. It is shown by Hiller et al. [21] that the combination of a muon detector with the radio detector might make the issue of confusion between being within or outside of the Cherenkov-ring disappear. Because of this the RNO-G stations are fitted with surface Log Periodic Dipole Antennas (LPDA), capable of detecting muons. Note that this is for air showers, the radio signal from neutrinos show additional complexities.

³i.e a filter that only lets frequencies in this range pass

⁴There is additionally a Long Range Wide Area Network (LoRaWAN) antenna as backup in case of problems with the LTE network

2.3.2 Reconstruction: Lookup tables

The main simulation code we'll be using consists of 2 parts: NuRadioMC [15] and NuRadioReco [16]. NuRadioMC uses Monte Carlo simulations to generate neutrino events in the ice and how they propagate to the various channels. NuRadioReco is reconstruction software, it simulates how the various detectors would respond to the detected radiowaves. The plan is to simulate a lot of neutrino events and record the detector responses in a giant database then, when an actual neutrino event occurs, we'll only have to look in the database and match the actual detector response to the simulated detector responses, thus finding the origin.

2.3.3 Reconstruction: Butterworth filters

Sometimes it is necessary to only let through a certain part of the frequency spectrum that's recorded, an elegant way to accomplish this is by using a Butterworth filter. This is a filter that's applied afterwards on the measurements and only let's through a certain part of the observed frequency spectrum

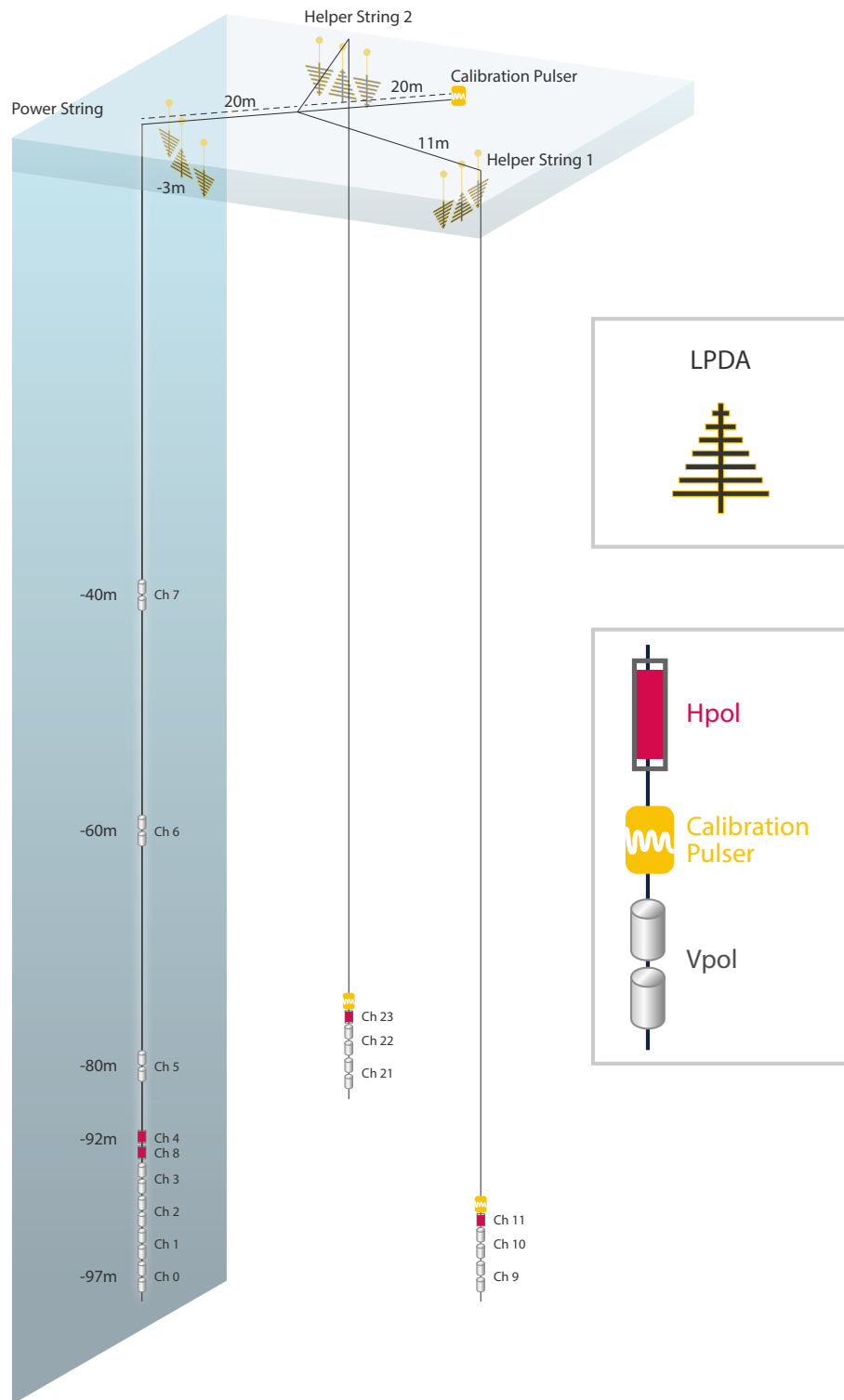
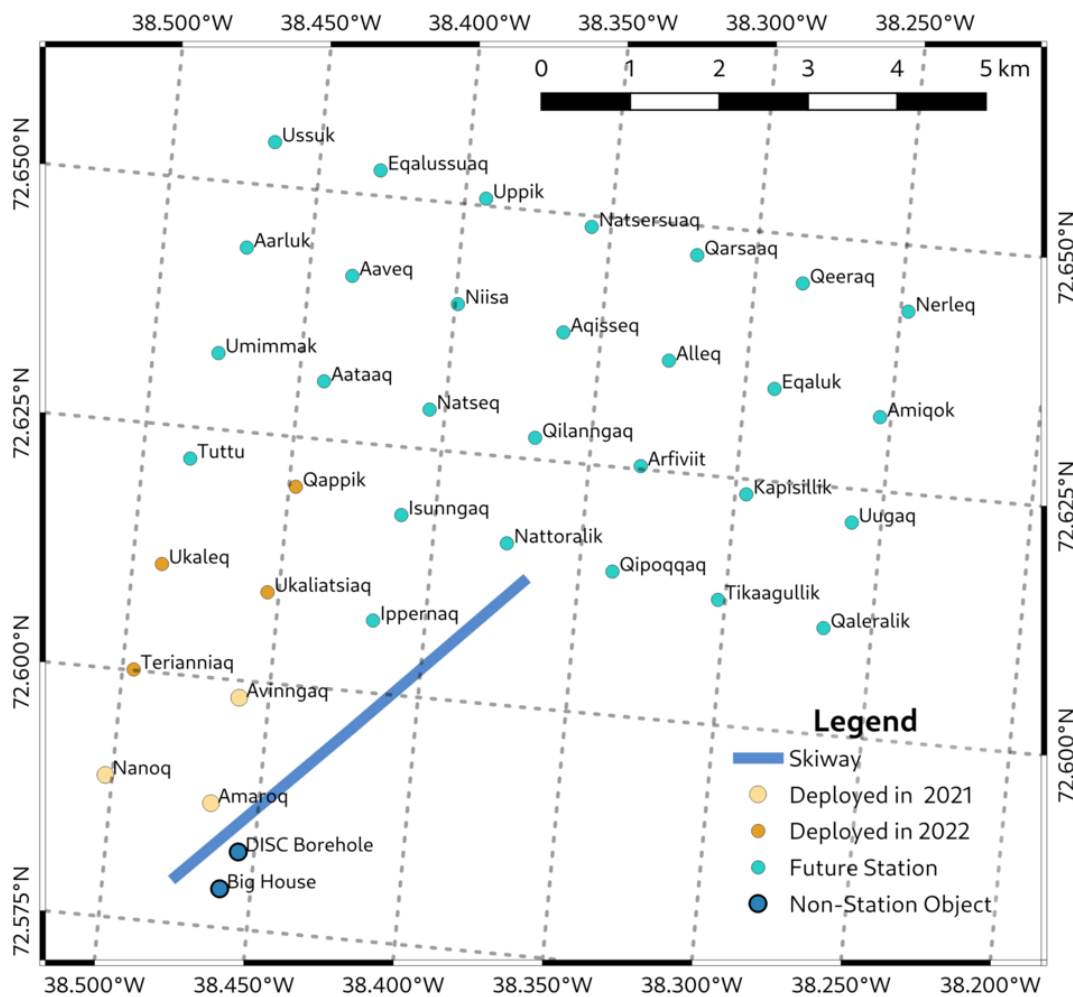


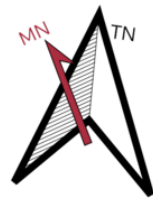
Figure 2.5: illustration of the detector

RNO-G Planned Layout



Notes:

- Station numbering follows a grid, where the first numeral is in increasing W-E and the second numeral is in increasing S-N, skipping non-existent stations (the Seckel method).
- Station spacing is 1.25 km in map coordinates (but really 1.23 km due to projection, which creates a 2% scale difference.)
- Projection is Greenland Polar Stereographic (EPSG:5938). True north indicated by Rose, offset from grid north by 5.37°.
- Magnetic Declination, for August 1 2022, is -25.2° according to the WMM.
- In list below, all future stations labeled as 2023.



v 0.5.1
2022-08-26
68000:1
Greenland Polar Stereographic Projection (EPSG:5938)

Figure 2.6: map of the station

CHAPTER

3

RAY TRACING

3.1 Wave propagation

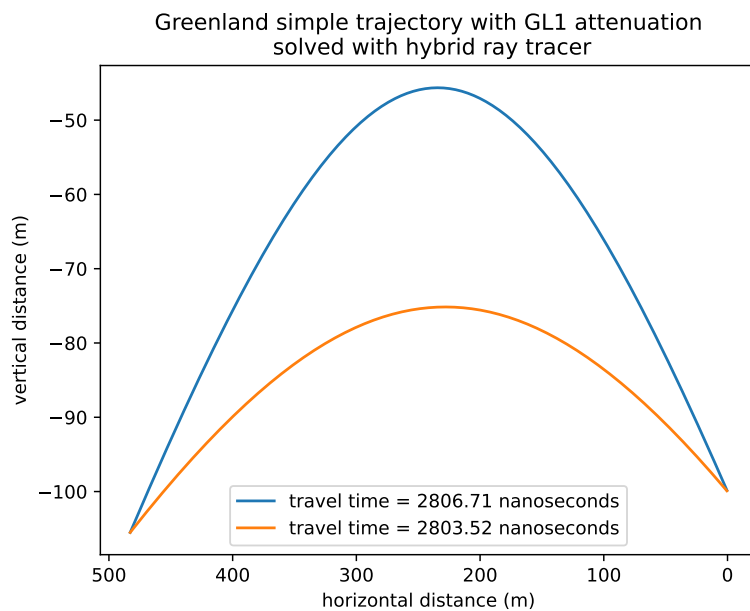


Figure 3.1: illustration of radiowave paths generated by a neutrino event

The way we simulate the strongest waves propagating to the detector from a radio source is through ray tracing, an illustration of such a simulation is shown in figure 3.1. Here the detector is located at (0,-100) and a radio source at (480,-108), note that there are two possible paths leading to the detector.

The amount of solutions and how the waves are bent is due to the nature of the ice we work in. In a dielectric medium a ray propagates with it's signal wave-speed determined by the local index of refraction as $v = c/n$. The effect on speed isn't the only effect the index of refraction has which we'll need to concern ourselves with however, if a ray propagates towards a boundary

dividing 2 media with different indexes of refraction, the ray will refract and the refracted angle can be found from Snell's law:

$$n_i \sin \theta_i = n_o \sin \theta_o \quad (3.1)$$

Where n is the index of refraction, θ the angle with respect to the surface normal and "i" and "o" indicating incoming and outgoing respectively. The system we'll consider however, isn't homogeneous with some specified boundary, it's continuous: ice in greenland has a continuously varying density and index of refraction.

How do we know how the waves propagate in a medium? The software we'll be using to simulate how the radio waves behave is called *Radioprop* [31] and as simulations of the wave propagation in full detail with the finite-differences-time-domain (FDTD) technique [32] are, even though they are more accurate, too time consuming. Have the authors of radioprop chosen to build their program on geometrical optics, i.e ray tracing. A path of a ray $\mathbf{r}(s)$ with path parameter s in a medium with index of refraction $n(\mathbf{r})$ is described by the eikonal equation [18]:

$$\frac{d}{ds} \left(n(\mathbf{r}) \frac{d\mathbf{r}}{ds} \right) = \nabla n \quad (3.2)$$

in radioprop the local paraxial approximation (small angle approximation) is used, i.e if we assume that in any individual step of the algorithm the change of the refractive index along the path ds is small it's possible to re-write the equation as:

$$n(\mathbf{r}) \frac{d^2\mathbf{r}}{ds^2} \approx \nabla n \quad (3.3)$$

Which is then iteratively solved using the Cash–Karp method. The way you would go about using this program is thus find a start and end point (e.g a supposed neutrino interaction point and a detector respectively), "shoot" your ray in a certain direction for which the path will then be iteratively solved using radioprop and if you chose your direction right you have the path a ray might take from your start to the end point. The big complication is this direction choosing which we'll get to later. If there are boundaries (such as defects or the surface) these are treated separately using Snell's law.

3.2 Ice model

Ice has a density gradient which we'll need to account for. Due to the way the ice bonds there will be more air trapped inbetween the molecules closer to the surface than at greater depths where the pressure due to the overhead ice prevents this. Due to this air being trapped the density of ice will be smaller closer to the surface than at greater depth.

Purely from classical gravity and density considerations it can be derived that the density scales exponentially. To see this let's consider a sheet of ice in the Greenland firn with a surface A and a height dz , the extra pressure this sheet of ice exerts on the ice just below it is:

$$d\sigma = \frac{dF}{A} = -\frac{gdM}{A} = -g \frac{A\rho(z)dz}{A} = -g\rho(z)dz \quad (3.4)$$

with $\rho(z)$ the depth-dependent density. Schytt assumed the proportional change in air space to be proportional to the change in pressure:

$$\frac{dV}{V} \propto d\sigma \quad (3.5)$$

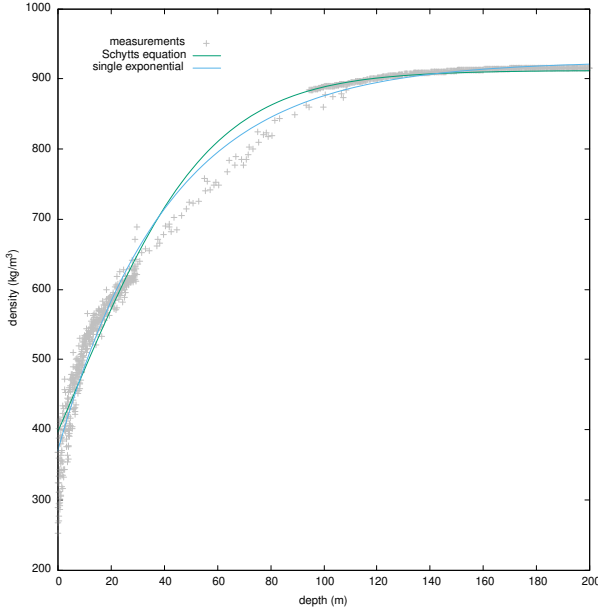


Figure 3.2: Illustration of the shortcomings of the analytical models

As the volume scales inversely with the density let's assume the relation $V \propto (\rho_i - \rho)$ with ρ_i the density of pure ice, this yields [19]:

$$\frac{d\rho}{\rho_i - \rho} \propto \rho dz \quad (3.6)$$

$$\frac{d\rho}{\rho(\rho_i - \rho)} \propto \rho dz \quad (3.7)$$

$$\frac{\ln\left(\frac{\rho}{\rho_i - \rho}\right)}{\rho_i} + C = Az \quad (3.8)$$

$$\ln\left(\frac{\rho}{\rho_i - \rho}\right) = A\rho_i z + C \quad (3.9)$$

$$\frac{\rho}{\rho_i - \rho} = e^{A\rho_i z + C} := Ae^{z/z_0} \quad (3.10)$$

$$\rho = \frac{A\rho_i e^{z/z_0}}{1 + Ae^{z/z_0}} \quad (3.11)$$

Note that Schytt worked with equation 3.7 but we found the further derivation useful. Schytt also empirically fitted the following function:

$$\rho = \rho_0 e^{z/z_0} + B \quad (3.12)$$

Figure 3.2 shows how both of these functions fit the density curve. There is one big downside however, it seems that the ice actually doesn't follow these exponential curves perfectly but would more closely follow some kind of higher order function.

Equation 3.3, and thus the path, depends on the index of refraction on a given location. The dependence of the index of refraction on density for ice can approximately be given by the Schytt equation [7]:

$$n(x, y, z) \approx 1 + 0.78\rho(x, y, z)/\rho_0 \quad (3.13)$$

Where $\rho(x, y, z)$ is the local ice density and ρ_0 is the density for solid ice (917 kg/m^3). For the development of the simulation software equation 3.12 was taken and after assuming Schytt's

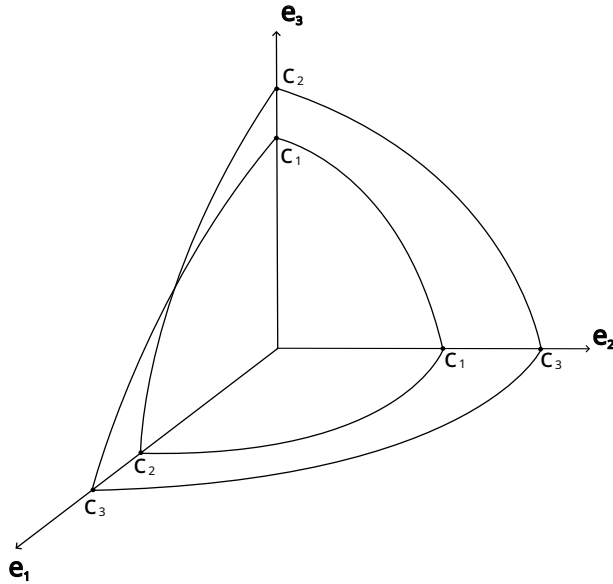


Figure 3.3: Wave surface of Fresnel with two sheets

equation to hold we find that the index of refraction abides by

$$n(z) = n_{ice} - \Delta n e^{z/z_0} \quad (3.14)$$

with n_{ice} the refractive index of solid ice and $\Delta n = n_{ice} - n_s$ with n_s the index of refraction of snow. This exponential dependency of the index of refraction on depth is called "the single exponential model".

This single exponential model has a huge advantage as it's analytically solvable, meaning that we can know which direction we'll have to shoot our ray in (as mentioned previously) after the location of the neutrino interaction and the detector are specified, the ray tracing algorithm developed using this exponential index is called the *analytic ray tracer*.

The discrepancy between the single exponential model and the actual data for the density implies that the analytic ray tracer will make the wrong predictions. This is why the development of a different ray tracer was needed which will be able to handle more complex ice models, one such ray tracer will be explained in section 3.3 but this ray tracer has its shortcomings. That's why the development of a new ray tracer was needed which is the partial work of this thesis and we'll get to that ray tracer in chapter 4.

Lastly there is an effect which might become important in the future: birefringence. Up until now have implicitly assumed that ice is isotropic meaning that both its permittivity ϵ and its permeability μ are scalars but these could very well be tensorial in nature for radio waves in ice. In general, after calculating this tensorial nature through you'd find that in every direction two different indices of refraction can be found implying two different types of waves each propagating with a different speed as illustrated in figure 3.3. Which of the two speeds in a certain direction is then dependent on the polarization of the wave, which in our case thus depends on the Cherenkov cone. The optical property coming from the anisotropic nature of the material is what's called *birefringence*. Birefringence has been extensively researched for implementation in the simulation software NuRadioMC used in the RNO-G group [20].

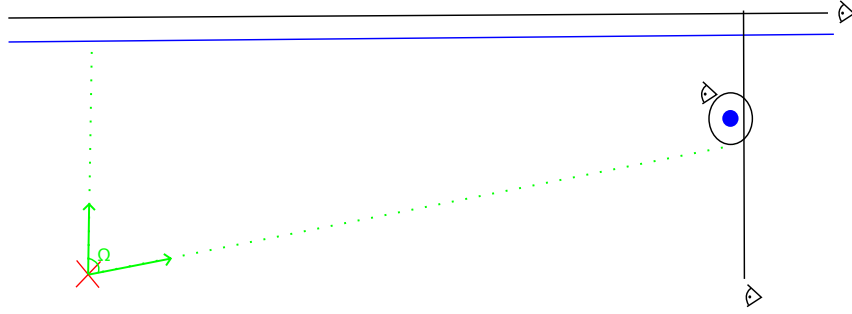


Figure 3.4: Illustration of the workings of the iterative algorithm

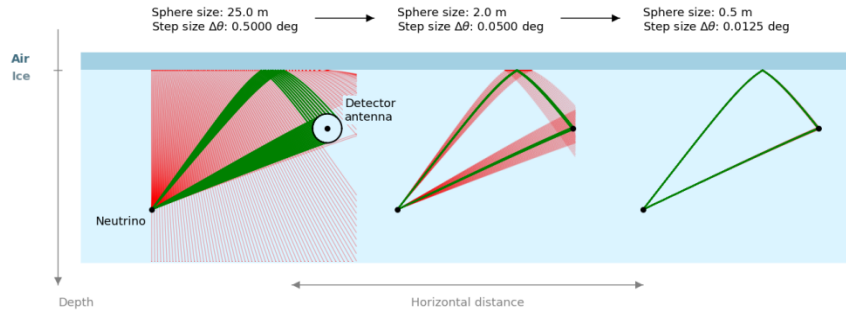


Figure 3.5: Illustration of the steps of the iterative ray tracer

3.3 Iterative ray tracer

The iterative ray tracer [27], as can be derived from its name, iteratively searches the path a ray might take. The workings of the first part of the explanation is illustrated in figure 3.4. Say we have a neutrino interaction point \mathbf{X}_i (the red cross on the figure), and a detector located at \mathbf{X}_d (the blue dot on the figure), the algorithm starts by constructing an *observer* sphere with radius r_1 with the detector, located at \mathbf{X}_d , at the center. This means that any ray that gets shot and propagates to the sphere will get stopped and counts as a solution. Then, to reduce the time spent simulating, there are also observers placed whose purpose is to stop the ray tracing but not count the observed signal as a solution. One such observer is placed just above the ice surface as a ray that escapes the ice won't be able to make it back, and one is placed just behind the detector looking from the point of the interaction vertex \mathbf{X}_i as a ray is not able to reach the detector anymore after it has passed it in the lateral direction. Finally it's noted that due to the way the ice's index of refraction continuously increases with depth, rays can't propagate upwards, this means that we only have to look for solutions within the angle Ω which is just the zenith angle the detector makes with the bottom of the observer sphere. Now that we have our setup we'll just iteratively shoot rays from the neutrino interaction point starting at an angle $\Delta\theta_1$ then at an angle $2\Delta\theta_1$, $3\Delta\theta_1, \dots$. Until we have reached Ω . This process is illustrated on the left side of figure 3.5. After we have gone over all the different launch angles we'll have some solutions (marked in green) and some whom don't end up on the detector (marked in red) we can now make the observer sphere's radius smaller ($r_2 < r_1$) and the step size of the angle smaller ($\Delta\theta_2 < \Delta\theta_1$). And again iteratively find the rays which end up on the sphere, only this time looking within the angles of the solutions of the previous step. We can keep on making the sphere and step size smaller in iterative steps until we've reached the precision we want. We then take, for each bunch of solutions within an angle interval, the most normal to the detector as the final solutions.

CHAPTER

4

HYBRID RAY TRACER

4.1 Shortcomings of the exponential ice model

As mentioned in section 3.2, complex ice models will be necessary moving forward as the exponential ice model fails to fit the density curve. The software for radio wave propagation through ice the RNO-G team chose is radioprop [31], but due to the way it works you'll have to know the start point, the end point and the launch angle of your ray to work out the path. This isn't difficult for the analytic model as it's exactly solvable but for a general ice model you'll somehow have to find where to *shoot* the ray. An algorithm was developed to work out the path the rays would trace out in more complex ice models called the *iterative ray tracer* [27], which was discussed in section 3.3. The way this algorithm works is however a sub-optimal solution in python as an optimisation library will generally work faster and more accurate, work had been done on trying to implement such an algorithm deemed the "minimizer" but this attempt failed. As we saw this work the idea came to mind to combine the iterative ray tracer and the code using the optimization libraries. This way we built the algorithm which will be discussed in this chapter: The hybrid ray tracer, in the source code called the "hybrid minimizer" which can be found [here](#) under the radioprop/hybrid_minimizer branch.

It succeeds in more rapidly finding the path from the event to the detector, is more accurate and also arrives closer to the detector as the final result is not limited by the final drawn sphere size but by a given tolerance making it useful for plane wave reconstruction as we'll get to in the next chapter.

4.2 How it works

The hybrid minimizer can be seen as an extension of the iterative raytracer as it starts out the same way: Say our source of radiation is at position \mathbf{X}_1 and our detector is located at position \mathbf{X}_2 , we start by defining the vector $\mathbf{v} = \mathbf{X}_2 - \mathbf{X}_1$, then we clone it as a new vector \mathbf{u} and set its z coordinate to 0, making it a normal vector of a plane parallel to the z direction in the lateral direction of the detector. We now want to constrain the search to where solutions are actually possible , looking at figure 3.1 we see that no solutions below the direct path are possible as

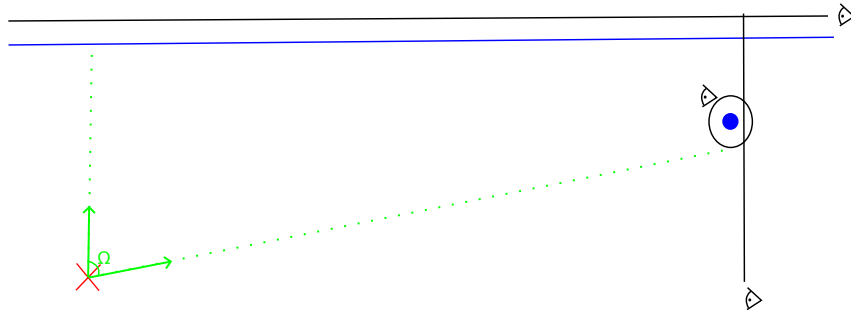


Figure 4.1: Illustration of the workings of the hybrid algorithm

there would need to be upwards reflection, so we convert our vector \mathbf{v} representing the path from the source to the detector to spherical coordinates, giving us a polar angle (zenith angle) "theta-direct". With this we know that from the source the ray should propagate with an initial zenith angle lying within the angle interval 0° to theta-direct $^\circ := \Omega$ ($\theta \in [0, \Omega]$).

Next we need to define our "observers", if you shoot a ray with the radioprop module from a certain point at a certain angle the ray path will get simulated until it interacts with this "observer". Ideally we would like to a priori know where to shoot our ray and have the detector be an infinitesimally small observer in our simulation, but as we'll be working with general ice models this can't be done.

The algorithm of finding the possible paths is then as follows: We define a spherical observer at the location of the detector, with a radius of fair size¹. We place an observer plane directly behind the detector with normal vector \mathbf{u} (as no rays can propagate back after passing the detector) and an observer above the surface (as no rays could make it back after escaping the ice) our full setup is then what's illustrated in figure 4.1

Here the red cross is the radio source, the blue horizontal line is the ice-air boundary surface, the blue dot to the right is the detector and the green Ω indicates the range over which solutions to the problem are possible.

We start off by just iteratively guessing: given a certain angle stepsize $\Delta\theta$ shoot rays at the angles $\{0, \Delta\theta, 2\Delta\theta, \dots, \Omega\}$ And see which ones get detected at the sphere around the detector, this process is illustrated in figure 4.2. if 2 distinct launch regions are found, the so called *minimization* procedure will start. Using scipy's module optimize.minimize the optimal solution will be found. First we get rid of the spherical observer and place the vertical observer **exactly** at the detector, now to be able to use the minimize module we'll need a function to minimize, for this reason we first define the function *delta_z* as, given a certain launch angle, propagating the ray onto the vertical observer and returning the distance from the point where it lands on the plane to the detector, as illustrated on figure 4.3 (i.e it returns the value Δz). The function we'll minimize is then *delta_z_squared* which just squares the value which *delta_z* returns as we want to do away with negative values (so we can minimize to $\Delta z = 0$). We use the previously found angle boundaries as the boundaries for this minimization algorithm, meaning that if the 2 zenith angle intervals $[\theta_1, \theta_2]$ and $[\theta_3, \theta_4]$ were found in the first step of the algorithm it will first minimize Δz^2 within the first angle interval and find it's solution and then within the second angle interval. With this our algorithm is done, it does have a fail-safe as well for if the first step, finding the launch regions, doesn't find the 2 launch regions. Namely it reverts back to being the iterative ray tracer.

¹We'll get back to this

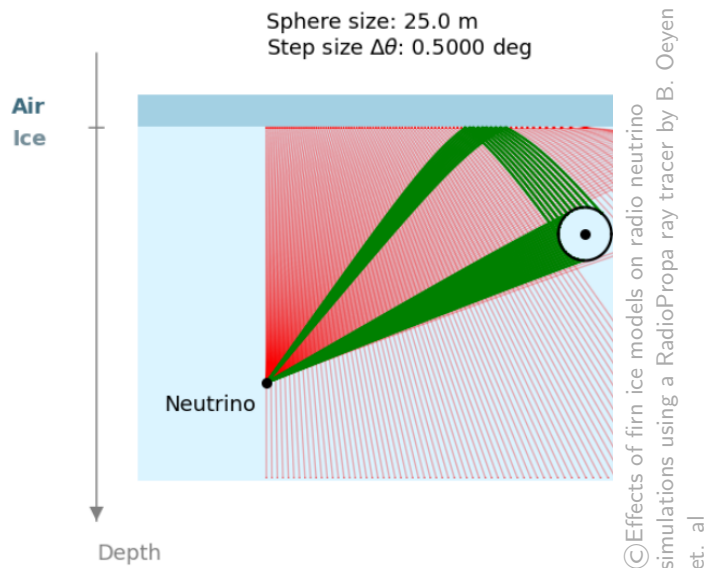


Figure 4.2: First step of the hybrid ray tracer

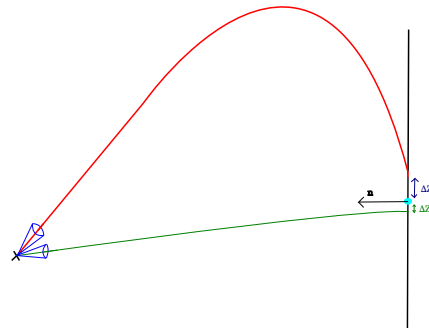


Figure 4.3: Principle behind the minimization in the hybrid ray tracer

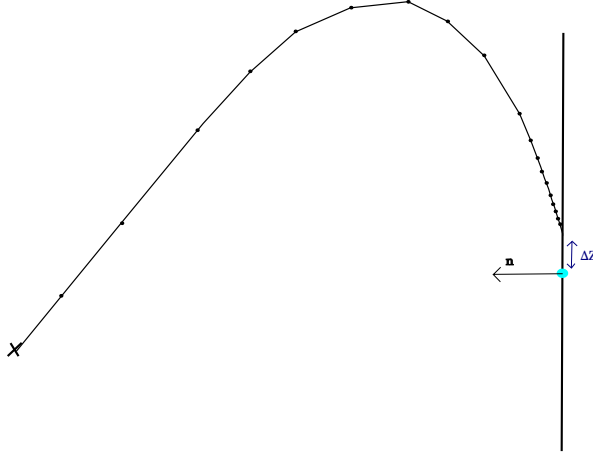


Figure 4.4: how normal vector size influences the stepsize

4.3 Performance Optimisation

We wish to optimize this algorithm to make it as fast as possible. To consistently test the algorithm after every particular change in a parameter we'll be randomly generating vertex interaction positions, keeping the detector at the fixed (0,-100) value. To this end the numpy random module was used to generate random coördinates, the considered square (as there is only a z component to the ice model the 3D problem is cylindrically symmetric and thus essentially only a 2D problem) is x:0.1km,4km and z:-0.1km,-3km². Every simulated point shown in the following subsections consists of at least 500 random initial positions. As the speed of the algorithm is computer dependent the algorithm's speed is always plotted relative to the iterative ray tracer's speed, simulated with the same coordinates equal computer load.

Now we don't want to just achieve higher speed in our algorithm, we also want to at least have the same accuracy as the iterative ray tracer, if not even better. To this end we need to check with an "exact solution". There is only one candidate that fits this role: *the analytic ray tracer*. The plan is thus to use the exponential ice model as a testing ground for the hybrid ray tracer and solving each vertex-detector ray tracing problem with both the iterative, analytic and hybrid ray tracer. After having solved for the **propagation time**, meaning the time it takes the ray to propagate from the source to the detector. And the **arrival zenith angle**, the zenith angle the ray makes at the detector, for each of the algorithms we can infer the accuracy of a particular algorithm by how much it differs from the solution found through the analytic ray tracer. For example, if the hybrid ray tracer finds a particular solution with a propagation time of 1001ns, the iterative finds one with 1002ns and the analytic one with 1000ns then the hybrid ray tracer is more accurate than the iterative ray tracer.

4.3.1 Length of the normal vector

Whilst figuring out what was wrong with the initial *minimizer* we stumbled on the fact that radiopropo has a little weird quirk. As visually explained in figure 4.4, the size of the normal vector seems to influence how big radiopropo's ray tracer's step size is taken close to the detector.

²This start at 100m depth was to get around issues concerning events that won't even trigger in a full simulation

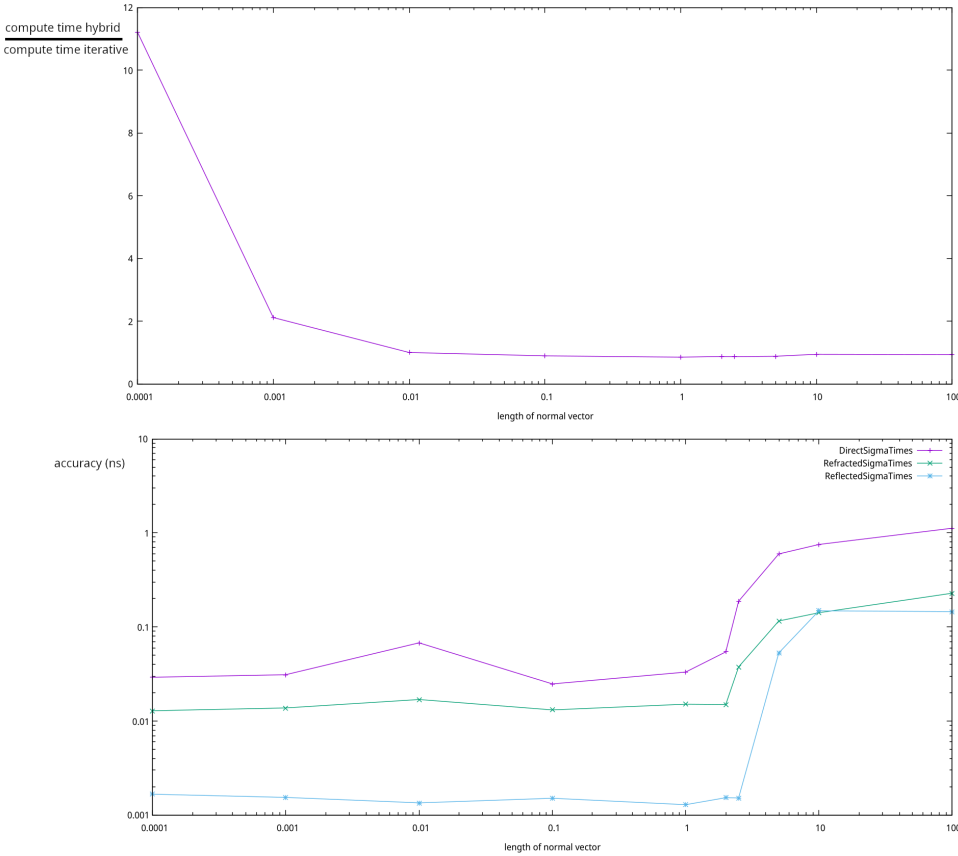


Figure 4.5: influence of the length of the normal vector

This thus influences the accuracy and total computational time taken. The results of varying the length of this normal vector, comparing the accuracy (in timing and arrival zenith) with the analytic ray tracer and the computational time with the iterative ray tracer, are shown in figures 4.5 and 4.6. Looking at these figures we can conclude a, what would normally be rather obvious but is interesting nonetheless, first optimization conclusion: take the normal vector length to be 1 meter. We can conclude this as the calculation speed seems to be minimal there (after zooming in on the graph) and the accuracy dropping rapidly after 1 meter.

4.3.2 ztol

We'll now change the *tolerance* on the vertical distance away from the detector which is deemed accepted i.e in figure 4.4 if Δz is below this threshold, the minimization procedure is stopped and the last found answer is the accepted answer. The results from analogous comparisons as previously discussed are shown in figures 4.7 and 4.8. There seems to be a minimum at 0.05m, looking at the accuracy for this tolerance it seems sufficient to be used. We can thus infer the second optimization conclusion: take ztol to be 0.05 m.

4.3.3 Sphere Size & Step Size

The initial rays are sent out in steps of a certain angle and with a sphere around the detector of a certain size, varying this first step of the algorithm might thus have an effect on both the accuracy and the computational time. As this initial search for launch angle regions is also the slowest step in the hybrid ray tracer it's also the most important step to optimize. The optimization procedure is as follows: change the sphere size and loop over various step sizes,

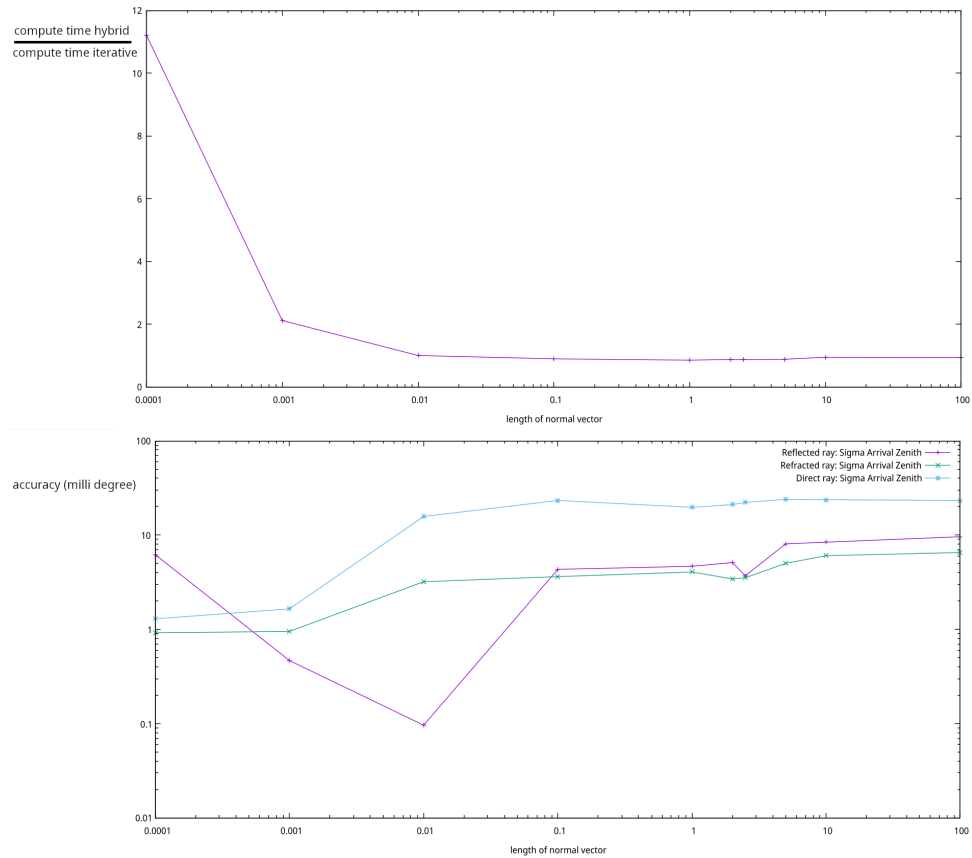


Figure 4.6: influence of the length of the normal vector

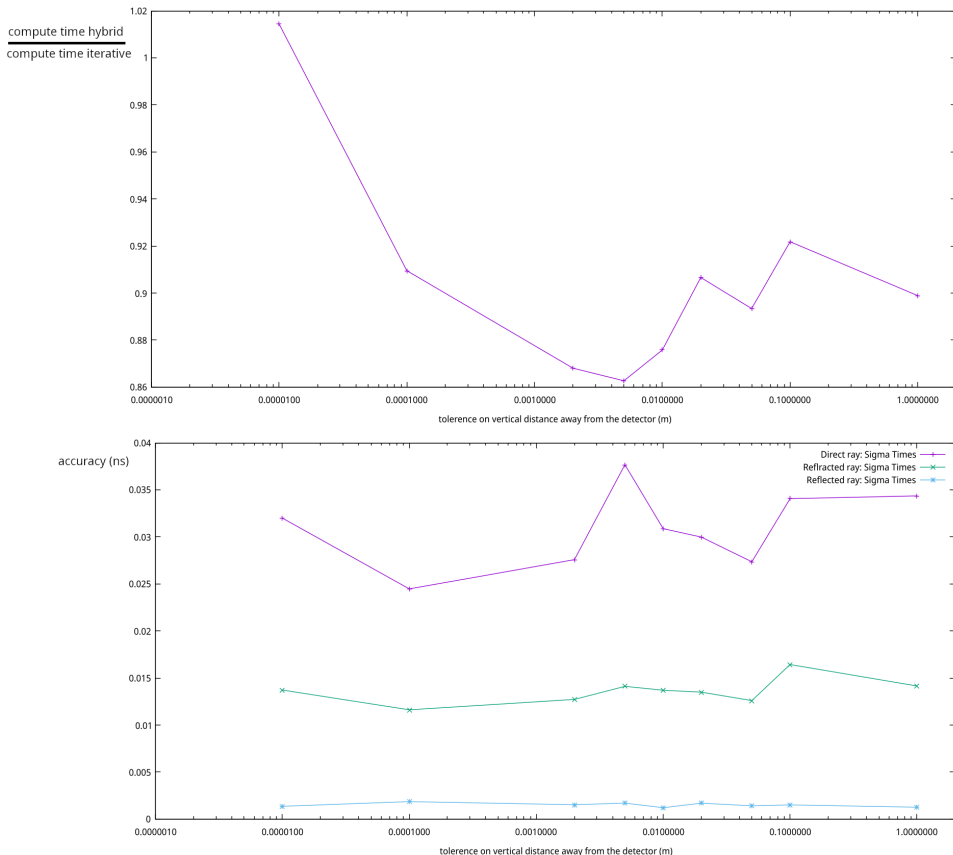


Figure 4.7: influence of the tolerance on vertical distance

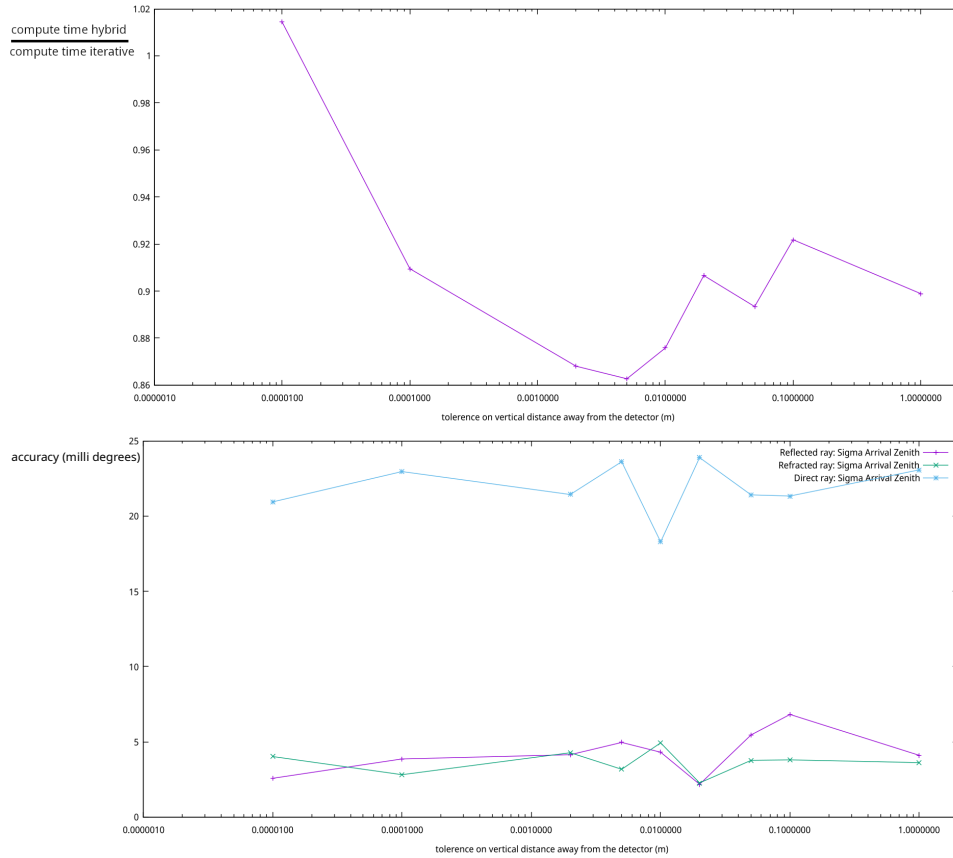


Figure 4.8: influence of the tolerance on vertical distance

recording the speed. Note that, as we have to vary 2 parameters, we can't really look at accuracy here. This isn't needed however as we'll see that after finding the optimal solution the accuracy is still superb, apart from one part where it is needed: **if insufficient solutions are found**, as we wish this algorithm to best the iterative ray tracer, it'll need to at least find as many solutions as the iterative ray tracer does. If, for a particular random interaction vertex location, less solutions are found by the hybrid ray tracer than for the iterative ray tracer, this parameter choice will be thrown away (and colored differently). The results of going through this are shown in figure 4.9, the points colored red are inusable as previously discussed.

The lower on the graph the points lie, the better. If we combine all the green points into a single plot we get what is shown on figure 4.10, zooming in onto the lowest point , we see that an optimal sphere size seems to be at 45m accompanied by a stepsize of 0.7°.

4.3.4 Conclusion of optimization

How does the hybrid ray tracer perform relative to the iterative ray tracer if we use the previously optimized variables? After doing a simulation of 1000 random source locations with the iterative, analytic and hybrid ray tracer and comparing both the iterative to the analytic and the hybrid to the analytic we get what's shown in figures 4.11 and 4.12. Where we can clearly see that the hybrid ray tracer is more accurate, now during this simulation we also recorded the computational speed, the results are presented below:

- iterative: 0.61 computations/s
- hybrid: 0.82 computations/s

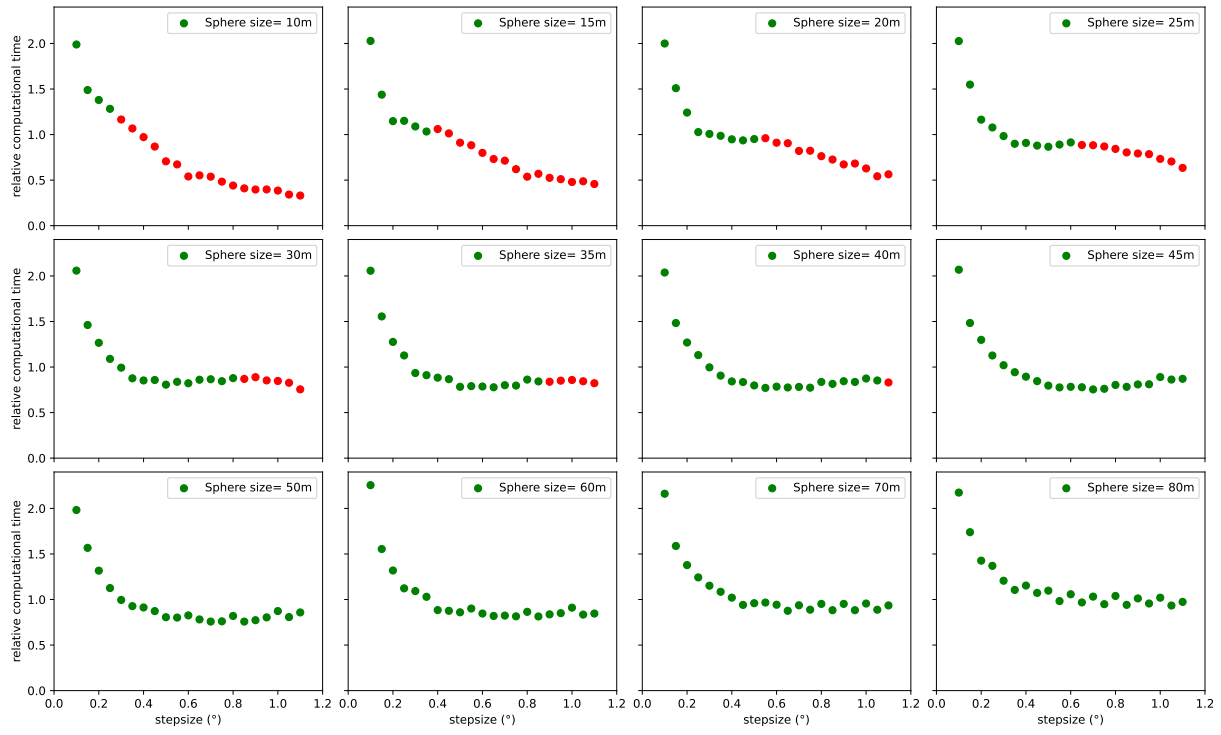


Figure 4.9: Variation in Sphere and angle step size with report on relative time.

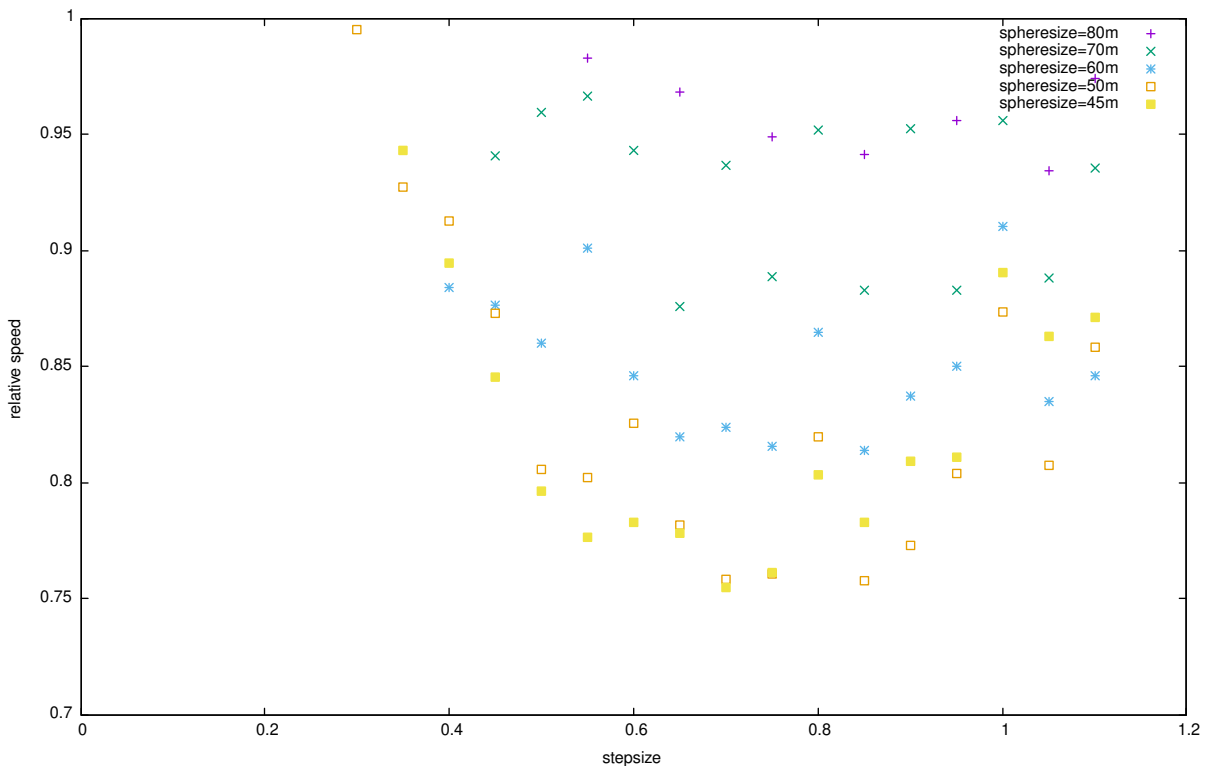


Figure 4.10: Green values in variation in sphere and angle step size with report on relative time.

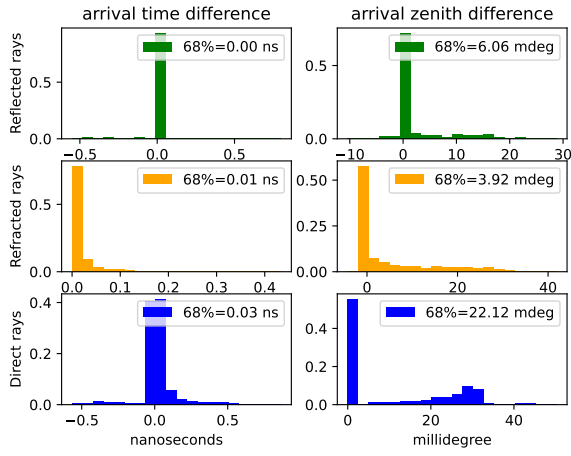


Figure 4.11: Hybrid

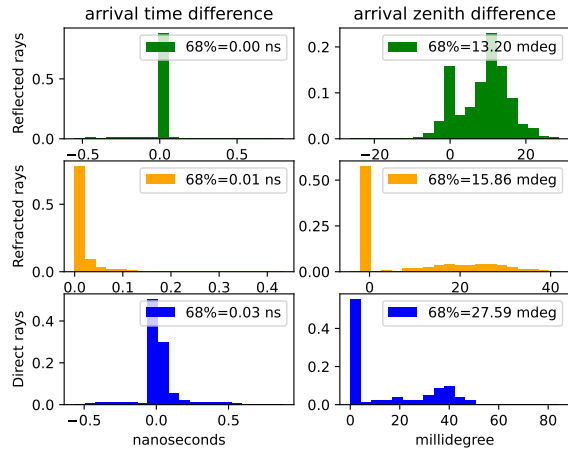


Figure 4.12: Iterative

- analytic (c++ compiled version): 10289 computations/s

The hybrid ray tracer is thus 33.7% faster than the iterative ray tracer, the speed of the analytic ray tracer has a difference to the other two that might seem quite overwhelming but this might get mitigated in the future if part of the hybrid ray tracer gets re-written in a compiled language.

4.4 Expansion

Using the ray tracer as it is now defined makes us unable to calculate paths by *secondaries*. When your ice model has some kind of added complexity like a reflective bottom or a discontinuity layer (like what will be the case for our air-bourne balloon in the next chapter) you'll need to account for secondaries, these are additional rays like an extra refracted or reflected rays that get generated at this discontinuity. How the algorithm is now it will follow one ray from the source to the discontinuity and only consider say the reflected ray, whilst a refracted ray generated at such a discontinuity might actually end up closer to the detector.

To implement secondaries, we'll just check if there are any found at the `delta_z` algorithm and if so loop over them, keeping the original ray's Δz in mind as the "global best" and looking if any of the secondary rays' Δz is lower than the "global best" if so this will be considered the new final ray which gets returned and the Δz that gets returned is the new "global best" originating from the secondary, if there is no secondary ending closer than the "original" ray than the original ray with its Δz is returned.

CHAPTER

5

WEATHER BALLOON

In this chapter we'll simulate radio signals coming from a weather balloon flying over the stations. Our goal is to use the plane waves method to reconstruct the position of the weather balloon with the timing information inferred from the detected radio signals in the detectors. If this is somewhat successful it can be used (as we'll get to shortly) to find out the local index of refraction in the ice.

There are 2 changes that need to happen first to our algorithm for us to be able to simulate this: The air observers needs to be hard removed as to make a ray tracing possible from within the air to the detector and second off, we'll need to implement secondaries. The problem is essentially that a ray coming from the balloon propagates to the ice, refracting and reflecting and then one of the refracted rays hits the detector. The "primary" ray is considered the reflected one so we adjusted the algorithm to look at the secondary that ends closest to the detector and return that ray. What this has as a consequence is that the "path" you get back is only the path from when it "became" a secondary (so only the part below the ice) but this can be easily fixed as the radio wave just propagates straight from the balloon to the beginning of that ray, making the full ray reconstructable by just assuming a line from the balloon to the "start" of the ray.

From this information the propagation time from the balloon to the ice t can later be added to the time of the path in the ice by measuring the length d of the drawn line from the balloon to the beginning of the recorded path, setting the speed of radio waves in air to c and then just adding $t = d/c$.

5.1 Plane Wave Reconstruction

Now having modified our ray tracer, the first problem we'll consider is plane wave reconstruction of the original position, an example path to some of the deep sensors is given in figure 5.1 The plane wave reconstruction can easily be understood using figure 5.2, the waves coming in are drawn in blue and make a certain angle with the detectors. the top detector (top box) detects the wave at a certain time t_1 , the bottom detector detects it at a time t_2 . In our database, after decoding the signal we'd thus see that these two detectors got a signal $\Delta t = t_1 - t_2$ seconds apart

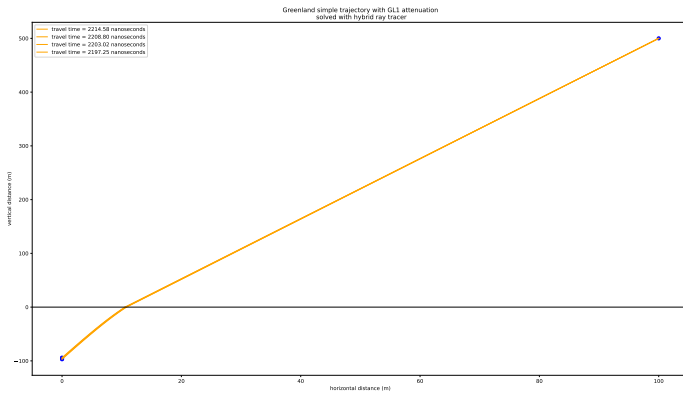


Figure 5.1: Example trajectory of rays coming from a weather balloon (blue dot top right) and going through the ice to the various detectors (blue dots bottom left)

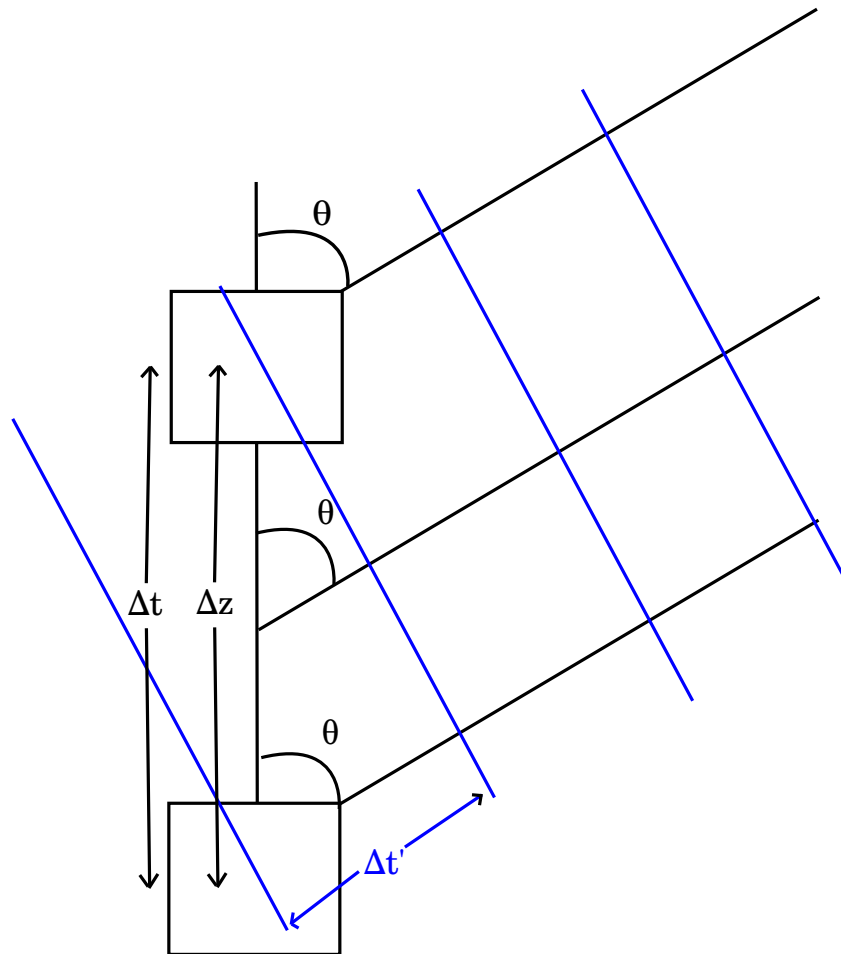


Figure 5.2: Illustration of Plane waves

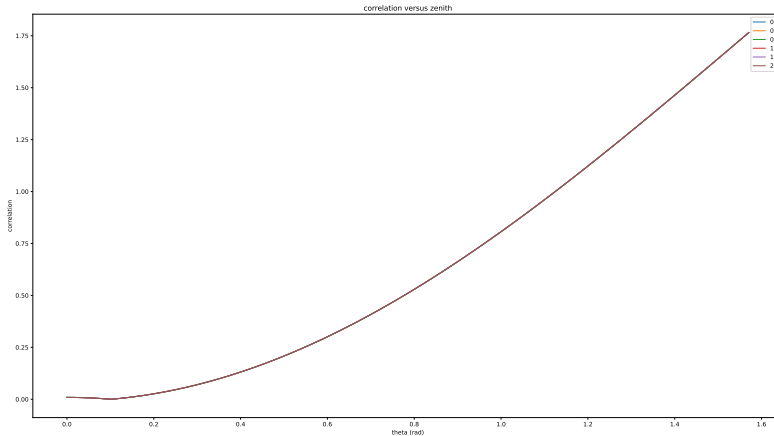


Figure 5.3: Example normed correlation functions

from each other. Now ideally this is equal to the time $\Delta t'$ which is the time it took the wave to propagate that distance which we can calculate from basic trigonometry and dimensional analysis:

$$\Delta t' = \frac{m}{(m/s)} = (s/m) * m = v^{-1} * m = v^{-1} \cos \theta \Delta z \quad (5.1)$$

With $v = c/n$ the local speed of light. As previously discussed this n is depth-dependent and for comparison with the fitted index we'll be using the models local index of refraction. Say we have 4 detectors at depths -94,-95,-96,-97, this then would mean that we'll set the index of refraction at a depth of -95.5, exactly inbetween:

```
1 ice = medium.greenland_simple()
2 n_exact = ice.get_index_of_refraction(np.array[0,0,-95.5])
```

Now in reality we don't know the angle a priori, we'll only have the timing information, so we'll perform a scan by minimizing something we define here as *the correlation function*:

$$\text{Correlation}(\theta) := \Delta t - \Delta t' = \Delta t - \frac{\cos \theta \Delta z}{v} \quad (5.2)$$

If we have more than 1 detector however (which of course will be the case in RNO-G), we'll need to specify various correlation functions. E.g if we have four detectors labeled 0 to 3 we'll have to construct correlation functions between detectors 0&1, 0&2, 0&3, 1&2, 1&3 and 2&3 . As all of these correlation functions will have different sizes we'll norm them as follows:

$$\text{Correlation}_{\text{Normed}}(\theta) = \frac{\text{Correlation}(\theta)}{\int \text{Correlation}(\theta) \Delta \theta} \quad (5.3)$$

An example of these correlation functions is shown in figure 5.3, notice how you can't differentiate between the correlation functions, this is only possible because of the hybrid ray tracer having that high of a precision. After this we can sum them, as shown in figure 5.4, and look where it reaches its minimum. Using this angle we can then reconstruct a ray and guess where the weather balloon is approximately, this is illustrated in figure 5.12.

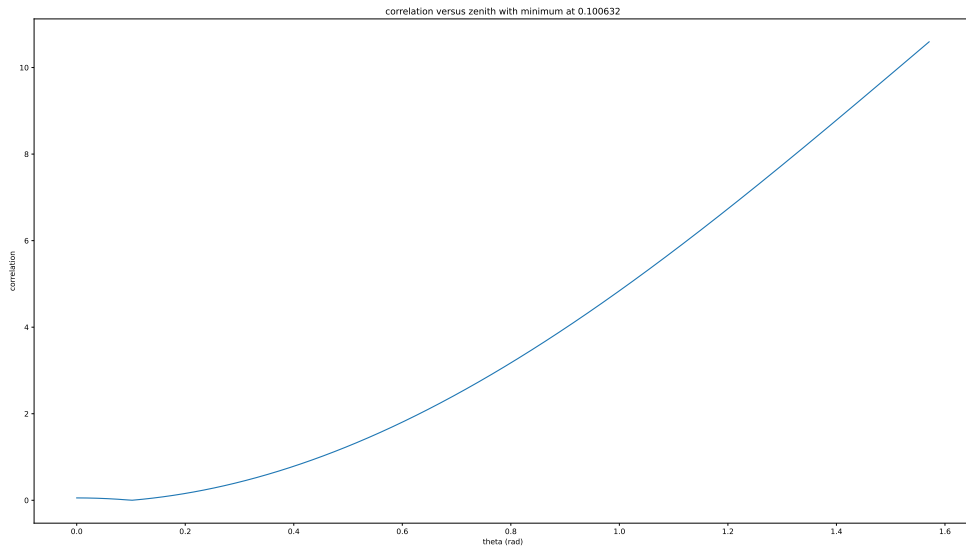


Figure 5.4: Example sum of the normed correlation functions

5.2 Is the goal feasible?

In the example reconstruction illustrated in figure 5.12 the difference in angle between direct to balloon and plane wave reconstruction is already quite small (0.65329617%) but as the balloon gets closer to the detector this reduces significantly as is shown in figure 5.13 where the difference in angle between direct to balloon and plane wave reconstruction is only 0.06788141%. Our goal is to find the local index of refraction n by using the plane wave reconstruction with the recorded timing and the positional data from the weather balloon as the plane wave reconstruction is heavily dependent on the index of refraction (as can be seen in equation 5.2). As was already established we'll consider the index of refraction in the middle of all the detectors (instead of a different one for every pair of detectors), after experimenting this doesn't seem to have an impact on the accuracy of the plane wave reconstruction.

Now let's ask ourselves the question, within which angles should the weather balloon fly for the data to be useful? As was previously stated, the further the weather balloon is away (in the x direction) the bigger the zenith angle with the detector the less accurate the plane wave reconstruction. So which angles are acceptable? Note that not only angle but also height will eventually play a role in the accuracy, the angle however gives a good starting point. To determine this our method works as follows:

we vary the position of the weather balloon in the x direction (keeping the height constant at 500m), simulate the ray path to the channels 0 to 3 and then fit n such that the difference between the reconstructed angle (from the plane wave method) and the direct angle (angle between the middle of channels 0-3 and the balloon) is the smallest possible. Then we compare the n we have fit to the one we know from the model at that position. We quantise the discrepancy between these two indices of refraction using what we here define as the *relative accuracy*:

$$\varepsilon (\%) = \frac{n_{\text{fit}} - n_{\text{exact}}}{n_{\text{exact}}} \times 100 \quad (5.4)$$

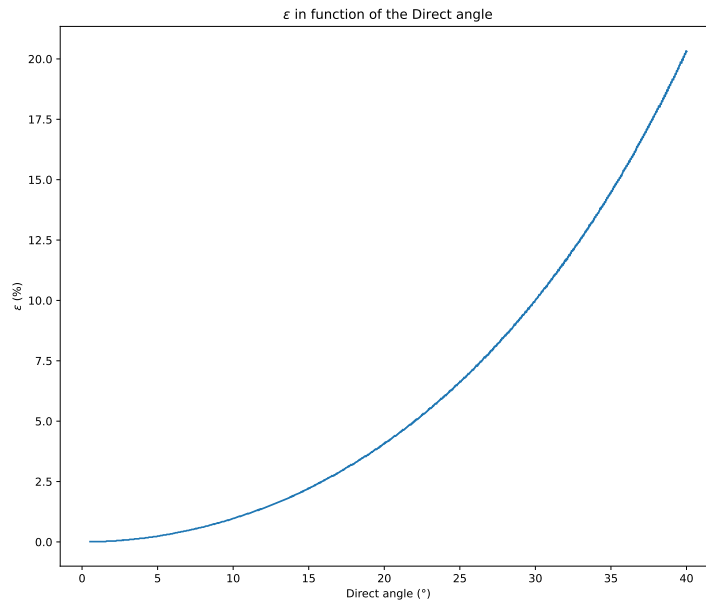


Figure 5.5: Epsilon in function of the direct angle

Carrying this out¹ we get figure 5.5, i.e it gets exponentially shifted towards higher n as the balloon moves further away. If we wish our accuracy to be within 1%, the angle the balloon makes with the middle of channels 0 to 3 needs to be less than 10° . An example path of a weather balloon is shown in figure 5.11, looking specifically at the height information recorded by the weather balloon in a .root file using ROOT² we get what is shown in figure 5.6. It can be seen that the elevation varies between 3228m (read the graph as: Over a 1000 data entries at that height) and 22755m (entries go to zero after that height). This is relative to sea-level, looking at the height map of greenland as shown in figure 5.7 this is obvious. It's quite difficult to work directly with the global geographic coordinate system (longitudinal, latitude and elevation coordinates), that's why we convert them to local ENU coordinates (north, east, up) relative to

¹The code for this can be found in projects-mt/BaLLoN/simulations as plane_wave.py

²<https://root.cern/>

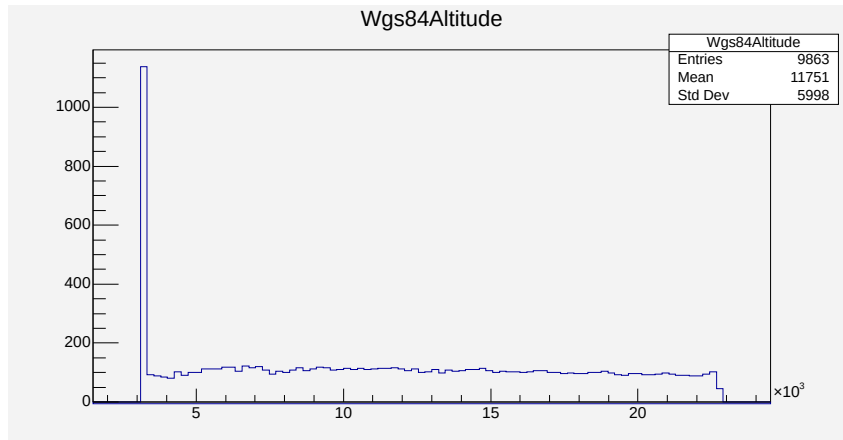


Figure 5.6: Height data viewed in ROOT

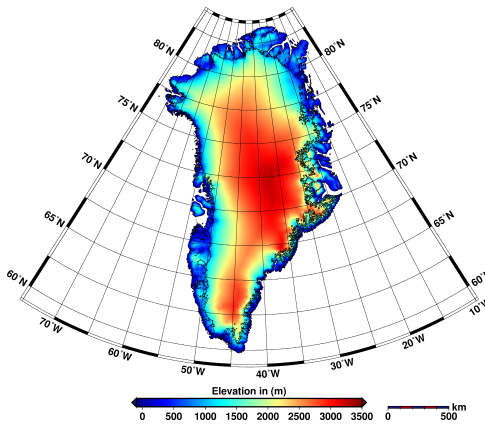


Figure 5.7: Height map of greenland

the 'DISC' which is located at 72.58279265212887 latitude, -38.45581495328228 longitude and 3251.9489147560234 elevation.

Now what would our $<10^\circ$ policy entail? And is it even possible? Say we take a look at station Terianniaq (station 12) it's located at 72.6000868058195° N -38.4962265332872° W. converting this into ENU coordinates we get -137.67250176003688N 1727.5184983294744E, we then set our "up" to be -95.5m as this is the approximate location of the middle of channels 0-3. Now looking at e.g the Balloon path recorded on the 20th of august 2022 (figure 5.10) we see that the balloon crosses paths closely with detector 12, but how close was this encounter? To quantize this we can take a look at every data entry (there are >12000 entries) individually and compute the angle the balloon makes with the detector by first converting the location of the balloon in ENU coordinates, then calculating the horizontal distance ($\sqrt{(x - x')^2 + (y - y')^2}$) then the relative vertical distance $|z - z'|$ and then from those compute the angle ($\tan(\theta) = \frac{Hor.}{Vert.}$) doing this and recording when the balloon gets close enough to get below the 10° mark we get figure 5.9. We thus see that in this example the $< 10^\circ$ policy is viable.

Now how much data do we have that way? We'll be looking at the data recorded over the summer of 2022, more particularly 15/06/2022 - 30/09/2022. The positional data of the weather balloons was obtained from the <ftp://esrl.noaa.gov> website using the rno-g-sonde script of the official RNO-G github page .After looping through every weather balloon gpx file recorded in the summer of 2022 and seeing where it get's within 10 degrees we get the data shown in appendix C, even though this is quite a lot of data there's still another step that we could do to broaden the amount of usable data.

5.2.1 Refraction at the surface

Up until now we have not used the property that waves refract at the surface as we didn't want to assume anything, now say that we include refraction at the surface for our plane wave reconstruction. This would mean that we'd follow analogous steps as our previous analysis, i.e doing a plane wave reconstruction from the difference in timing and trying to fit the index of refraction, only now the plane wave abides with snell's law at the surface, going from $n=1.27$ to $n=1$ and we'll need to minimize the horizontal distance from the ray at the height of the balloon and the balloon, not the angle. The full algorithm thus goes as follows: We first reconstruct the plane wave launch angle θ_1 by minimizing the correlation function previously defined, this gives us a function

$$z = a_{InIce} * x + b_{InIce} \quad (5.5)$$

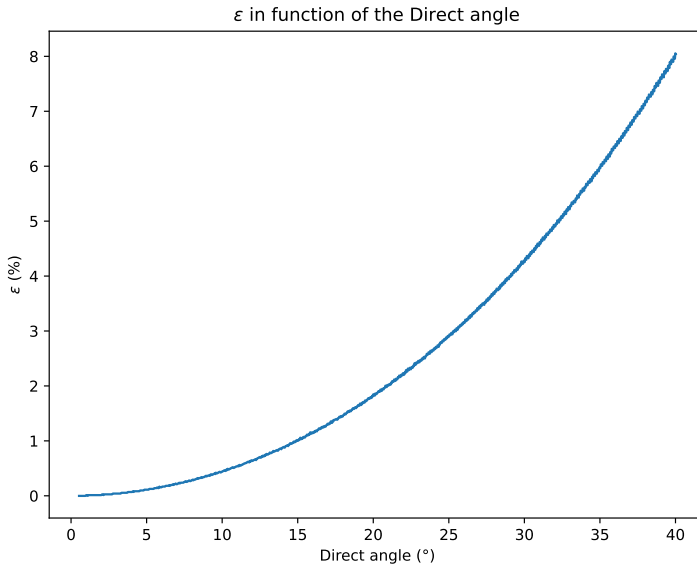


Figure 5.8: epsilon IFO possible angles from channels 0-3 with refraction at the surface

The outgoing zenith angle at the surface θ_2 can be calculated from snell's law:

$$n_1 \sin \theta_1 = n_2 \sin \theta_2 \implies \theta_2 = \sin^{-1} \left(\frac{n_1}{n_2} \sin \theta_1 \right) \quad (5.6)$$

from this we know the slope of the wave path $a_{InAir} = \tan(\frac{\pi}{2} - \theta_2)$ but not the offset, but this can easily be found from equation 5.5 as

$$z = 0 = a_{InIce} * x_{End} + b_{InIce} \implies x_{End} = -\frac{b_{InIce}}{a_{InIce}} \quad (5.7)$$

and

$$z = 0 = a_{InAir} * x_{End} + b_{InAir} \implies b_{InAir} = -a_{InAir} * x_{End} \quad (5.8)$$

$$= a_{InAir} * \frac{b_{InIce}}{a_{InIce}} \quad (5.9)$$

Now that we have the function describing the "path of the plane wave"³ in the air we can find out the horizontal position at the height of the balloon as

$$z = z_{Balloon} = a_{InAir} * x_f + b_{InAir} \implies x_f = \frac{z_{Balloon} - b_{InAir}}{a_{InAir}} \quad (5.10)$$

and iteratively loop over possible indices of refraction, minimizing $|x_{Balloon} - x_f|$.

Doing this whilst looping over possible horizontal balloon positions, we get the result shown in figure 5.8⁴ As you can see we can now go up to 15° and still have less than 1% error! The only drawback of this method is that we need to assume the index of refraction to be 1.27 at the surface of the ice, if this isn't the case in some places our predictions won't be accurate.

³we use double quotes as to emphasize that this is a reconstruction method and not an actual wave

⁴The code for this can be found in projects-mt/BalLooN/simulations as plane_wave_with_snell.py

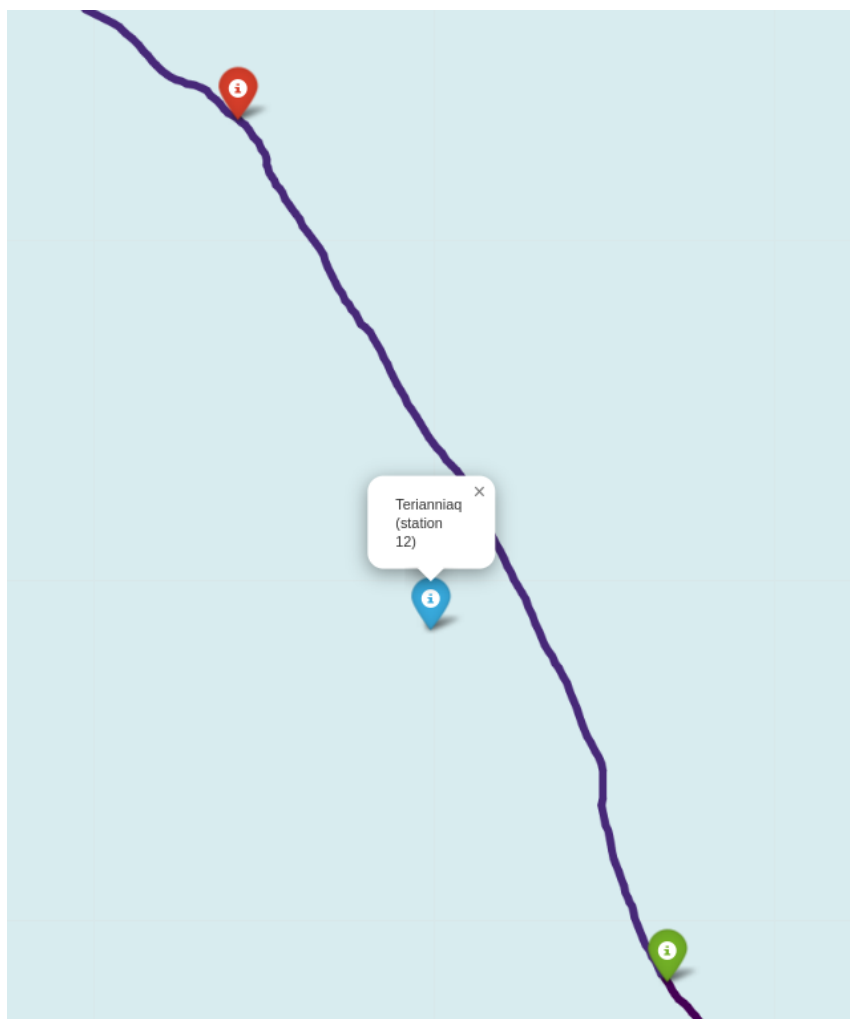


Figure 5.9: Illustration of when the angle with the deep array (channels 0-3) with the weather balloon is less than 10 degrees, the green mark indicates when it starts being less than 10 degrees and the red mark when it stops being less than 10 degrees.

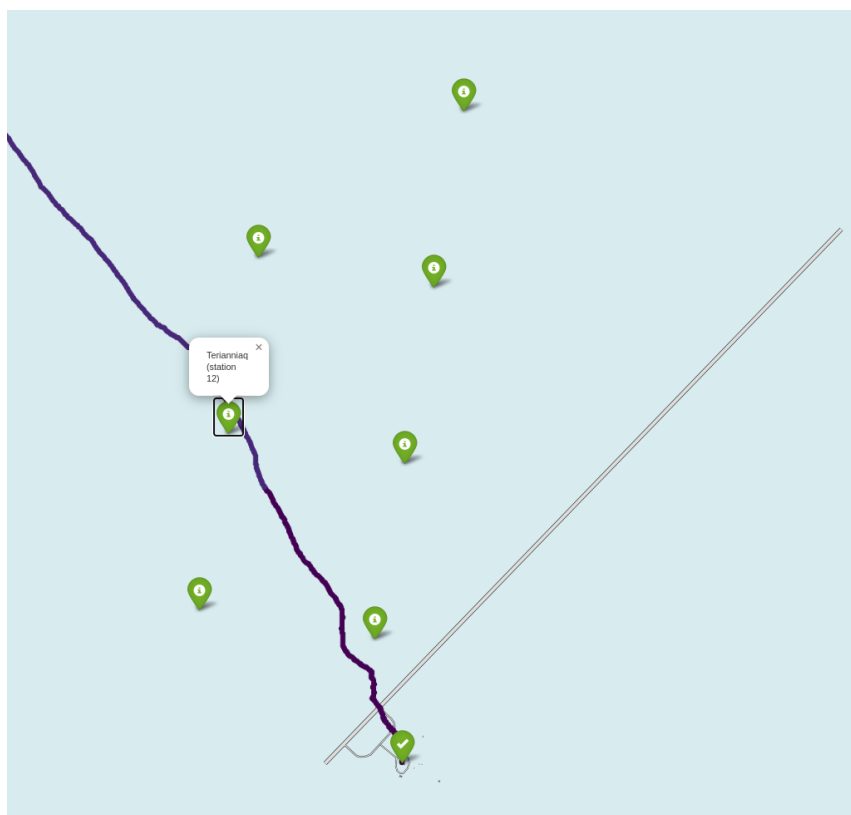


Figure 5.10: Path traced out by a weather balloon released at 20/08/2022



Figure 5.11: Path traced out by a weather balloon released by Bob Oeyen, the checkmark indicating the start and the house mark the end

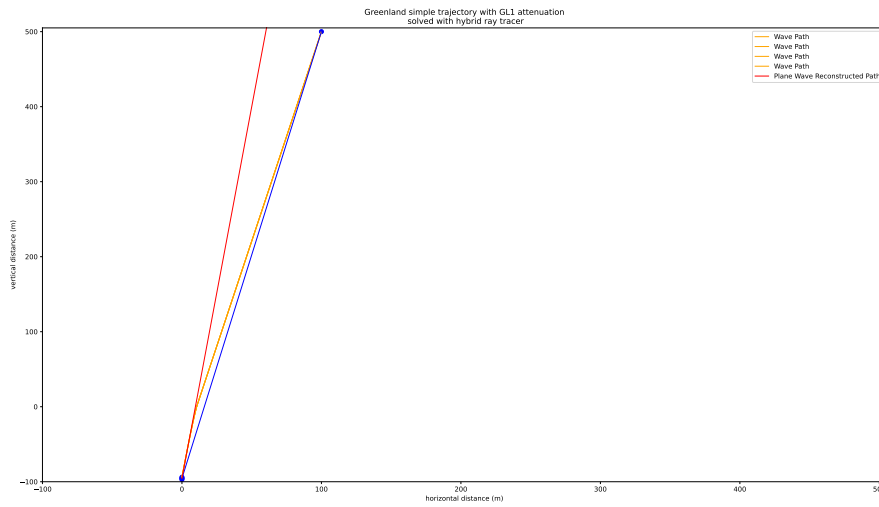


Figure 5.12: Example plane wave reconstruction of weather balloon position

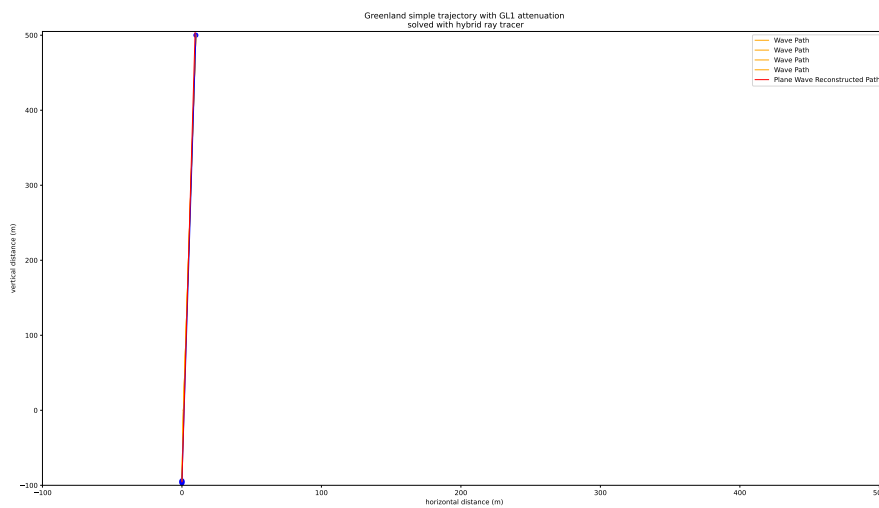


Figure 5.13: Example plane wave reconstruction of near-flying weather balloon position

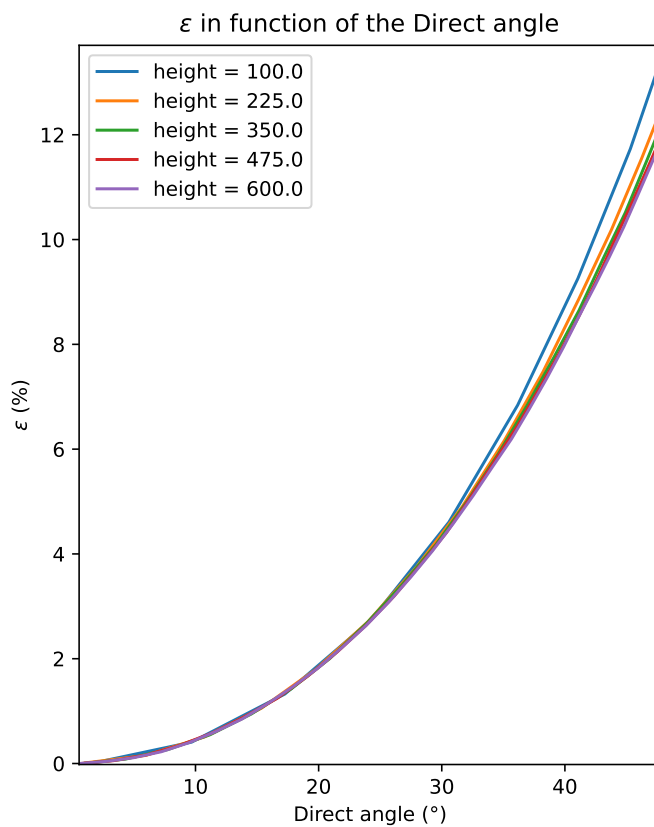


Figure 5.14: How varying the height influences ϵ over the same angles

5.2.2 Influence of height on Epsilon

In the previous sections we've assumed the height to be 500m, does changing this influence the behaviour of ϵ in some way? The answer is, at first surprisingly, yes. As can be seen in figure 5.14. This has, as a consequence, that if we manage to get a hold on some usable data (say the balloon's angle is less than 5°) the ϵ might still be quite large (if the height is really large).

5.3 Error on prediction

Running ahead on the actual measurements, let's estimate how accurate our predictions will be. For the moment we're only interested in the deep channels 0-3. Let's label the vertical spatial accuracy, i.e how accurately we know the height of these channels, δz^5 . And the timely accuracy, or how accurate the vpol timing characteristics are, δt . If we want to fit n, we first minimize the summed correlation function to construct the plane wave. One correlation function is given by

$$\text{Correlation}(\theta) := \Delta t - \Delta t' = \Delta t - \frac{\cos \theta \Delta z}{v} \quad (5.11)$$

Say the minimum occurs at $\text{Correlation}(\theta) = \text{Correlation}(\theta_{min}) := \mathcal{C}$, we can then re-write this equation for n:

$$n = \frac{c(\Delta t - \mathcal{C})}{\cos \theta_{min} \Delta z} = \frac{c}{\cos \theta_{min}} \left[\frac{\Delta t}{\Delta z} - \frac{\mathcal{C}}{\Delta z} \right] \quad (5.12)$$

The Δz is the vertical distance between two channels and thus has an error of $2\delta z$ and Δt is the time difference between two channels, implying an error $2\delta t$. Let's look at the two terms separately (assuming the error on θ_{min} to be negligible), the first quotient $\phi_1 := \Delta t / \Delta z$ has a variance [17] of

$$s_{\phi_1}^2 = \frac{1}{\Delta z^2} s_{\Delta t}^2 - 2 \frac{\Delta t}{\Delta z^3} s_{\Delta t \Delta z} + \frac{\Delta t^2}{\Delta z^4} s_{\Delta z}^2 \quad (5.13)$$

Assuming Δt and Δz to be independent:

$$s_{\phi_1}^2 = \frac{1}{\Delta z^2} s_{\Delta t}^2 + \frac{\Delta t^2}{\Delta z^4} s_{\Delta z}^2 \quad (5.14)$$

$$= 4 \left(\frac{1}{\Delta z^2} \delta t^2 + \frac{\Delta t^2}{\Delta z^4} \delta z^2 \right) \quad (5.15)$$

And the second term ($\phi_2 := -\mathcal{C}/\Delta z$):

$$s_{\phi_2}^2 = \frac{\mathcal{C}^2}{\Delta z^2} s_{\Delta t}^2 \quad (5.16)$$

$$= 4 \frac{\mathcal{C}^2}{\Delta z^2} \delta t^2 \quad (5.17)$$

$$(5.18)$$

Our squared variance on the index of refraction is thus (neglecting unknown systematic errors):

$$\delta n^2 =: s_n^2 = 4 \left(\frac{c}{\cos \theta_{min}} \right)^2 \left(\frac{1}{\Delta z^2} \delta t^2 + \frac{\Delta t^2}{\Delta z^4} \delta z^2 + \frac{\mathcal{C}^2}{\Delta z^2} \delta t^2 \right) \quad (5.19)$$

If we have more than 2 detectors, say N then the uncertainty on the fit can be assumed to be the RMS of the individual uncertainties:

$$\delta n = \sqrt{\sum_{i=0}^N \delta n_i^2} \quad (5.20)$$

Let's assume ϵ to be an absolute error. Now due to this inherent inaccuracy, the "global" uncertainty on n also has an additional error of $\pm \epsilon(\vec{r})n$ with \vec{r} the position of the balloon. Our final error on n is thus:

$$\delta n(\vec{r}) = \epsilon(\vec{r})n + \sqrt{\sum_{i=0}^N 4 \left(\frac{c}{\cos \theta_{min}} \right)^2 \left(\frac{1}{\Delta z_i^2} \delta t^2 + \frac{\Delta t_i^2}{\Delta z_i^4} \delta z^2 + \frac{\mathcal{C}_i^2}{\Delta z_i^2} \delta t^2 \right)} \quad (5.21)$$

⁵meaning if we have a measurement z_i the true value is within $z_i \pm \delta z$ with 95% certainty

If we assume the ϵ to overestimate the index of refraction the same way in real life as in the simulation however, our estimated n can be corrected as

$$n_{\text{corrected}}(\vec{r}) = \frac{n(\vec{r})}{\epsilon(\vec{r}) + 1} \quad (5.22)$$

and our error becomes only the second part of equation 5.21. As the error on the position of the channels is not yet fully known most of this section mainly serves as a future reference to calculate the additional errors on the indices of refraction that will be calculated in the next sections within this chapter. However the error on timing can be estimated from the sampling rate, as if we have a sampling rate of e.g 3.2GHz then the antenna will take a measurement every

$$\delta t = \frac{1}{3.2\text{GHz}} = 0.3125\text{ns} \quad (5.23)$$

So we can predict a measurement of the index of refraction, assuming ϵ to be a correction and $\delta z \ll$, to have an error of

$$\delta n(\vec{r})_{\text{corrected}} = (1 + \epsilon) \times \sqrt{\sum_{i=0}^N 4 \left(\frac{c}{\cos \theta_{min}} \right)^2 \left(\frac{1}{\Delta z_i^2} \delta t^2 + \frac{\mathcal{C}_i^2}{\Delta z_i^2} \delta t^2 \right)} \quad (5.24)$$

$$= 2(1 + \epsilon)\delta t \times \sqrt{\sum_{i=0}^N \left(\frac{c}{\cos \theta_{min}} \right)^2 \left(\frac{1}{\Delta z_i^2} + \frac{\mathcal{C}_i^2}{\Delta z_i^2} \right)} \quad (5.25)$$

$$= 2(1 + \epsilon)\delta t \times \sqrt{\sum_{i=0}^N \left(\frac{c}{\Delta z_i \cos \theta_{min}} \right)^2 (1 + \mathcal{C}_i^2)} \quad (5.26)$$

And if we only consider 2 detectors (which we will in most cases) this reduces to

$$\delta n(\vec{r})_{\text{corrected}} = 2(1 + \epsilon) \times c \left(\frac{\delta t}{\Delta z} \right) \times \left[\frac{\sqrt{1 + \mathcal{C}^2}}{\cos \theta_{min}} \right] \quad (5.27)$$

Note again that Δz is the **difference** in height between the two detectors and δt is the **accuracy** in timing (which gets determined by the sample rate of the antenna).

5.4 Fitting the index: Channels 0 and 3

Now that we know our goal to be feasible, let's analyse some data. As we'll start by just analysing one event, let's take one of the best events possible for our analysis. A close look at graph 5.5 shows that events under 5° at a height of 500m produce an ϵ of less than 0.22%, implying that if we measure n to be 1.7407 our ϵ will only be 0.0038. A good start will thus be finding moments when the balloon gets to within a 5% angle, note that ϵ is height dependent so we'll have to calculate it afterwards. After looping through all the balloon positional files and only outputting the < 5 ones we get some timeframes where balloons were actually close enough (note that < 5 almost never happens at low heights).

If we search in the DESY database ⁶ within the calculated timeframes for the particular detectors where the balloon gets close enough to, AND where the 403MHz signal coming from the Balloon (see figure 5.16) is detected in the deep channels, the events of the 7th of september stands out; at 11:28:10, just before the < 5 passby between 11:28:47 and 11:28:49, the balloon gets quite close to detector 23 and shows a clear 403MHz signal at the phased array, as shown in figure (???).

Now to calculate the differences in timing for this received signal, the code we built for this is called FitN.py and stored at the repository [projects-mt](#) under BaLLooN/RealData, let's go over the full code step by step:⁷

5.4.1 Spatial data

The first part we'll need to concern ourselves with is determining the relative positions of everything. The balloon data file and the time when the event took place are given, from these two both the latitudinal and longitudinal position and the elevation of the balloon at the given time are determined. We convert these three measurements to the ENU coordinate frame (x,y,z with respect to reference) and store it in the array *BalloonPosition*. The next step is to get the location of the detector, for this we first instantiate a detector object

```
1 det = NuRadioReco.detector.detector.Detector(json_file="RNO_season_2022.json")
```

The RNO season 2022 json file can be found on the official RNO-G github under "analysis-tools", then we update the detector to the time of the event and get the absolute position of our detector (station 23) via the `get_absolute_position` module:

```
1 stationlocation = det.get_absolute_position(station_id)
```

Where at the specific station this position is doesn't matter as we'll explain shortly. Now that we have both the position of our balloon and station in ENU coordinates, let's simplify the calculations by setting the detector as the origin. i.e our new balloon position will be

$$RelBalloon = BalloonPosition - StationPosition \quad (5.28)$$

And as we might want to plot this later, due to the cylindrical symmetry, we can rotate the coordinates to get rid of our y-axis. We can do this by defining the radius:

⁶<https://rnog-monitor.zeuthen.desy.de/>

⁷I advise the people who will continue this work to pull up the code side-by-side with this explanation

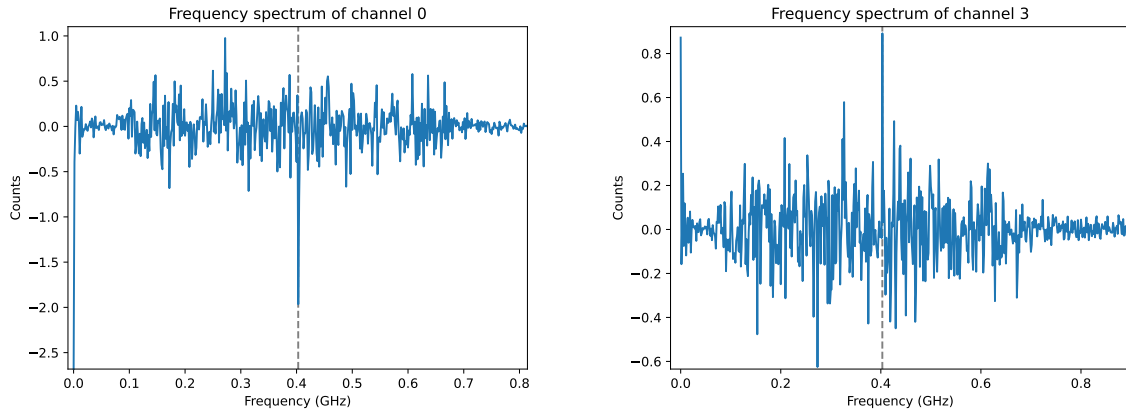


Figure 5.15: recorded frequencies on detector 23 at 2022/08/29 11:18:32

$$r := \sqrt{RelBalloon_x^2 + RelBalloon_y^2} \quad (5.29)$$

and just setting this equal to $Balloon_x$ and setting $Balloon_y$ to zero (equivalent to setting $\theta = 0$ in a rotation).

Now we don't have the position of our individual channels yet, only of the station itself, these can however easily be obtained using the `get_relative_position` module on our detector object, as we chose our station to be the center of the coordinate system, these relative positions are absolute positions of the channels in our frame of reference. Using these it thus doesn't matter where position of the station was defined.

5.4.2 Signal analysis and initial guesses

Now that we have our geometry, let's analyse the data for the channels 0 and 3, the data for a particular channel is stored in a channel object. From this object we can get the recorded voltages with the `get_trace()` module, the recorded times with the `get_times()` module, the recorded frequencies with the `get_frequencies()` and the recorded spectrum corresponding to these frequencies with `get_frequency_spectrum()`, note that the last two do a FFT on our data. We know that the signal sent out by the weather balloon is a sine wave with a frequency of 403MHz; as the data is measured in nanoseconds the frequency is:

$$f = 403.125\text{MHz} = 403.125 \times 10^{-3} \frac{1}{\text{ns}} \quad (5.30)$$

The recorded spectrum of both channels is given in figure 5.15, we observe a clear spike at 0.403GHz. Now note that there are a bunch of peaks both below 0.15GHz and above 0.6GHz, this is all non-physical noise as the Vpol antenna's range only goes from 0.15GHz to 0.6GHz [4] that's why we'll first pass this signal through a virtual butterworth bandpass filter.

After passing the signal through the filter we'd also like to upsample the signal as to increase the resolution, this can be done using the `resample()` module and we'll upsample towards 10GHz increasing our timely accuracy from 0.3125ns to 0.1ns. After filtering and upsampling we have some voltage response as shown in figure 5.17, we wish to find a sine wave in this signal.

To find a sine wave herein we'll radiotools' helper module `get_normalized_xcorr` which indirectly uses scipys signal correlation function but before using that we'll need a template to correlate

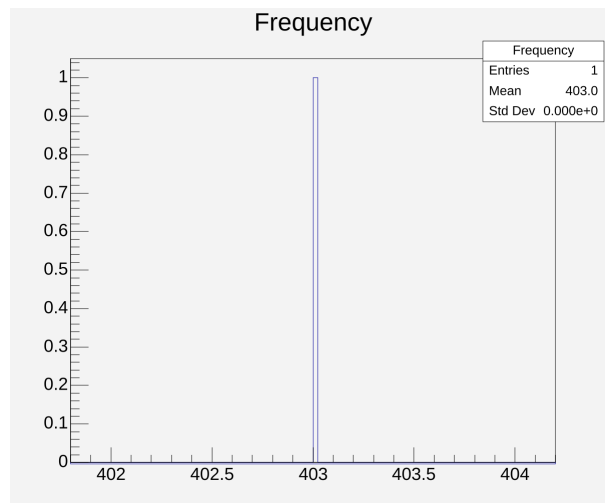


Figure 5.16: Frequencies sent out by the weather balloon

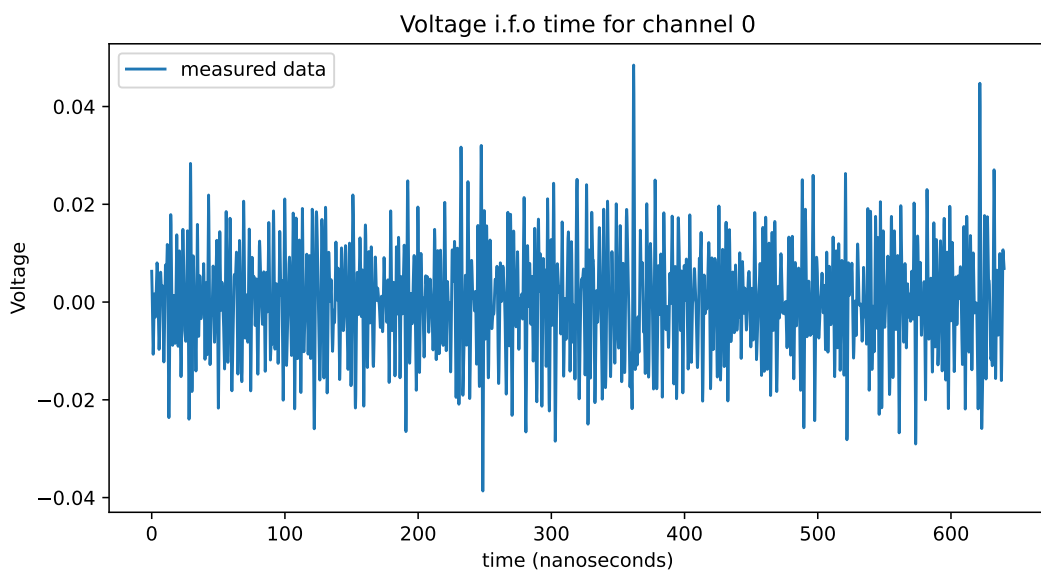


Figure 5.17: Recorded voltage i.f.o time in vpol antenna 0 after upsampling and passing through the butterworth filter

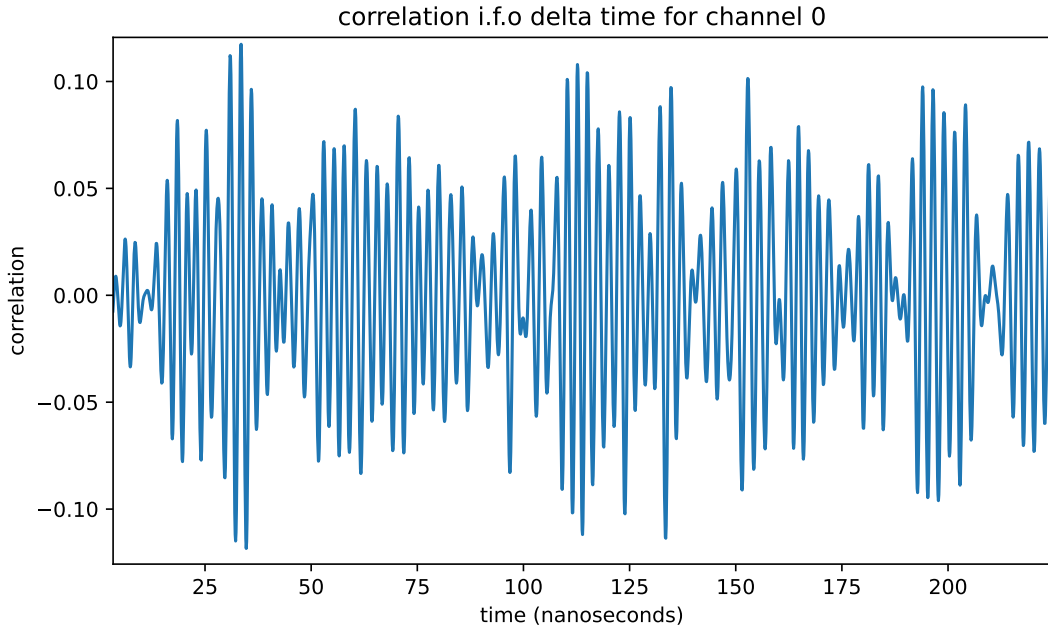


Figure 5.18: Zoom on the correlation i.f.o the time for channel 0

with the data. The template we'll be choosing is of course the sine function but it's important to notice that the channel has a certain sampling rate, namely now after upsampling, 10GHz.

Our template sine which we'll correlate to the data will also need to have this sampling rate, meaning that it needs to be stepwise defined with spaces of 0.1ns. Next we'll also need to give the sine a certain amplitude, as we don't have a system for finding this yet let's for now assume an amplitude $A = 0.007$ (this shouldn't impact the correlation). Our template thus looks like this:

$$\mathcal{S} = A \cdot \sin(\omega t) \quad (5.31)$$

with

$$\omega = 2\pi f \quad (5.32)$$

Herein t is an array going from 0 to $3/f$ as to be able to fit 3 periods with intervals of 0.1ns. This template gets automatically shifted by the radiotools correlation module with steps of 0.1ns and each time the correlation with the data gets computed. After this we get what's (partially) shown in figure 5.18. Herein the peaks represent the maximal correlation, if we now do the same for channel 3 we have two correlation functions, if we correlate these with eachother we'll get the difference in timing between the channels. This is easy to comprehend after taking a look at the illustration shown in figure 5.20. This cross correlation, after taking into account the cable delay, is shown in figure 5.19. Note that multiple peak correlations are present, to thus find out which one is the right one we'll do a simple simulation from which we know what the approximate time difference is and search in this neighbourhood.

Carrying out the full calculation we get the results which are presented below (note that the error on the epsilon corrected n was estimated using equation 5.26)

Depth (m)	Station id	channels	Run:Event	n _{exp}	n _{fit}	ε	n _{corr}
-93.231	23	0&3	800:1867	1.738	1.8188	4.6166%	1.739 ± 0.024

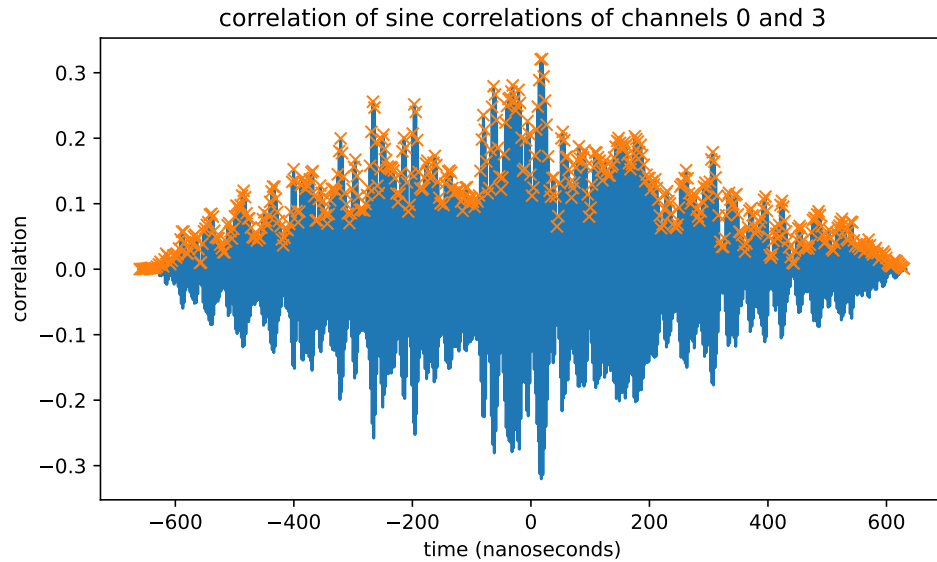


Figure 5.19: correlation of the previously, with sine, correlated dataset of channels 0 and 3, the orange marks indicate the peaks

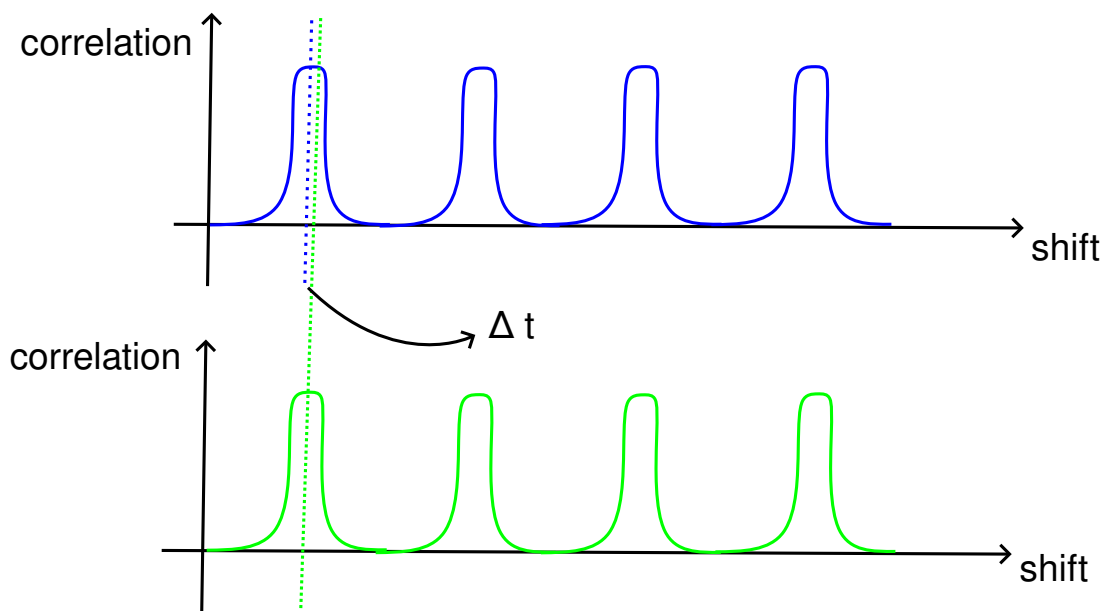


Figure 5.20: Illustration of how the different correlations with sine (above in blue being e.g. channel 0 and below in green channel 1) have a difference in timing between the peaks which can be found from correlating the two

Analogously we can use channels 0,1,2 and 3 in various combinations. In full all possibilities are (in order of increasing depth) ⁸⁹:

Depth (m)	Station id	channels	Run:Event	n _{exp}	n _{fit}	ε	n _{corr}
-92.24	23	2&3	800:1867	1.737	1.867	4.605%	1.784 ± 0.071
-92.75	23	1&3	800:1867	1.738	1.800	4.611%	1.721 ± 0.036
-93.23	23	0&3	800:1867	1.738	1.819	4.617%	1.739 ± 0.024
-93.24	23	1&2	800:1867	1.738	1.735	4.616%	1.659 ± 0.074
-93.73	23	0&2	800:1867	1.739	1.845	4.621%	1.763 ± 0.036
-94.23	23	0&1	800:1867	1.739	1.858	4.626%	1.776 ± 0.073

5.5 Channels 6 and 7

A very interesting depth is between channels 5 and 7 as, looking at the density profile shown in figure 3.2 this is where the actual density deviates the most from the models. The event we'll be using is recorded in detector 21 at the 26th of july 11:18:41 and falls within the < 5° mark:

Depth (m)	Station id	channels	Run:Event	n _{exp}	n _{fit}	ε	n _{corr}
-48.16	21	6&7	1441:117	1.640	1.631	-0.02%	1.631 ± 0.004
-58.38	21	5&7	1441:117	1.674	1.665	-0.23%	1.669 ± 0.002
-68.2	21	5&6	1441:117	1.698	1.692	0.02%	1.692 ± 0.003

Let's use Schytt's equation 3.13 to see where on the density vs depth curve these values lie:

$$n(z) \approx 1 + 0.78\rho/\rho_0 \quad (5.33)$$

$$\rho_0(n(z) - 1) \approx 0.78\rho \quad (5.34)$$

$$\frac{\rho_0}{0.78}(n(z) - 1) \approx \rho \quad (5.35)$$

$$\rho \approx 1175.641(n(z) - 1) \frac{\text{kg}}{\text{m}^3} \quad (5.36)$$

$$(5.37)$$

The error propagation is also quite easily found:

$$\delta\rho = 1175.641\delta n \quad (5.38)$$

If we use these equations the corrected indices of refraction correspond to the densities:

Depth (m)	ρ _{corr}
-48.16	741.830 ± 4.703
-58.38	786.504 ± 2.351
-68.2	813.544 ± 3.527

If we plot this we get what's shown in figure 5.21

⁸In all calculations the channel 1 had the least good signal, as such if these calculations ever get revised try to take this into account

⁹we also left out the possibility of combinations as 0&1&2&3 as the error would be too large but these are possible with the program

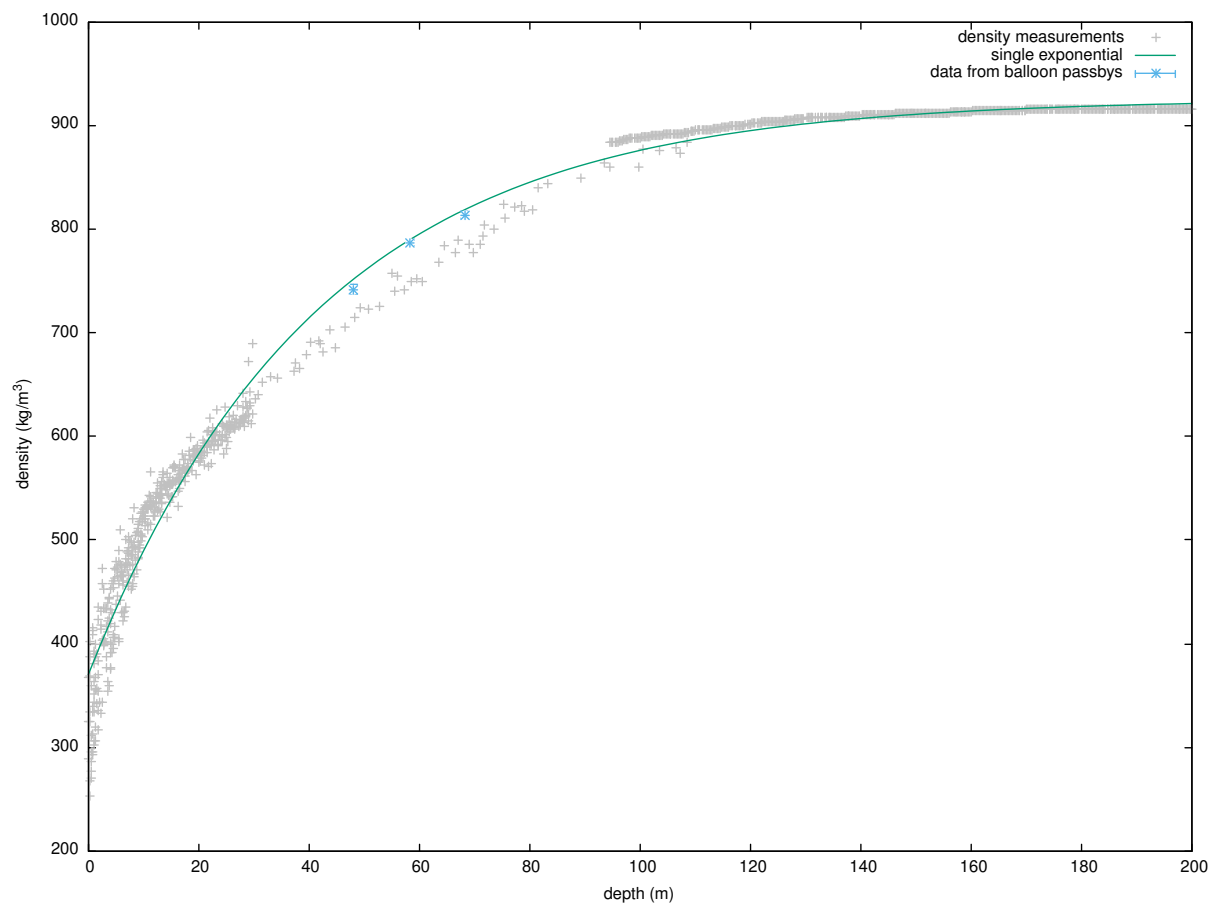


Figure 5.21: graph showing where the balloon data density is with respect to the other measurements and the exponential model

CHAPTER

6

TO BE DELETED

Now going through the full calculation (i.e minimizing the correlation function for different n given the time difference and finding the minimal distance between reconstruction and balloon position)¹ we get that the index for refraction at a depth of 47.714m is 1.6061, which is a fairly good estimate as, looking at the measurements depicted in figure 3.2 a depth of 47.7m would correspond to a density of about 710kg/m^3 , using Schytts equation this would thus give an index of refraction of 1.603. Now using the positional data we can calculate the relative accuracy ϵ which comes to be about 0.39%. Our final answer is thus:

depth (m)	station number	run used	event_id used	channels used	n
-47.714	23	691	489	6,7	1.606 ± 0.006

Which has the expected answer within the margin of error. We are aware that this event also shows a peak in the frequency spectrum for channel 5 but the data deviates slightly from an AM signal and thus didn't seem to be usable due to the difficulty of fitting it.

¹Note that we used Snell's law

6.1 Fitting the index: deep components

6.1.1 Station 23 run 800 event 1867 Channels 0 and 3

Using guesses $\phi_2^0 = -786.91$ & $\phi_2^3 = -782$, traveltimes [4822.41659697 4806.73065199] are found which have nearly the same difference and size as the simulated [4822.16,4805.80]. The minimal correlation was found to be 0.334ns and yielded 1.7475 as index of refraction at a depth of -93.231m. Epsilon is calculated to be 4.865% for this Balloon position, our final result is thus:

depth (m)	station number	run used	event_id used	channels used	n
-93.231	23	800	1867	0,3	1.748 ± 0.085

From analysis of the density we expect an index of refraction of 1.73 which lies inside our confidence interval.

6.2 Special test: Channels 7 and 13

depth (m)	station number	run used	event_id used	channels used	n
-19.11	23	691	489	7,13	1.3777 ± 0.117

This test isn't to be used as the error is too large but it might be useful to know that a plane wave reconstruction with one of the nearest deep components and a surface component is possible.

CONCLUSION

Proposal of improved measurements

As this method seems to be a viable way of measuring the index of refraction, it might be a good idea to have a more controllable radio wave source fly closer to the detectors to make more accurate measurements, e.g an autonomous² drone with an antenna strapped to it. Assuming Schytt's equation to hold completely, ideally we'd like data inbetween the depths of 20-100m as density measurements are few there as depicted on figure 3.2 which is possible to achieve using this method as detectors span this range.

It would also help in the fitting of the AM signal is the message signal had a longer frequency making it less difficult to fit.

²as to not have it need a radio controller, causing RF interference and also as autonomous GNSS positioning are always more accurate than humans

APPENDIX

A

LIST OF ABBREVIATIONS

- **AM:** Amplitude Modulated
- **CMB:** Cosmic Microwave Background
- **DAQ:** Data AQuisition system
- **DnR:** Direct aNd Refracted
- **FFT** Fast Fourier Transform
- **GRBs:** Gamma-Ray Bursts
- **RADIANT:** RAdio DIgitizer and Auxiliary Neutrino Trigger
- **RNO-G:** Radio Neutrino Observatory in Greenland
- **UHE:** Ultra High Energy

APPENDIX

B

BALLOON PASSBYS UNDER 5° IN THE SUMMER OF 2022

Balloon filename (gpx)	station	expected timeframe
SMT_20220907_112500.gpx	23.00	2022-09-07 11:28:47+00:00 till 2022-09-07 11:28:49+00:00
SMT_20220728_112143.gpx	12.00	2022-07-28 11:36:42+00:00 till 2022-07-28 11:37:44+00:00
SMT_20220728_112143.gpx	11.00	2022-07-28 11:34:00+00:00 till 2022-07-28 11:35:37+00:00
SMT_20220728_112143.gpx	13.00	2022-07-28 11:38:18+00:00 till 2022-07-28 11:39:13+00:00
SMT_20220723_231622.gpx	21.00	2022-07-23 23:25:19+00:00 till 2022-07-23 23:27:24+00:00
SMT_20220723_231622.gpx	22.00	2022-07-23 23:31:22+00:00 till 2022-07-23 23:33:50+00:00
SMT_20220930_231507.gpx	13.00	2022-09-30 23:19:22+00:00 till 2022-09-30 23:19:23+00:00

**APPENDIX B. BALLOON PASSBYS UNDER 5°
IN THE SUMMER OF 2022**

Balloon filename (gpx)	station	expected timeframe
SMT_20220904_111459.gpx	21.00	2022-09-04 11:17:00+00:00 till 2022-09-04 11:17:49+00:00
SMT_20220904_111459.gpx	22.00	2022-09-04 11:21:12+00:00 till 2022-09-04 11:21:29+00:00
SMT_20220726_111605.gpx	21.00	2022-07-26 11:18:31+00:00 till 2022-07-26 11:18:47+00:00
SMT_20220726_111605.gpx	23.00	2022-07-26 11:27:32+00:00 till 2022-07-26 11:28:24+00:00
SMT_20220726_111605.gpx	24.00	2022-07-26 11:34:42+00:00 till 2022-07-26 11:40:36+00:00
SMT_20220826_113003.gpx	21.00	2022-08-26 11:32:14+00:00 till 2022-08-26 11:32:30+00:00
SMT_20220826_113003.gpx	13.00	2022-08-26 11:38:18+00:00 till 2022-08-26 11:39:04+00:00
SMT_20220714_231645.gpx	11.00	2022-07-14 23:30:57+00:00 till 2022-07-14 23:31:40+00:00
SMT_20220701_111515.gpx	11.00	2022-07-01 11:22:57+00:00 till 2022-07-01 11:25:30+00:00
SMT_20220725_112511.gpx	12.00	2022-07-25 11:29:41+00:00 till 2022-07-25 11:30:12+00:00
SMT_20220703_111803.gpx	24.00	2022-07-03 11:47:29+00:00 till 2022-07-03 11:50:43+00:00
SMT_20220820_111609.gpx	12.00	2022-08-20 11:24:37+00:00 till 2022-08-20 11:25:33+00:00
SMT_20220623_231633.gpx	13.00	2022-06-23 23:29:52+00:00 till 2022-06-23 23:30:59+00:00
SMT_20220623_231633.gpx	22.00	2022-06-23 23:23:50+00:00 till 2022-06-23 23:25:39+00:00
SMT_20220703_231627.gpx	21.00	2022-07-04 00:21:36+00:00 till 2022-07-04 00:42:14+00:00
SMT_20220703_231627.gpx	12.00	2022-07-04 00:32:03+00:00 till 2022-07-04 00:45:17+00:00
SMT_20220703_231627.gpx	11.00	2022-07-04 00:32:02+00:00 till 2022-07-04 00:47:35+00:00
SMT_20220703_231627.gpx	22.00	2022-07-04 00:21:47+00:00 till 2022-07-04 00:40:30+00:00
SMT_20220703_231627.gpx	23.00	2022-07-04 00:26:31+00:00 till 2022-07-04 00:34:55+00:00
SMT_20220624_231528.gpx	24.00	2022-06-25 00:29:26+00:00 till 2022-06-25 00:35:21+00:00
SMT_20220916_231807.gpx	22.00	2022-09-16 23:21:25+00:00 till 2022-09-16 23:21:49+00:00
SMT_20220908_111450.gpx	12.00	2022-09-08 11:20:23+00:00 till 2022-09-08 11:21:08+00:00
SMT_20220908_111450.gpx	13.00	2022-09-08 11:23:08+00:00 till 2022-09-08 11:23:54+00:00
SMT_20220817_111600.gpx	21.00	2022-08-17 11:31:37+00:00 till 2022-08-17 11:33:56+00:00
SMT_20220729_112533.gpx	11.00	2022-07-29 12:26:35+00:00 till 2022-07-29 12:31:35+00:00
SMT_20220907_231621.gpx	24.00	2022-09-07 23:24:23+00:00 till 2022-09-07 23:24:51+00:00
SMT_20220630_231835.gpx	21.00	2022-07-01 00:18:16+00:00 till 2022-07-01 00:32:45+00:00
SMT_20220630_231835.gpx	12.00	2022-07-01 00:25:19+00:00 till 2022-07-01 00:38:40+00:00
SMT_20220630_231835.gpx	11.00	2022-07-01 00:24:24+00:00 till 2022-07-01 00:37:58+00:00
SMT_20220630_231835.gpx	13.00	2022-07-01 00:30:30+00:00 till 2022-07-01 00:37:06+00:00
SMT_20220630_231835.gpx	22.00	2022-07-01 00:22:24+00:00 till 2022-07-01 00:34:12+00:00
SMT_20220826_231852.gpx	23.00	2022-08-26 23:27:09+00:00 till 2022-08-26 23:27:51+00:00
SMT_20220826_231852.gpx	24.00	2022-08-26 23:29:02+00:00 till 2022-08-26 23:29:48+00:00
SMT_20220624_111844.gpx	13.00	2022-06-24 11:33:51+00:00 till 2022-06-24 11:34:42+00:00
SMT_20220624_111844.gpx	22.00	2022-06-24 11:31:46+00:00 till 2022-06-24 11:32:35+00:00
SMT_20220707_112434.gpx	21.00	2022-07-07 12:31:12+00:00 till 2022-07-07 12:48:00+00:00
SMT_20220707_112434.gpx	12.00	2022-07-07 12:37:07+00:00 till 2022-07-07 12:49:22+00:00
SMT_20220707_112434.gpx	11.00	2022-07-07 12:36:00+00:00 till 2022-07-07 12:49:22+00:00
SMT_20220707_112434.gpx	13.00	2022-07-07 12:41:38+00:00 till 2022-07-07 12:49:22+00:00
SMT_20220707_112434.gpx	22.00	2022-07-07 12:34:46+00:00 till 2022-07-07 12:49:22+00:00
SMT_20220707_112434.gpx	23.00	2022-07-07 12:41:33+00:00 till 2022-07-07 12:48:09+00:00
SMT_20220829_111459.gpx	23.00	2022-08-29 11:18:46+00:00 till 2022-08-29 11:18:58+00:00
SMT_20220829_111459.gpx	24.00	2022-08-29 11:19:52+00:00 till 2022-08-29 11:20:10+00:00
SMT_20220727_232120.gpx	21.00	2022-07-27 23:24:53+00:00 till 2022-07-27 23:25:26+00:00
SMT_20220719_231514.gpx	11.00	2022-07-19 23:23:48+00:00 till 2022-07-19 23:26:06+00:00
SMT_20220807_231525.gpx	11.00	2022-08-07 23:18:35+00:00 till 2022-08-07 23:19:02+00:00
SMT_20220725_231505.gpx	13.00	2022-07-26 00:41:45+00:00 till 2022-07-26 00:53:49+00:00
SMT_20220725_231505.gpx	22.00	2022-07-25 23:22:13+00:00 till 2022-07-25 23:23:48+00:00
SMT_20220725_231505.gpx	23.00	2022-07-25 23:26:39+00:00 till 2022-07-26 00:48:25+00:00

**APPENDIX B. BALLOON PASSBYS UNDER 5°
IN THE SUMMER OF 2022**

Balloon filename (gpx)	station	expected timeframe
SMT_20220725_231505.gpx	23.00	2022-07-25 23:26:39+00:00 till 2022-07-26 00:48:25+00:00
SMT_20220725_231505.gpx	24.00	2022-07-26 00:35:23+00:00 till 2022-07-26 00:49:53+00:00
SMT_20220928_111604.gpx	11.00	2022-09-28 11:34:13+00:00 till 2022-09-28 11:35:36+00:00
SMT_20220808_231507.gpx	11.00	2022-08-08 23:18:40+00:00 till 2022-08-08 23:19:08+00:00
SMT_20220816_232314.gpx	22.00	2022-08-16 23:34:34+00:00 till 2022-08-16 23:35:09+00:00
SMT_20220704_231605.gpx	21.00	2022-07-04 23:23:47+00:00 till 2022-07-04 23:27:33+00:00
SMT_20220630_112143.gpx	21.00	2022-06-30 12:26:56+00:00 till 2022-06-30 12:38:03+00:00
SMT_20220630_112143.gpx	12.00	2022-06-30 12:31:57+00:00 till 2022-06-30 12:44:25+00:00
SMT_20220630_112143.gpx	11.00	2022-06-30 12:31:26+00:00 till 2022-06-30 12:42:23+00:00
SMT_20220630_112143.gpx	13.00	2022-06-30 12:34:40+00:00 till 2022-06-30 12:44:06+00:00
SMT_20220630_112143.gpx	22.00	2022-06-30 12:28:56+00:00 till 2022-06-30 12:39:23+00:00
SMT_20220630_112143.gpx	23.00	2022-06-30 12:33:15+00:00 till 2022-06-30 12:37:09+00:00
SMT_20220704_112103.gpx	21.00	2022-07-04 11:49:20+00:00 till 2022-07-04 11:55:43+00:00
SMT_20220704_112103.gpx	11.00	2022-07-04 11:45:32+00:00 till 2022-07-04 11:51:31+00:00
SMT_20220704_112103.gpx	13.00	2022-07-04 12:10:16+00:00 till 2022-07-04 12:11:52+00:00
SMT_20220704_112103.gpx	22.00	2022-07-04 11:52:45+00:00 till 2022-07-04 12:02:35+00:00
SMT_20220704_112103.gpx	23.00	2022-07-04 11:58:37+00:00 till 2022-07-04 12:16:54+00:00
SMT_20220704_112103.gpx	24.00	2022-07-04 12:06:21+00:00 till 2022-07-04 12:25:28+00:00
SMT_20220720_111442.gpx	23.00	2022-07-20 11:46:26+00:00 till 2022-07-20 11:50:05+00:00
SMT_20220720_111442.gpx	24.00	2022-07-20 11:50:53+00:00 till 2022-07-20 12:03:52+00:00
SMT_20220829_231438.gpx	22.00	2022-08-29 23:16:33+00:00 till 2022-08-29 23:16:38+00:00
SMT_20220829_231438.gpx	23.00	2022-08-29 23:17:45+00:00 till 2022-08-29 23:17:58+00:00
SMT_20220921_231851.gpx	12.00	2022-09-22 10:46:18+00:00 till 2022-09-22 10:46:19+00:00
SMT_20220821_111511.gpx	21.00	2022-08-21 12:39:53+00:00 till 2022-08-21 12:56:06+00:00
SMT_20220821_111511.gpx	12.00	2022-08-21 12:51:06+00:00 till 2022-08-21 12:56:06+00:00
SMT_20220821_111511.gpx	11.00	2022-08-21 12:51:32+00:00 till 2022-08-21 12:56:06+00:00
SMT_20220821_111511.gpx	13.00	2022-08-21 12:52:27+00:00 till 2022-08-21 12:56:06+00:00
SMT_20220821_111511.gpx	22.00	2022-08-21 12:40:26+00:00 till 2022-08-21 12:56:06+00:00
SMT_20220821_111511.gpx	23.00	2022-08-21 12:43:03+00:00 till 2022-08-21 12:56:06+00:00
SMT_20220724_231539.gpx	11.00	2022-07-24 23:20:04+00:00 till 2022-07-24 23:21:11+00:00
SMT_20220827_111534.gpx	24.00	2022-08-27 11:23:00+00:00 till 2022-08-27 11:23:07+00:00
SMT_20220625_111630.gpx	21.00	2022-06-25 12:27:31+00:00 till 2022-06-25 12:35:22+00:00
SMT_20220625_111630.gpx	12.00	2022-06-25 12:30:09+00:00 till 2022-06-25 12:39:40+00:00
SMT_20220625_111630.gpx	11.00	2022-06-25 12:32:45+00:00 till 2022-06-25 12:37:21+00:00
SMT_20220625_111630.gpx	13.00	2022-06-25 12:30:42+00:00 till 2022-06-25 12:40:11+00:00
SMT_20220625_111630.gpx	22.00	2022-06-25 12:27:03+00:00 till 2022-06-25 12:37:11+00:00
SMT_20220625_111630.gpx	23.00	2022-06-25 12:28:31+00:00 till 2022-06-25 12:37:18+00:00

APPENDIX

C

BALLOON PASSBYS UNDER 10° IN THE SUMMER OF 2022

Balloon filename (gpx)	station	expected timeframe
SMT_20220719_231514.gpx	21	2022-07-19 23:19:46+00:00 till 2022-07-19 23:20:41+00:00
SMT_20220719_231514.gpx	11	2022-07-19 23:22:44+00:00 till 2022-07-19 23:27:19+00:00
SMT_20220831_111419.gpx	11	2022-08-31 11:16:20+00:00 till 2022-08-31 11:16:26+00:00
SMT_20220625_111630.gpx	21	2022-06-25 12:22:22+00:00 till 2022-06-25 12:40:57+00:00
SMT_20220625_111630.gpx	12	2022-06-25 12:25:55+00:00 till 2022-06-25 12:45:40+00:00
SMT_20220625_111630.gpx	11	2022-06-25 12:25:58+00:00 till 2022-06-25 12:45:09+00:00
SMT_20220625_111630.gpx	13	2022-06-25 12:26:44+00:00 till 2022-06-25 12:45:40+00:00
SMT_20220625_111630.gpx	22	2022-06-25 12:22:25+00:00 till 2022-06-25 12:42:40+00:00
SMT_20220625_111630.gpx	23	2022-06-25 12:24:10+00:00 till 2022-06-25 12:43:09+00:00
SMT_20220625_111630.gpx	24	2022-06-25 12:26:32+00:00 till 2022-06-25 12:42:24+00:00
SMT_20220826_113003.gpx	21	2022-08-26 11:32:04+00:00 till 2022-08-26 11:32:42+00:00
SMT_20220826_113003.gpx	13	2022-08-26 11:37:48+00:00 till 2022-08-26 11:39:40+00:00
SMT_20220626_112912.gpx	11	2022-06-26 11:35:52+00:00 till 2022-06-26 11:37:32+00:00
SMT_20220808_231507.gpx	11	2022-08-08 23:18:27+00:00 till 2022-08-08 23:19:24+00:00

**APPENDIX C. BALLOON PASSBYS UNDER 10°
IN THE SUMMER OF 2022**

Balloon filename (gpx)	station	expected timeframe
SMT_20220724_231539.gpx	11	2022-07-24 23:19:27+00:00 till 2022-07-24 23:21:58+00:00
SMT_20220724_231539.gpx	13	2022-07-25 00:19:35+00:00 till 2022-07-25 00:32:09+00:00
SMT_20220829_231438.gpx	22	2022-08-29 23:16:29+00:00 till 2022-08-29 23:16:42+00:00
SMT_20220829_231438.gpx	23	2022-08-29 23:17:39+00:00 till 2022-08-29 23:18:04+00:00
SMT_20220829_231438.gpx	24	2022-08-29 23:18:59+00:00 till 2022-08-29 23:19:22+00:00
SMT_20220916_231807.gpx	21	2022-09-16 23:19:09+00:00 till 2022-09-16 23:19:17+00:00
SMT_20220916_231807.gpx	22	2022-09-16 23:21:13+00:00 till 2022-09-16 23:22:03+00:00
SMT_20220816_232314.gpx	22	2022-08-16 23:33:11+00:00 till 2022-08-16 23:37:34+00:00
SMT_20220907_112500.gpx	23	2022-09-07 11:28:37+00:00 till 2022-09-07 11:28:59+00:00
SMT_20220907_112500.gpx	24	2022-09-07 11:29:35+00:00 till 2022-09-07 11:29:53+00:00
SMT_20220628_231514.gpx	12	2022-06-28 23:19:37+00:00 till 2022-06-28 23:20:55+00:00
SMT_20220630_112143.gpx	21	2022-06-30 12:21:02+00:00 till 2022-06-30 12:46:53+00:00
SMT_20220630_112143.gpx	12	2022-06-30 12:26:35+00:00 till 2022-06-30 12:48:30+00:00
SMT_20220630_112143.gpx	11	2022-06-30 12:25:33+00:00 till 2022-06-30 12:48:30+00:00
SMT_20220630_112143.gpx	13	2022-06-30 12:28:56+00:00 till 2022-06-30 12:48:30+00:00
SMT_20220630_112143.gpx	22	2022-06-30 12:23:21+00:00 till 2022-06-30 12:47:42+00:00
SMT_20220630_112143.gpx	23	2022-06-30 12:26:20+00:00 till 2022-06-30 12:47:25+00:00
SMT_20220630_112143.gpx	24	2022-06-30 12:30:34+00:00 till 2022-06-30 12:46:14+00:00
SMT_20220725_231505.gpx	21	2022-07-25 23:17:47+00:00 till 2022-07-26 00:53:39+00:00
SMT_20220725_231505.gpx	12	2022-07-26 00:38:19+00:00 till 2022-07-26 00:55:04+00:00
SMT_20220725_231505.gpx	11	2022-07-26 00:45:41+00:00 till 2022-07-26 00:55:04+00:00
SMT_20220725_231505.gpx	13	2022-07-26 00:34:56+00:00 till 2022-07-26 00:55:04+00:00
SMT_20220725_231505.gpx	22	2022-07-25 23:21:41+00:00 till 2022-07-26 00:55:04+00:00
SMT_20220725_231505.gpx	23	2022-07-25 23:25:16+00:00 till 2022-07-26 00:55:04+00:00
SMT_20220725_231505.gpx	24	2022-07-26 00:25:43+00:00 till 2022-07-26 00:55:04+00:00
SMT_20220703_111803.gpx	22	2022-07-03 11:40:24+00:00 till 2022-07-03 11:42:55+00:00
SMT_20220703_111803.gpx	23	2022-07-03 11:42:26+00:00 till 2022-07-03 11:49:33+00:00
SMT_20220703_111803.gpx	24	2022-07-03 11:45:29+00:00 till 2022-07-03 11:52:37+00:00
SMT_20220820_111609.gpx	21	2022-08-20 11:19:36+00:00 till 2022-08-20 11:21:16+00:00
SMT_20220820_111609.gpx	12	2022-08-20 11:24:02+00:00 till 2022-08-20 11:26:23+00:00
SMT_20220624_231528.gpx	12	2022-06-25 00:33:09+00:00 till 2022-06-25 00:40:51+00:00
SMT_20220624_231528.gpx	13	2022-06-25 00:28:45+00:00 till 2022-06-25 00:40:56+00:00
SMT_20220624_231528.gpx	22	2022-06-25 00:31:15+00:00 till 2022-06-25 00:34:40+00:00
SMT_20220624_231528.gpx	23	2022-06-25 00:24:52+00:00 till 2022-06-25 00:40:56+00:00
SMT_20220624_231528.gpx	24	2022-06-25 00:23:18+00:00 till 2022-06-25 00:40:56+00:00
SMT_20220701_111515.gpx	11	2022-07-01 11:21:58+00:00 till 2022-07-01 11:26:31+00:00
SMT_20220930_111518.gpx	12	2022-09-30 11:19:46+00:00 till 2022-09-30 11:20:04+00:00
SMT_20220821_111511.gpx	21	2022-08-21 12:30:15+00:00 till 2022-08-21 12:56:06+00:00
SMT_20220821_111511.gpx	12	2022-08-21 12:37:45+00:00 till 2022-08-21 12:56:06+00:00
SMT_20220821_111511.gpx	11	2022-08-21 12:37:28+00:00 till 2022-08-21 12:56:06+00:00
SMT_20220821_111511.gpx	13	2022-08-21 12:39:39+00:00 till 2022-08-21 12:56:06+00:00
SMT_20220821_111511.gpx	22	2022-08-21 12:31:58+00:00 till 2022-08-21 12:56:06+00:00
SMT_20220821_111511.gpx	23	2022-08-21 12:33:47+00:00 till 2022-08-21 12:56:06+00:00
SMT_20220821_111511.gpx	24	2022-08-21 12:39:51+00:00 till 2022-08-21 12:56:06+00:00
SMT_20220813_112235.gpx	21	2022-08-13 11:12:14+00:00 till 2022-08-13 11:12:14+00:00
SMT_20220714_231645.gpx	12	2022-07-14 23:33:22+00:00 till 2022-07-14 23:38:49+00:00
SMT_20220714_231645.gpx	11	2022-07-14 23:27:54+00:00 till 2022-07-14 23:35:34+00:00
SMT_20220714_231645.gpx	13	2022-07-14 23:37:48+00:00 till 2022-07-14 23:46:03+00:00
SMT_20220723_231622.gpx	21	2022-07-23 23:21:03+00:00 till 2022-07-23 23:30:26+00:00

**APPENDIX C. BALLOON PASSBYS UNDER 10°
IN THE SUMMER OF 2022**

Balloon filename (gpx)	station	expected timeframe
SMT_20220723_231622.gpx	21	2022-07-23 23:21:03+00:00 till 2022-07-23 23:30:26+00:00
SMT_20220723_231622.gpx	22	2022-07-23 23:30:12+00:00 till 2022-07-23 23:35:27+00:00
SMT_20220723_231622.gpx	23	2022-07-23 23:33:26+00:00 till 2022-07-23 23:37:57+00:00
SMT_20220723_231622.gpx	24	2022-07-23 23:36:33+00:00 till 2022-07-23 23:39:18+00:00
SMT_20220701_231934.gpx	22	2022-07-01 23:08:19+00:00 till 2022-07-01 23:08:19+00:00
SMT_20220701_231934.gpx	23	2022-07-01 23:08:19+00:00 till 2022-07-01 23:08:19+00:00
SMT_20220830_231921.gpx	12	2022-08-30 23:22:15+00:00 till 2022-08-30 23:22:31+00:00
SMT_20220706_231615.gpx	22	2022-07-07 00:34:24+00:00 till 2022-07-07 00:35:15+00:00
SMT_20220706_231615.gpx	23	2022-07-07 00:33:30+00:00 till 2022-07-07 00:35:15+00:00
SMT_20220706_231615.gpx	24	2022-07-07 00:33:50+00:00 till 2022-07-07 00:35:15+00:00
SMT_20220728_112143.gpx	12	2022-07-28 11:36:04+00:00 till 2022-07-28 11:38:16+00:00
SMT_20220728_112143.gpx	11	2022-07-28 11:32:06+00:00 till 2022-07-28 11:36:28+00:00
SMT_20220728_112143.gpx	13	2022-07-28 11:37:48+00:00 till 2022-07-28 11:39:49+00:00
SMT_20220716_111633.gpx	21	2022-07-16 12:05:05+00:00 till 2022-07-16 12:20:22+00:00
SMT_20220716_111633.gpx	12	2022-07-16 12:10:53+00:00 till 2022-07-16 12:24:07+00:00
SMT_20220716_111633.gpx	11	2022-07-16 12:08:23+00:00 till 2022-07-16 12:25:43+00:00
SMT_20220716_111633.gpx	22	2022-07-16 12:09:06+00:00 till 2022-07-16 12:18:35+00:00
SMT_20220715_231621.gpx	21	2022-07-16 00:08:58+00:00 till 2022-07-16 00:12:03+00:00
SMT_20220726_111605.gpx	21	2022-07-26 11:18:19+00:00 till 2022-07-26 11:19:03+00:00
SMT_20220726_111605.gpx	12	2022-07-26 12:20:14+00:00 till 2022-07-26 12:21:53+00:00
SMT_20220726_111605.gpx	13	2022-07-26 12:06:52+00:00 till 2022-07-26 12:30:56+00:00
SMT_20220726_111605.gpx	22	2022-07-26 11:21:46+00:00 till 2022-07-26 11:24:39+00:00
SMT_20220726_111605.gpx	23	2022-07-26 11:26:09+00:00 till 2022-07-26 12:22:24+00:00
SMT_20220726_111605.gpx	24	2022-07-26 11:31:17+00:00 till 2022-07-26 12:25:10+00:00
SMT_20220726_231510.gpx	11	2022-07-26 23:31:39+00:00 till 2022-07-26 23:43:04+00:00
SMT_20220724_111936.gpx	11	2022-07-24 11:24:45+00:00 till 2022-07-24 11:27:03+00:00
SMT_20220724_111936.gpx	13	2022-07-24 12:23:16+00:00 till 2022-07-24 12:33:48+00:00
SMT_20220724_111936.gpx	24	2022-07-24 12:12:44+00:00 till 2022-07-24 12:29:27+00:00
SMT_20220820_231751.gpx	13	2022-08-20 23:41:03+00:00 till 2022-08-20 23:45:01+00:00
SMT_20220820_231751.gpx	22	2022-08-20 23:39:20+00:00 till 2022-08-20 23:41:29+00:00
SMT_20220820_231751.gpx	23	2022-08-20 23:39:47+00:00 till 2022-08-20 23:42:41+00:00
SMT_20220703_231627.gpx	21	2022-07-03 23:58:58+00:00 till 2022-07-04 00:51:57+00:00
SMT_20220703_231627.gpx	12	2022-07-04 00:19:47+00:00 till 2022-07-04 00:52:09+00:00
SMT_20220703_231627.gpx	11	2022-07-04 00:19:37+00:00 till 2022-07-04 00:52:09+00:00
SMT_20220703_231627.gpx	13	2022-07-04 00:22:04+00:00 till 2022-07-04 00:52:07+00:00
SMT_20220703_231627.gpx	22	2022-07-04 00:14:09+00:00 till 2022-07-04 00:50:28+00:00
SMT_20220703_231627.gpx	23	2022-07-04 00:17:51+00:00 till 2022-07-04 00:48:29+00:00
SMT_20220703_231627.gpx	24	2022-07-04 00:23:40+00:00 till 2022-07-04 00:42:26+00:00
SMT_20220816_111548.gpx	11	2022-08-16 11:19:06+00:00 till 2022-08-16 11:20:08+00:00
SMT_20220704_231605.gpx	21	2022-07-04 23:21:14+00:00 till 2022-07-04 23:29:47+00:00
SMT_20220704_231605.gpx	22	2022-07-05 00:45:35+00:00 till 2022-07-05 00:46:21+00:00
SMT_20220704_231605.gpx	23	2022-07-05 00:44:35+00:00 till 2022-07-05 00:46:21+00:00
SMT_20220704_231605.gpx	24	2022-07-05 00:44:08+00:00 till 2022-07-05 00:46:21+00:00
SMT_20220921_231851.gpx	12	2022-09-22 10:46:18+00:00 till 2022-09-22 10:46:20+00:00
SMT_20220921_231851.gpx	13	2022-09-22 10:46:21+00:00 till 2022-09-22 10:46:22+00:00
SMT_20220630_231835.gpx	21	2022-07-01 00:11:25+00:00 till 2022-07-01 00:39:49+00:00
SMT_20220630_231835.gpx	12	2022-07-01 00:19:34+00:00 till 2022-07-01 00:45:51+00:00
SMT_20220630_231835.gpx	11	2022-07-01 00:17:35+00:00 till 2022-07-01 00:45:17+00:00

**APPENDIX C. BALLOON PASSBYS UNDER 10°
IN THE SUMMER OF 2022**

Balloon filename (gpx)	station	expected timeframe
SMT_20220630_231835.gpx	13	2022-07-01 00:23:23+00:00 till 2022-07-01 00:45:28+00:00
SMT_20220630_231835.gpx	22	2022-07-01 00:17:04+00:00 till 2022-07-01 00:40:11+00:00
SMT_20220630_231835.gpx	23	2022-07-01 00:21:11+00:00 till 2022-07-01 00:39:32+00:00
SMT_20220630_231835.gpx	24	2022-07-01 00:26:47+00:00 till 2022-07-01 00:37:45+00:00
SMT_20220807_231525.gpx	11	2022-08-07 23:18:24+00:00 till 2022-08-07 23:19:22+00:00
SMT_20220727_232120.gpx	21	2022-07-27 23:24:29+00:00 till 2022-07-27 23:25:46+00:00
SMT_20220727_232120.gpx	22	2022-07-27 23:27:22+00:00 till 2022-07-27 23:27:30+00:00
SMT_20220727_232120.gpx	23	2022-07-27 23:31:39+00:00 till 2022-07-27 23:32:39+00:00
SMT_20220727_232120.gpx	24	2022-07-27 23:33:29+00:00 till 2022-07-27 23:36:31+00:00
SMT_20220707_112434.gpx	21	2022-07-07 12:23:11+00:00 till 2022-07-07 12:49:22+00:00
SMT_20220707_112434.gpx	12	2022-07-07 12:31:06+00:00 till 2022-07-07 12:49:22+00:00
SMT_20220707_112434.gpx	11	2022-07-07 12:28:16+00:00 till 2022-07-07 12:49:22+00:00
SMT_20220707_112434.gpx	13	2022-07-07 12:34:19+00:00 till 2022-07-07 12:49:22+00:00
SMT_20220707_112434.gpx	22	2022-07-07 12:26:02+00:00 till 2022-07-07 12:49:22+00:00
SMT_20220707_112434.gpx	23	2022-07-07 12:32:01+00:00 till 2022-07-07 12:49:22+00:00
SMT_20220707_112434.gpx	24	2022-07-07 12:37:10+00:00 till 2022-07-07 12:49:22+00:00
SMT_20220617_231459.gpx	22	2022-06-17 23:17:36+00:00 till 2022-06-17 23:17:58+00:00
SMT_20220826_231852.gpx	23	2022-08-26 23:26:43+00:00 till 2022-08-26 23:28:19+00:00
SMT_20220826_231852.gpx	24	2022-08-26 23:28:41+00:00 till 2022-08-26 23:30:12+00:00
SMT_20220828_111632.gpx	22	2022-08-28 11:21:14+00:00 till 2022-08-28 11:23:09+00:00
SMT_20220828_111632.gpx	23	2022-08-28 11:24:07+00:00 till 2022-08-28 11:25:44+00:00
SMT_20220828_111632.gpx	24	2022-08-28 11:26:44+00:00 till 2022-08-28 11:28:09+00:00
SMT_20220623_231633.gpx	13	2022-06-23 23:29:11+00:00 till 2022-06-23 23:31:38+00:00
SMT_20220623_231633.gpx	22	2022-06-23 23:23:06+00:00 till 2022-06-23 23:26:51+00:00
SMT_20220807_111547.gpx	12	2022-08-07 11:22:02+00:00 till 2022-08-07 11:22:59+00:00
SMT_20220807_111547.gpx	13	2022-08-07 11:26:06+00:00 till 2022-08-07 11:27:55+00:00
SMT_20220624_111844.gpx	12	2022-06-24 11:33:01+00:00 till 2022-06-24 11:33:33+00:00
SMT_20220624_111844.gpx	13	2022-06-24 11:33:25+00:00 till 2022-06-24 11:35:11+00:00
SMT_20220624_111844.gpx	22	2022-06-24 11:31:13+00:00 till 2022-06-24 11:33:06+00:00
SMT_20220929_111540.gpx	12	2022-09-29 11:19:52+00:00 till 2022-09-29 11:20:48+00:00
SMT_20220720_111442.gpx	21	2022-07-20 11:28:20+00:00 till 2022-07-20 11:34:28+00:00
SMT_20220720_111442.gpx	22	2022-07-20 11:32:55+00:00 till 2022-07-20 11:49:29+00:00
SMT_20220720_111442.gpx	23	2022-07-20 11:37:02+00:00 till 2022-07-20 12:04:15+00:00
SMT_20220720_111442.gpx	24	2022-07-20 11:44:43+00:00 till 2022-07-20 12:12:56+00:00
SMT_20220829_111459.gpx	21	2022-08-29 11:15:53+00:00 till 2022-08-29 11:15:59+00:00
SMT_20220829_111459.gpx	23	2022-08-29 11:18:35+00:00 till 2022-08-29 11:19:05+00:00
SMT_20220829_111459.gpx	24	2022-08-29 11:19:44+00:00 till 2022-08-29 11:20:20+00:00
SMT_20220705_113009.gpx	21	2022-07-05 12:48:04+00:00 till 2022-07-05 12:53:24+00:00
SMT_20220705_113009.gpx	11	2022-07-05 12:50:13+00:00 till 2022-07-05 12:53:24+00:00
SMT_20220817_111600.gpx	21	2022-08-17 11:20:21+00:00 till 2022-08-17 11:35:09+00:00
SMT_20220817_111600.gpx	11	2022-08-17 11:27:50+00:00 till 2022-08-17 11:30:32+00:00
SMT_20220904_111459.gpx	21	2022-09-04 11:16:45+00:00 till 2022-09-04 11:18:39+00:00
SMT_20220904_111459.gpx	22	2022-09-04 11:20:46+00:00 till 2022-09-04 11:21:55+00:00
SMT_20220904_111459.gpx	23	2022-09-04 11:22:57+00:00 till 2022-09-04 11:24:53+00:00
SMT_20220904_111459.gpx	24	2022-09-04 11:24:58+00:00 till 2022-09-04 11:25:49+00:00
SMT_20220928_111604.gpx	12	2022-09-28 11:37:02+00:00 till 2022-09-28 11:38:16+00:00
SMT_20220928_111604.gpx	11	2022-09-28 11:33:16+00:00 till 2022-09-28 11:36:59+00:00
SMT_20220930_231507.gpx	13	2022-09-30 23:19:10+00:00 till 2022-09-30 23:19:35+00:00

**APPENDIX C. BALLOON PASSBYS UNDER 10°
IN THE SUMMER OF 2022**

Balloon filename (gpx)	station	expected timeframe
SMT_20220904_231730.gpx	24	2022-09-04 23:22:54+00:00 till 2022-09-04 23:23:14+00:00
SMT_20220921_111527.gpx	12	2022-09-21 11:27:31+00:00 till 2022-09-21 11:29:09+00:00
SMT_20220921_111527.gpx	11	2022-09-21 11:25:37+00:00 till 2022-09-21 11:27:09+00:00
SMT_20220921_111527.gpx	13	2022-09-21 11:29:18+00:00 till 2022-09-21 11:30:46+00:00
SMT_20220725_112511.gpx	12	2022-07-25 11:29:27+00:00 till 2022-07-25 11:30:29+00:00
SMT_20220907_231621.gpx	23	2022-09-07 23:22:59+00:00 till 2022-09-07 23:23:40+00:00
SMT_20220907_231621.gpx	24	2022-09-07 23:24:09+00:00 till 2022-09-07 23:25:07+00:00
SMT_20220827_111534.gpx	24	2022-08-27 11:22:30+00:00 till 2022-08-27 11:23:43+00:00
SMT_20220615_231713.gpx	12	2022-06-15 23:21:29+00:00 till 2022-06-15 23:22:47+00:00
SMT_20220908_111450.gpx	12	2022-09-08 11:20:02+00:00 till 2022-09-08 11:21:40+00:00
SMT_20220908_111450.gpx	13	2022-09-08 11:22:39+00:00 till 2022-09-08 11:24:21+00:00
SMT_20220616_231523.gpx	11	2022-06-16 23:17:55+00:00 till 2022-06-16 23:18:16+00:00
SMT_20220729_112533.gpx	21	2022-07-29 12:19:23+00:00 till 2022-07-29 12:33:04+00:00
SMT_20220729_112533.gpx	12	2022-07-29 12:26:18+00:00 till 2022-07-29 12:36:15+00:00
SMT_20220729_112533.gpx	11	2022-07-29 12:21:20+00:00 till 2022-07-29 12:37:29+00:00
SMT_20220704_112103.gpx	21	2022-07-04 11:46:05+00:00 till 2022-07-04 12:00:57+00:00
SMT_20220704_112103.gpx	12	2022-07-04 11:48:49+00:00 till 2022-07-04 12:35:14+00:00
SMT_20220704_112103.gpx	11	2022-07-04 11:41:27+00:00 till 2022-07-04 11:58:58+00:00
SMT_20220704_112103.gpx	13	2022-07-04 11:56:33+00:00 till 2022-07-04 12:40:36+00:00
SMT_20220704_112103.gpx	22	2022-07-04 11:49:29+00:00 till 2022-07-04 12:25:01+00:00
SMT_20220704_112103.gpx	23	2022-07-04 11:54:52+00:00 till 2022-07-04 12:33:48+00:00
SMT_20220704_112103.gpx	24	2022-07-04 11:59:40+00:00 till 2022-07-04 12:34:54+00:00
SMT_20220825_112057.gpx	12	2022-08-25 11:25:22+00:00 till 2022-08-25 11:25:43+00:00
SMT_20220712_111713.gpx	11	2022-07-12 12:29:00+00:00 till 2022-07-12 12:30:52+00:00
SMT_20220628_111612.gpx	11	2022-06-28 11:19:17+00:00 till 2022-06-28 11:19:27+00:00
SMT_20220702_231622.gpx	21	2022-07-03 00:14:37+00:00 till 2022-07-03 00:47:11+00:00
SMT_20220702_231622.gpx	12	2022-07-03 00:22:20+00:00 till 2022-07-03 00:52:30+00:00
SMT_20220702_231622.gpx	11	2022-07-03 00:29:05+00:00 till 2022-07-03 00:52:25+00:00
SMT_20220702_231622.gpx	13	2022-07-03 00:21:33+00:00 till 2022-07-03 00:52:30+00:00
SMT_20220702_231622.gpx	22	2022-07-03 00:11:26+00:00 till 2022-07-03 00:50:35+00:00
SMT_20220702_231622.gpx	23	2022-07-03 00:14:24+00:00 till 2022-07-03 00:51:28+00:00
SMT_20220702_231622.gpx	24	2022-07-03 00:16:28+00:00 till 2022-07-03 00:51:10+00:00
SMT_20220706_112237.gpx	21	2022-07-06 12:48:26+00:00 till 2022-07-06 12:48:49+00:00
SMT_20220803_232212.gpx	21	2022-08-03 23:23:53+00:00 till 2022-08-03 23:23:54+00:00
SMT_20220803_232212.gpx	22	2022-08-03 23:26:19+00:00 till 2022-08-03 23:27:55+00:00
SMT_20220803_232212.gpx	23	2022-08-03 23:29:46+00:00 till 2022-08-03 23:34:09+00:00
SMT_20220803_232212.gpx	24	2022-08-03 23:34:19+00:00 till 2022-08-03 23:38:20+00:00

BIBLIOGRAPHY

- [1] Measurement of the multi-TeV neutrino interaction cross-section with IceCube using earth absorption. *Nature*, 551(7682):596–600, nov 2017.
- [2] M. G. Aartsen, M. Ackermann, J. Adams, J. A. Aguilar, et al. Neutrino astronomy with the next generation icecube neutrino observatory, 2019.
- [3] M.G. Aartsen, M. Ackermann, J. Adams, J.A. Aguilar, et al. The IceCube neutrino observatory: instrumentation and online systems. *Journal of Instrumentation*, 12(03):P03012–P03012, mar 2017.
- [4] J.A. Aguilar, P. Allison, J.J. Beatty, et al. Design and sensitivity of the radio neutrino observatory in greenland (RNO-g). *Journal of Instrumentation*, 16(03):P03025, mar 2021.
- [5] P. Allison, R. Bard, J. J. Beatty, D.Z. Besson, C. Bora, C.-C. Chen, C.-H. Chen, P. Chen, A. Christenson, A. Connolly, J. Davies, M. Duvernois, B. Fox, R. Gaior, P. W. Gorham, K. Hanson, J. Haugen, B. Hill, K. D. Hoffman, E. Hong, S.-Y. Hsu, L. Hu, J.-J. Huang, M.-H. A. Huang, A. Ishihara, A. Karle, J. L. Kelley, D. Kennedy, I. Kravchenko, T. Kuwabara, H. Landsman, A. Laundrie, C.-J. Li, T. C. Liu, M.-Y. Lu, L. Macchiarulo, K. Mase, T. Meures, R. Meyhandan, C. Miki, R. Morse, J. Nam, R. J. Nichol, G. Nir, A. Novikov, A. O’Murchadha, C. Pfendner, K. Ratzlaff, M. Relich, M. Richman, L. Ritter, B. Rotter, P. Sandstrom, P. Schellin, A. Shultz, D. Seckel, Y.-S. Shiao, J. Stockham, M. Stockham, J. Touart, G. S. Varner, M.-Z. Wang, S.-H. Wang, Y. Yang, S. Yoshida, and R. Young and. Performance of two askaryan radio array stations and first results in the search for ultrahigh energy neutrinos. *Physical Review D*, 93(8), apr 2016.
- [6] G A Askaryan. Excess negative charge of an electron-photon shower and the coherent radio emission from it. *Zhur. Eksptl'. i Teoret. Fiz.*, 41, 8 1961.
- [7] S.W. Barwick, E.C. Berg, D.Z. Besson, G. Gaswint, C. Glaser, A. Hallgren, J.C. Hanson, S.R. Klein, S. Kleinfelder, L. Köpke, I. Kravchenko, R. Lahmann, U. Latif, J. Nam, A. Nelles, C. Persichilli, P. Sandstrom, J. Tatar, and E. Unger. Observation of classically ‘forbidden’ electromagnetic wave propagation and implications for neutrino detection. *Journal of Cosmology and Astroparticle Physics*, 2018(07):055–055, jul 2018.

- [8] Federica Bradascio. Search for high-energy neutrinos from agn cores, 2019.
- [9] S. Buitink, J. Bacelar, R. Braun, G. de Bruyn, H. Falcke, O. Scholten, K. Singh, B. Stappers, R. Strom, and R. al Yahyaoui. The numoon experiment: first results, 2008.
- [10] Jr. Cowan, C. L., F. Reines, F. B. Harrison, H. W. Kruse, and A. D. McGuire. Detection of the Free Neutrino: A Confirmation. *Science*, 124(3212):103–104, July 1956.
- [11] Scott Dodelson. *Modern Cosmology*. Academic Press, Amsterdam, 2003.
- [12] K. Eguchi, S. Enomoto, K. Furuno, J. Goldman, H. Hanada, H. Ikeda, K. Ikeda, K. Inoue, et al. First results from kamland: Evidence for reactor antineutrino disappearance. *Physical Review Letters*, 90(2), jan 2003.
- [13] Thomas K. Gaisser, Ralph Engel, and Elisa Resconi. *Cosmic Rays and Particle Physics*. Cambridge University Press, 2 edition, 2016.
- [14] C. Glaser, D. García-Fernández, A. Nelles, J. Alvarez-Muñiz, S. W. Barwick, D. Z. Besson, B. A. Clark, A. Connolly, C. Deaconu, K. D. de Vries, J. C. Hanson, B. Hokanson-Fasig, R. Lahmann, U. Latif, S. A. Kleinfelder, C. Persichilli, Y. Pan, C. Pfendner, I. Plaisier, D. Seckel, J. Torres, S. Toscano, N. van Eijndhoven, A. Vieregg, C. Welling, T. Winchen, and S. A. Wissel. NuRadioMC: simulating the radio emission of neutrinos from interaction to detector. *European Physical Journal C*, 80(2):77, January 2020.
- [15] C. Glaser, D. García-Fernández, A. Nelles, J. Alvarez-Muñiz, S. W. Barwick, D. Z. Besson, B. A. Clark, A. Connolly, C. Deaconu, K. D. de Vries, J. C. Hanson, B. Hokanson-Fasig, R. Lahmann, U. Latif, S. A. Kleinfelder, C. Persichilli, Y. Pan, C. Pfendner, I. Plaisier, D. Seckel, J. Torres, S. Toscano, N. van Eijndhoven, A. Vieregg, C. Welling, T. Winchen, and S. A. Wissel. NuRadioMC: simulating the radio emission of neutrinos from interaction to detector. *The European Physical Journal C*, 80(2), jan 2020.
- [16] Christian Glaser, Anna Nelles, Ilse Plaisier, Christoph Welling, Steven W. Barwick, Daniel García-Fernández, Geoffrey Gaswint, Robert Lahmann, and Christopher Persichilli. NuRadioReco: a reconstruction framework for radio neutrino detectors. *The European Physical Journal C*, 79(6), jun 2019.
- [17] M. Grabe. *Measurement Uncertainties in Science and Technology*. Springer Berlin Heidelberg, 2005.
- [18] R.A. Herman. *A Treatise on Geometrical Optics*. Creative Media Partners, LLC, 2019.
- [19] Michael M. Herron and Chester C. Langway. Firn densification: An empirical model. *Journal of Glaciology*, 25(93):373–385, 1980.
- [20] Nils Heyer and Christian Glaser. First-principle calculation of birefringence effects for in-ice radio detection of neutrinos. *The European Physical Journal C*, 83(2):124, Feb 2023.
- [21] R. Hiller, P. A. Bezyazeekov, N. M. Budnev, et al. Tunka-rex: energy reconstruction with a single antenna station. *EPJ Web of Conferences*, 135:01004, 2017.
- [22] Tim Huege and Dave Besson. Radio-wave detection of ultra-high-energy neutrinos and cosmic rays. *Progress of Theoretical and Experimental Physics*, 2017(12), nov 2017.
- [23] J.D. Jackson. *Classical Electrodynamics*. Wiley, 1998.

- [24] Demosthenes Kazanas. Neutrinos from AGN. In Felix A. Aharonian and Heinz J. Völk, editors, *High Energy Gamma-Ray Astronomy: International Symposium*, volume 558 of *American Institute of Physics Conference Series*, pages 370–380, April 2001.
- [25] I. Kravchenko, S. Hussain, D. Seckel, D. Besson, E. Fensterholz, J. Ralston, J. Taylor, K. Ratzlaff, and R. Young. Updated results from the RICE experiment and future prospects for ultra-high energy neutrino detection at the south pole. *Physical Review D*, 85(6), mar 2012.
- [26] Tobias Melson, Hans-Thomas Janka, Robert Bollig, Florian Hanke, Andreas Marek, and Bernhard Müller. Neutrino-driven explosion of a 20 solar-mass star in three dimensions enabled by strange-quark contributions to neutrino–nucleon scattering. *The Astrophysical Journal Letters*, 808(2):L42, jul 2015.
- [27] B. Oeyen, I. Plaisier, A. Nelles, C. Glaser, and T. Winchen. Effects of firn ice models on radio neutrino simulations using a RadioPropa ray tracer. In *37th International Cosmic Ray Conference. 12-23 July 2021. Berlin*, page 1027, March 2022.
- [28] H. Schoorlemmer, K. Belov, A. Romero-Wolf, D. García-Fernández, V. Bugaev, et al. Energy and flux measurements of ultra-high energy cosmic rays observed during the first anita flight. *Astroparticle Physics*, 77:32–43, 2016.
- [29] C. Welling, P. Frank, T. Enßlin, and A. Nelles. Reconstructing non-repeating radio pulses with information field theory. *Journal of Cosmology and Astroparticle Physics*, 2021(04):071, apr 2021.
- [30] C. Welling, C. Glaser, and A. Nelles. Reconstructing the cosmic-ray energy from the radio signal measured in one single station. *Journal of Cosmology and Astroparticle Physics*, 10:075–075, oct 2019.
- [31] Tobias Winchen. RadioPropa — a modular raytracer for in-matter radio propagation. *EPJ Web of Conferences*, 216:03002, 2019.
- [32] Kane Yee. Numerical solution of initial boundary value problems involving maxwell’s equations in isotropic media. *IEEE Transactions on Antennas and Propagation*, 14(3):302–307, 1966.